

# **Additive Manufacturing of porous ceramic structures**

## Doctoral Thesis (Dissertation)

to be awarded the degree  
Doctor of Engineering (Dr.- Ing.)

submitted by

**Andrea Zocca**

from Mirano (VE), Italy

approved by the Faculty of Natural and Materials Science,  
Clausthal University of Technology

Date of oral examination

/ /

Chairperson of the Board of Examiners:

Chief Reviewers: Prof. Dr. rer. nat. Jens Günster, TU Clausthal  
Prof. Dr.-Ing. Paolo Colombo, University of Padova

Reviewers: Prof. Dr.-Ing. Enrico Bernardo, University of Padova  
Prof. Dr. rer. nat. Albrecht Wolter, TU Clausthal

Name, Vorname

Datum:

## **EIDESSTATTLICHE ERKLÄRUNG**

Hiermit erkläre ich an Eides Statt, dass ich die bei der Fakultät für Natur- und Materialwissenschaften der Technischen Universität Clausthal eingereichte Dissertation selbständig und ohne unerlaubte Hilfe verfasst und die benutzten Hilfsmittel vollständig angegeben habe.

Unterschrift

Name, Vorname

Datum:

## **EIDESSTATTLICHE ERKLÄRUNG**

Hiermit erkläre ich an Eides Statt, dass die eingereichte Dissertation weder in Teilen noch in Ihrer Gesamtheit einer anderen Hochschule zur Begutachtung vorliegt oder vorgelegen hat und dass ich bisher noch keinen Promotionsversuch unternommen habe.

Unterschrift

To my family and to Miriam,

for the love and the support during these years, despite the distance

## **Acknowledgements**

I would sincerely like to thank Prof. Jens Günster and Prof. Paolo Colombo for their supervision. Their support and advice has been countless and immensely valuable in these years. I recognize that without them my PhD would have been much harder both professionally and personally and I am very grateful for having them as my supervisors.

Special thanks to Prof. Enrico Bernardo and to Dr. Cynthia Gomes who have always helped me with fruitful discussion and much more.

I would also like to thank all my colleagues and collaborators, particularly Ulf Linow during my period in Berlin at BAM and Hamada Elsayed and Giorgia Franchin during the time spent at the University of Padova. It has been a pleasure to work with Hamada and I thank him in particular for formulating the mixtures to produce hardystonite, for their XRD characterization and for the DTA and XRD characterization of the AP40 glass-ceramic. Giorgia collaborated with me during the development of the extrusion-based 3D printing and shared with me the initial difficulties and the satisfactions of the first results.

Particular thanks to Marco Lopez, University of Marburg, for performing the in-vitro cell tests and for discussing them.

Further thanks to Dagmar Nicolaides at BAM for her help with the ICP and XRD measurements and to Mauro Gobbin for his help with the DTA measurements and his often needed advice.

I would like to extend my thanks to all the wonderful working groups in Berlin and in Padova.

I especially thank all the students that worked with me and that helped me with the experiments, particularly Douglas Coelho and Omar Sanson.

Finally, my acknowledgement to BAM, to the University of Padova and to INSTM (Consorzio Interuniversitario Nazionale per la Scienza e Tecnologia dei Materiali) for the financial and logistic support.

## **Abstract**

This doctoral thesis describes the additive manufacturing of porous structures starting from preceramic mixtures. Preceramic polymers are a class of inorganic polymers which can be converted to a ceramic with high yield. The use of a preceramic polymer has been explored in this work with the double aim of providing the desired ceramic phases and of facilitating the shaping processes.

The work is divided in three parts. In a first project, the powder-based three-dimensional printing technology has been applied to a preceramic polymer powder. Complex porous structures with Kagome and octahedral geometries have been replicated. The preceramic polymer was successively converted to a unique SiOC phase upon heat treatment in inert atmosphere. This approach, in contrast to the use of a ceramic powder, allows an easier shaping and the achievement of relatively higher green densities, due to the dissolution and re-solidification of the polymer in the process. The shaping of fine porous structures is particularly suited to this material because problems related to gas release during the polymer-to-ceramic transformation are limited.

In a second project, the same powder-based technology was applied to mixtures of a preceramic polymer and ceramic fillers. In this case, the preceramic polymer acts as a binder for the fillers during the printing process. Upon heat treatment in air, the polymer is converted to silica, which then can be reacted with the fillers in the mixture in order to form silicate ceramic phases. This approach is very versatile and has been used to form apatite-wollastonite bioceramic composites, which have been shaped into porous scaffolds with designed porosity and cylindrical or cubic geometries.

Finally, a different technology, which is an extrusion-based printing, has been applied. In this technique, as opposite to powder-based technologies, the part is not supported during its buildup, therefore a careful tailoring of the ink rheology is necessary in order to create spanning features. In this context, mixtures of a preceramic polymer and fillers were formulated which had a suitable shear-thinning behaviour, with the help of suitable additives. A hardystonite ceramic, which is a bio-silicate phase, was formed upon heat treatment in air. Hardystonite scaffolds with orthogonal pores were successfully shaped by the deposition of fine (< 0.5 mm) filaments.

**Keywords:** additive manufacturing; porous ceramics; preceramic polymers.

## **Zusammenfassung**

Diese Dissertation beschreibt die Additive Fertigung von porösen Strukturen aus präkeramischen Mischungen. Präkeramische Polymere sind eine Gruppe von anorganischen Polymeren die, nach Pyrolyse, zu keramischen Materialien mit einer hohen Ausbeute verwandelt werden können. Die Verwendung von präkeramischen Polymeren wurde in dieser Arbeit mit zwei Zielsetzungen erforscht: die gewünschte keramische Phasen zu generieren und die Formgebung zu erleichtern.

Diese Arbeit ist in drei Abschnitte eingeteilt: In einem ersten Projekt, wurde das Pulver-Bett 3D-Druck Verfahren auf ein präkeramisches Pulver angewendet. Komplizierte poröse Strukturen wurden mit Kagome und Oktaedern Geometrie aufgebaut. Das präkeramische Polymer wurde später zu einer speziellen SiOC Phase umwandelt, durch eine Wärmebehandlung in inerter Atmosphäre.

Dieser Ansatz erlaubt, im Gegenteil der Benutzung eines keramischen Pulvers, eine einfachere Formgebung und die Erreichung einer höheren Gründichte, aufgrund der Auflösung und erneuten Verfestigung des präkeramischen Polymers. Diese Formgebung ist für dieses Material für feine Strukturen besonders geeignet, weil die Probleme für die Aufschließung des Polymers, welche mit der Entwicklung von gasförmigen Spezies einhergeht, vermindert wird.

In einem zweiten Projekt, wurde die gleiche Technologie zur Mischungen von präkeramischen Polymeren und keramischen Füllmaterialien eingesetzt. In diesem Fall war das präkeramische Polymer ein Binder für die Füllmaterialien in dem Druckverfahren. Nach einer Wärmebehandlung, wurde das Polymer zu Silicium Oxid verwandelt, das mit den Füllmaterialien reagieren kann um silikatische Keramik zu bilden. Dieser Ansatz ist sehr vielfältig und wurde benutzt um Apatit-Wollastonite biokeramische Komposite zu erstellen. Poröse Scaffolds wurden mit zylindrischen oder kubischen Geometrien aufgebaut. Schlussendlich, wurde ein extrusionsbasiertes Verfahren eingesetzt. Entgegengesetzt des Pulver-Betts Verfahrens, ist das Bauteil während des Aufbaus nicht gestützt. Daher, ist die Rheologie der keramischen Paste sehr wichtig um nicht gestützte Teile aufzubauen. Deshalb, wurden Mischungen von präkeramischem Polymer und Füllmaterialien entwickelt, die eine Strukturviskosität zeigen. Eine Hardystonite Phase wurde nach einer Wärmebehandlung in Luft erstellt, die eine bio-Silikat Phase ist. Hardystonite Scaffolds mit orthogonalen Poren wurden durch die Abscheidung von dünnen ( $<0.5$  mm) Filamenten aufgebaut.

Stichwörter: Additive Fertigung; porös keramisch; präkeramische Polymere.



## Sommario

In questa tesi di dottorato sono descritte tecnologie di manifattura additiva per la realizzazione di strutture porose a partire da miscele preceramiche. I polimeri preceramici sono una classe di polimeri inorganici che possono essere convertiti in un materiale ceramico con una resa elevata. L'utilizzo di polimeri preceramici è stato studiato con il duplice obiettivo di fornire le fasi ceramiche desiderate e di facilitare i processi di formatura.

La descrizione è suddivisa in tre parti. In un progetto iniziale, una tecnologia di stampa 3D a polveri è stata applicata ad una polvere di polimero preceramico. Strutture porose di geometria complessa, quali Kagome od ottaedrica, sono state replicate. Il polimero preceramico è stato successivamente convertito in una speciale fase ceramica SiOC tramite trattamento in atmosfera inerte. Questo approccio, in confronto all'utilizzo di una polvere ceramica, permette di semplificare il processo nonché di ottenere una densità del verde relativamente elevata, grazie alla dissoluzione e solidificazione del polimero. Inoltre, la scelta di strutture porose è particolarmente adatta a questo materiale, in quanto i problemi relativi allo sviluppo di gas, che questo materiale rilascia durante il trattamento, vengono limitati.

In un secondo progetto, la stessa tecnologia a polveri è stata applicata a miscele di un polimero preceramico e filler. In questo caso, il ruolo del polimero preceramico è quello di un legante per i filler durante il processo di stampa. Tramite trattamento termico, il polimero viene convertito in silice, che può successivamente reagire con i filler per formare fasi silicatiche. Questo approccio è molto versatile ed è stato utilizzato per formare compositi bioceramici apatite-wollastonite, i quali sono stati replicati in varie forme di scaffolds porosi, con geometria cubica o cilindrica.

Infine, una tecnologia di stampa ad estrusione di filamento è stata utilizzata. Contrariamente alle tecnologie a polveri, in questo caso la parte da costruire non è supportata da altro materiale, pertanto uno studio della reologia delle paste ceramiche è essenziale per creare strutture non supportate tra due appoggi. In questo contesto, diverse miscele di un polimero preceramico e filler sono state formulate in modo da ottenere un comportamento pseudoplastico, grazie all'aggiunta di additivi adatti allo scopo. Una fase di hardystonite, che è un bio-silicato, viene formata tramite trattamento termico in aria. Scaffold di hardystonite con pori ortogonali sono stati creati tramite la deposizione di filamenti sottili (diametro < 0.5 mm).

Parole chiave: manifattura additiva; ceramici porosi; polimeri preceramici.

## I. MOTIVATION

## II. GENERAL INTRODUCTION

### II.I Additive Manufacturing

#### II.I.I Indirect Additive Manufacturing

II.I.I.I Powder-based 3D-printing (P-3DP)

II.I.I.II Powder-based selective laser sintering (P-SLS)

II.I.I.III Stereolithography (SL)

II.I.I.IV Slurry-based 3DP (S-3DP) and slurry-based SLS (S-SLS)

II.I.I.V Laminated object manufacturing (LOM)

#### II.I.II Direct Additive Manufacturing

II.I.II.I Direct inkjet printing (DIP)

II.I.II.II Filament extrusion 3D-printing

#### II.I.III Negative AM technologies

### II.II Polymer-derived ceramics

## CHAPTER 1: SiOC porous structures produced by powder-based 3D-printing of a preceramic polymer

### 1.1 Porous materials

1.1.1 Fabrication of porous ceramics

1.1.2 Elastic properties of porous materials

1.1.3 Stretching-dominated vs bending-dominated structures

### 1.2 Three-dimensional printing of preceramic polymers

#### 1.2.1 Materials and methods

#### 1.2.2 Results and discussion

1.2.2.1 Influence of the printing parameters

1.2.2.2 Optimization of printing and ceramization conditions

1.2.2.3 Printing of ordered porous structures

### 1.2.3 Conclusions

## CHAPTER 2: bioceramic scaffolds produced by powder-based 3D-printing of preceramic polymers and fillers

### 2.1 Bioceramics: role and major classes

#### 2.1.1 Silicate bioceramics

### 2.2 Synthesis of bio-silicate ceramics and composites from preceramic polymers and fillers

#### 2.2.1 AP40 glass-ceramic

#### 2.2.2 AP40/wollastonite composites from preceramic polymer and fillers

##### 2.2.2.1 Pressed samples

##### 2.2.2.2 Powder-based 3D-printing

#### 2.2.3 AP40/hardystonite composites from preceramic polymer and fillers

##### 2.2.3.1 Pressed samples

### 2.3 Characterization and comparison of pressed and 3D-printer samples

#### 2.3.1 Dissolution tests

#### 2.3.2 Physical and mechanical properties

### 2.4 Conclusions

## CHAPTER 3: bioceramic scaffolds produced by extrusion-based 3D-printing of preceramic polymers and fillers

### 3.1 Materials and methods

#### 3.1.1 3D-printer

#### 3.1.2 Ink preparation

#### 3.1.3 Rheological characterization

3.1.4 Direct ink writing of hardystonite 3D scaffolds

3.1.5 Phase composition characterization

3.1.6 Mechanical testing and physical characterization

3.2 Results and discussion

3.2.1 Rheological characterization

3.2.1.1 Dynamic oscillation test

3.2.1.2 Steady rate sweep

3.2.1.3 Time dependent recovery

3.2.2 Production and characterization of porous scaffolds

3.2.3 Phase composition

3.2.4 Physical and mechanical properties of the scaffolds

3.3 Comparison of the mechanical properties of scaffolds produced by different technologies

3.4 Conclusions

CONCLUSIONS

## **Motivation**

The main theme of this work is the additive manufacturing of ceramic materials, with particular focus on the processing of ceramics produced from polymeric precursors. Two technologies have been exploited: the powder-based three-dimensional printing and the extrusion based three-dimensional printing.

Additive manufacturing will be introduced in the General Introduction chapter, paragraph II.I.

The two cited technologies are very well known and increasingly spreading, however their use for the shaping of polymer-derived ceramics is a novel application which takes advantage of the specific properties of these material systems. Advantages of processing preceramic polymers include a high achievable phase purity, generally low processing temperatures and most of all the shaping possibilities which are characteristic of polymeric materials.

Preceramic polymers and their advantages will be presented in the General Introduction chapter, paragraph II.II.

The powder-based three-dimensional printing of a pure preceramic polymer will be discussed in Chapter 1. Porous parts possessing an ordered porosity with a high level of complexity have been produced and converted to an SiOC amorphous ceramic.

Additive manufacturing of filled preceramic polymers using both a powder-based system (Chapter 2) and an extrusion-based system (Chapter 3) will also be presented. The use of filled preceramic polymers was employed as a versatile mean for producing parts made of silicate ceramics and in particular of bioceramic compositions.

The possibility of producing complex shaped geometries, together with the unique properties of preceramic polymers, seems to open new opportunities for the shaping of a wide range of ceramic parts where phase purity and complex geometries are of outmost importance, such as in the medical field.

# GENERAL INTRODUCTION

Partially in publication:

Zocca A, Colombo P, Gomes CM, Palmer T, Günster J. Additive manufacturing of ceramics: issues, potentialities and opportunities. Submitted to Journal of the American Ceramic Society 2015

## **II General introduction**

### **II.I Additive Manufacturing**

The term “3D-printing” has become nowadays part of the common language and known also to people outside the industry and research environment. However, often the same term “3D-printing” is used when referring to a range of different technologies. Therefore, it seems useful to introduce the nomenclature adopted by the ASTM committee and thus using the term “additive manufacturing” to include all these technologies. Specifically, ASTM F2792 - 12a (ASTM Standard F2792, 2012) (Standard Terminology for Additive Manufacturing Technologies) defines Additive Manufacturing (AM) as the “process of joining materials to make objects from 3D model data, usually layer upon layer, opposed to subtractive manufacturing methodologies, such as traditional machining.”

General advantages of AM are (Royal Academy of Engineering, 2013):

- Tooling costs are eliminated in AM, therefore the production of single parts or small batches is feasible and economical.
- Lower material waste and less energy consumption, thus a more “green” production.
- Increase of the production flexibility and reduction of lead time.
- Higher freedom in design and possible optimization of the parts performance.

All AM processes have in common the way that an object is built, i.e. by joining material. Most AM technologies also have in common that building of a part is carried out in a layer-by-layer fashion. Two main aspects however differ between technologies:

- 1) In which form the material is, and, often closely related to it, how the layers are formed.
- 2) How the material is selectively deposited or joined, within one layer and/or between successive layers. Briefly, this can be defined as the technology used to “inscribe” the cross-section of the object in a layer.

Based on the first point, material can be in form e.g. of a powder, a liquid, a slurry, a filament, or a sheet.

Following the second point, there are mainly two approaches: either the material is selectively deposited only where needed (e.g. by extrusion) or first a complete layer of material is formed and then the material in the layer is selectively joined (e.g. by laser melting) or removed (e.g. cutting of a sheet).

By crossing the options listed in points 1) and 2) it is possible to formulate a table where the most common AM technologies are located.

<b>Feedstock →</b>  ----- <b>Inscribing technology</b>  ↓	<b>Powder</b>	<b>Liquid</b>	<b>Slurry / paste</b>	<b>Filament</b>	<b>Sheet</b>
<b>Extrusion</b>			Robocasting	FDM	
<b>Jetting of Material</b>		DIP	DIP		
<b>Jetting of binder</b>	Powder based 3D-printing				
<b>Cutting</b>					
<b>Photo- polymerization</b>		SL	SL		
<b>Selective sintering / melting</b>	SLS/SLM				LOM

**Table 1** Classification of additive manufacturing technologies. FDM= fused deposition modelling; DIP= direct inkjet printing; LOM= laminated object manufacturing; SL= stereolithography; SLS/SLM= selective laser sintering/melting; LSD= layerwise slurry deposition.



Following similar criteria, ASTM divides AM processes in several categories:

- **Material extrusion:** material is selectively dispersed through a nozzle or orifice (e.g. robocasting, fused deposition modelling, FDM). (*Fab@home, MakerBot, RepRap, Wasp*).
- **Material jetting:** droplets of build material are selectively deposited (e.g. direct inkjet printing, DIP). (*Stratasys*).
- **Binder jetting:** a liquid bonding agent is selectively deposited to join powder materials (e.g. powder based 3D-printing). (*ExOne, Voxeljet, 3d-Systems (Z-Corp)*).
- **Sheet lamination:** sheets of material are bonded to form an object (e.g. laminated object manufacturing, LOM). (*Wuhan Binhu*).
- **Vat photopolymerization:** liquid photopolymer in a vat is selectively cured by light-activated polymerization (e.g. stereolithography, SL). (*3d-Systems, Lithoz, DWS, Envisiontec, CMET*).
- **Powder-bed fusion:** thermal energy selectively fuses regions of a powder bed (e.g. selective laser sintering/melting, SLS/SLM; selective electron beam melting). (*EOS, ReaLizer, SLM Solutions, Aspect*).
- **Direct energy deposition:** focused thermal energy fuses materials by melting as the material is deposited. (*InssTech*).

An example of manufacturing companies in the field is reported within brackets. The list to the best of my knowledge, and more information can be found at:

<http://wohlersassociates.com/manufacturers-and-developers.html>

*Table 2* summarizes some of the general characteristics of the most used AM technologies described in literature for manufacturing ceramic components. Indications about the quality and size of the produced parts (ability of making dense and/or monolithic parts, precision, surface quality) and cost of the production (cost of the feedstock preparation and cost of the process) are included.

Technology*	Feedstock (Liquid or Solid)	Dense Struts (Dense Ceramic, but Limited Volume)	Monolithic	Part Dimension <sup>§</sup> (Size that can be Produced Economically)	Surface (Quality of Parts, Not of Single Struts)	Precision	Cost of Feedstock Preparation	Cost of Process	Direct Vs. Indirect
P-3DP	Solid	No	No	M-XL	Medium	100 μm	Low	Medium	Indirect
P-SLS	Solid	No	No	M-L	Medium	100 μm	Low	High	Indirect
P-SLM	Solid	No	No	M-L	Medium	100 μm	Low	High	Indirect
S-3DP	Liquid	Yes	Yes	M-XL	High	100 μm	Low	Medium	Indirect
S-SLS	Liquid	Yes	Yes	M-L	High	100 μm	Low	High	Indirect
SL	Liquid	Yes	No	XS-M	High	< 1μm	Medium- High	Medium	Indirect
LOM	Solid	Yes	Yes	M-L	Medium	100 μm	Medium	Medium	Indirect
DIW/Robocasting	Liquid	Yes	No	S-XL	Low	10 μm	Low- Medium	Low	Direct
FDM	Liquid	Yes	No	S-M	Low	100 μm	Medium	Low	Direct
DIP	Liquid	Yes	Yes	S-M	Medium	10 μm	High	Medium	Direct
Direct Dep	Liquid				Low				Direct

\*: the definition of the acronyms for each technology are given later in the text

<sup>§</sup>: XS = 100 μm; S = 1 mm; M = 10 mm; L = 0.1 m; XL = 1 m

**Table 2.** Main characteristics of AM technologies used for printing ceramics.

Before commenting on the individual technologies, it is appropriate to qualify further the content of the columns in *Table 2*.

- Dense struts: this term indicates technologies that can provide a dense material (that is, without any residual porosity), at least for some of the possible geometries and features that they can produce (specifically, only features possessing a small length scale or volume) and some ceramic material systems. Importantly, it is relevant to notice that there is a correlation between the use of a liquid-based feedstock and the possibility of achieving a dense microstructure in the struts (or small printed features), as opposite to solid-based and, in particular, powder-based technologies.
- Monolithic: this term indicates technologies that are able to generate parts without residual micro-porosity, at least for some ceramic material systems, regardless of its volume and thickness. A part with these characteristics is what we define as a “ceramic monolithic part”. Naturally, the possibility to sinter to full density is related to the composition of the feedstock (i.e. presence of sintering aids, composition of the ceramic) and on the sintering schedule and

technique employed. Here, however, we consider as given that the ceramic powder could be sintered to full density (for instance if it was shaped into a tablet by cold pressing), and are interested in discussing whether it is the AM process itself that prevents this full sintering to happen in the final produced part.

- Part dimension: this is the maximum part size that can be produced. Based on the fact that the dimension of the process area (printing envelope) can be potentially scaled-up for most technologies, it is difficult to provide precise data and trends. However, at the current state-of-the-art, it is often the case that, for dimensions outside a certain range, it becomes more convenient, for economic and technical reasons, to switch from one technology to another. These dimensional ranges are indicated as sizes from XS to XL, corresponding to 100  $\mu\text{m}$  or to 1 m, respectively, as explained in the table caption.

We should also note that it is not only the dimension of the printing envelope for each AM technology that imposes a limit to the maximum part size (area or volume), but also the mechanical properties of the parts during the printing process. For instance, structures constituted by thin filaments and not supported by a liquid or powder bed can deform by their own weight during fabrication, when they're still not consolidated by sintering.

- Precision and surface quality are partially related, and are also correlated to the dimension and cost of the part (printing speed) to be produced. On the other hand, the surface of a part can become smoother due to the minimization of its free surface energy, if sufficient material transport can occur during fabrication or sintering, or artefacts such as steps deriving from deposited layers can be smoothed out by the presence of a liquid phase during sintering. Here, only the best state-of-the-art results achieved so far are listed. As the dimension of the part increases, the precision in many technologies can be reduced (e.g. by increasing the diameter of extrusion nozzles or the thickness of deposited powder layers) in order to obtain an economical building rate. It is furthermore noteworthy to observe that surface quality is important not only for aesthetical reasons, but also because it can influence the mechanical properties of the printed ceramic components. It is noteworthy to observe that filament based technologies can provide very smooth surfaces on a micro-scale level, but by fusing multiple filaments a textured surface is generated, which can significantly deviate from the surface contour of the 3D model.
- The cost parameter is divided into two factors: cost related to the feedstock and cost related to the process. Cost for feedstock does not include the cost for ceramic raw materials, as this would be similar for a conventional fabrication process. A low feedstock cost means that the material can be bought commercially and is usable with none or minimal further processing, irrespective of the cost of the specific ceramic raw material selected; this is typically the case for powders to

be used in powder-based and slurry-based technologies. Medium and high cost indicates that the material requires extensive secondary processing, and often has to be designed specifically for the application. An example is the ink designed for extrusion through very fine nozzles. Finally, the process cost considers depreciation of capital expenditure and operating expenses for the particular AM equipment, and costs related to necessary processing and post-processing of the final product. Machines which employ lasers, for example, are usually quite expensive and are not faster than equipment based on rather cheap inkjet printing heads. On the other hand, the extrusion of pastes through fine tips is typically based on a rather cheap setup, and the production rate can be adapted by changing the diameter of the tip, which makes this a low cost process.

We can also point out that AM technologies can be divided into two categories: direct and indirect. Direct 3D printing means that the material is directly deposited only in the position giving the desired shape of the final object. Indirect 3D printing means that, first a layer of material is deposited, subsequently the cross section (slice) of the part is inscribed in the layer and, after printing all layers to complete the process, excess material surrounding the part is removed to release the final object. Inscribing can be done in several ways, each one with its own characteristics.

Already from this distinction, some general considerations concerning the potentials and drawbacks of the two approaches can be outlined:

- 1) The excess material in indirect technologies forms a support to the successive layers, enabling the generation of parts with large overhangs. Direct techniques, on the other hand, require support structures for overhangs above a certain dimension, which may be often impractical or time consuming, and furthermore need to be removed in order to obtain the precise desired shape of the final object.
- 2) Indirect technologies require the removal of the excess material in the form of powder, liquid or solid pieces of a sheet, which can be difficult or impossible for certain geometries. For example, if the excess material is a powder, it may be complicated to remove it completely from small open pores and cells. In any case, it is not possible to print any form of closed porosity, because the material inside the pores that has not been inscribed cannot be removed. The direct deposition of material, instead, does not have such geometrical limitations.
- 3) Indirect technologies have the potential to be faster, because the material is deposited in one complete layer and the layer information, that is the cross section of the part to be built, can be printed on the entire area, selectively inscribing the desired profile. Moreover, the simultaneous

fabrication of multiple individual parts can be achieved. In direct technologies, instead, the material is usually deposited only in specific positions and in a sequence.

4) Direct technologies offer straightforward possibilities to use multi-material systems (ceramic/ceramic with functional grading, ceramic/plastic, ceramic/metal interfaces,). Indirect technologies can also do this, but with much more limitations, e.g. the addition of metallic materials acting as conductor in multilayer ceramic systems is possible, but their concentration is limited. (Kollenberg, 2014)

The following section reviews the current state-of-the-art of AM of ceramics, describing the main technologies developed so far. Specifically, the paragraph relative to each technology includes a description of: (i) the fabrication of structures with a designed macro-porosity and considerations about the residual micro-porosity in the parts, which might be resulting from the various fabrication technologies; (ii) the possibility of producing monolithic ceramics, according to the definition used in *Table 1*. The discussion relative to the AM fabrication of part with a designed porosity is particularly relevant for this work of thesis, since this will be the main topic of the experimental work described in chapters 1, 2 and 3.

## **II.I.I Indirect AM technologies**

### **II.I.I.I Powder-based 3D-printing (P-3DP)**

In powder-based AM technologies, a solid structure is realized by the successive deposition of layers of a flowable powder. A layer of powdered material is first spread and subsequently the corresponding layer information is selectively inscribed by e.g. local compaction or gluing; these steps are iteratively replicated until the object is completed. The layer information is defined by the corresponding cross-section of a sliced virtual 3D model of the object to be built. At the end, the part is completely embedded in a powder-bed, from which it can be easily extracted and cleaned. The technology used to inscribe the layer information depends on the specific process considered: two of the most well-known and world-wide spread processes are: “Three-dimensional printing” (3DP) and “Selective laser sintering” (SLS). (Bourell et al., 1992) The milestone patent “Three-dimensional printing techniques” (Sachs et al., 1993) by Sachs et al. was filed in 1989, while Deckard’s patent “Method and apparatus for producing parts by selective sintering” dates back to three years earlier. (Deckard, 1989) Within powder-based AM technologies, powders are bound or fused to more or less dense parts, often ready to use. The former method uses a printing head to selectively spread out droplets of a liquid binder, while the latter employs the energy of a focused laser beam to selectively sinter/melt a powder.

In the P-3DP process, an inkjet printing head spits a binding liquid onto a powder bed, thus defining the cross-section of the object in that layer. Some P-3DP setups stabilize the powder layer by misting with water droplets to avoid disturbance of the powder by the ballistic impact of the binder droplets. (Butscher et al., 2013) Multiple nozzles can also be used, allowing to cover a wide printing area. Printing machines with print heads consisting of a few hundred of parallel working jets and with a printing envelope as large as 6x6x6 m<sup>3</sup> are used to fabricate ceramic objects for architectural applications based on the cold consolidation of inorganic powders (such as marble) using a hydraulic or non-hydraulic binder. (Cesaretti et al., 2014) In Figure 1, we show, as an example, a large artwork piece which is 1.28 m wide, but could be printed up to a diameter of 3.5 m using such an equipment.

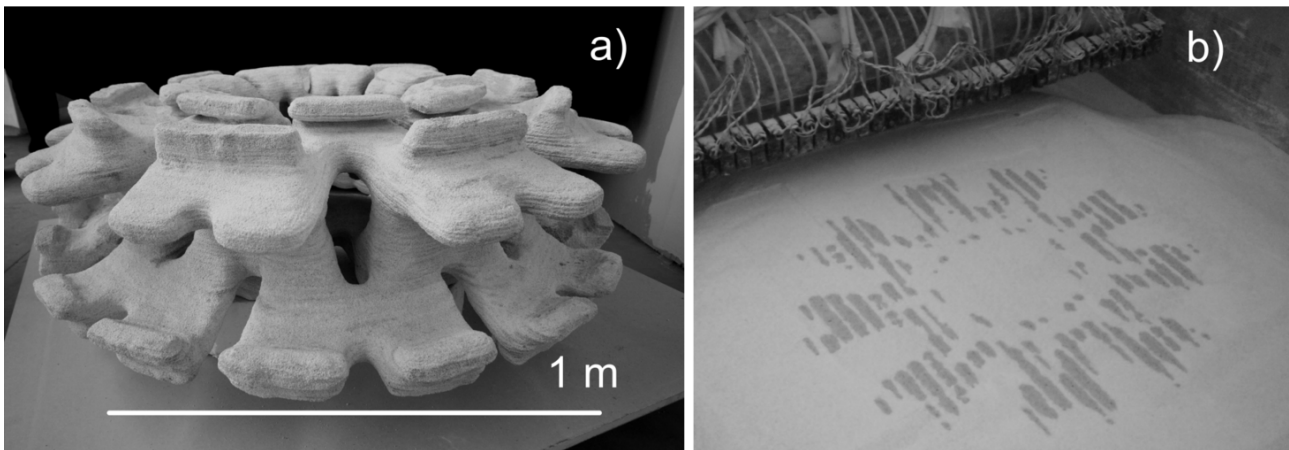


**Figure 1.** a) powder-based 3D-printed “The Flower” artwork model (the part is 1.28 m in diameter); b) image of a layer during the 3D-printing process (model designed by Yassi Mazandi; image courtesy of Antonino Italiano, Desamanera SRL, Italy).

The polymer-polymer derived approach has been applied to P-3DP, and in this context it offers several advantages. When using pure preceramic polymer powders, it is possible to achieve a high green density (~80% TD) because the sprayed solvent locally dissolves the preceramic polymer binding the particles together, filling also the inter-particle voids. (Zocca et al., 2013) Moreover, the preceramic polymer can be used as a non-sacrificial, reactive binder mixed with a glass powder to create bio-ceramic scaffolds based on wollastonite-apatite. (Zocca et al., submitted)

#### (i) Porous components

The vast majority of the research on powder-based 3D-printed porous parts has been devoted to the shaping of biomedical scaffolds for tissue engineering (TE). Two major classes of material-binder

systems have been used for this purpose: 1) the ceramic powder is bound by an organic glue, which is dissolved in a water- or solvent-based liquid and sprayed on the printing bed (Fielding et al., 2012a); alternatively, a polymer can be mixed with the ceramic powder and then used to glue the powder when in contact with the jetted liquid. (Castilho et al., 2014a),(Chumnanklang et al., 2007) The green part has to be successively sintered at high temperatures in order to obtain the final ceramic object. 2) a reactive liquid-powder system is employed, which involves a setting reaction at low temperature. There are several examples of systems based on calcium phosphates using phosphoric acids as a binder. (Bergmann et al., 2010; Castilho et al., 2014b; Klammert et al., 2009) An excellent review of the important scaffold parameters for this specific application, as well as of the most important processing aspects is already present in the literature. (Butscher et al., 2011) Typically, TE scaffolds have pores in the range 50-1000  $\mu\text{m}$  and a porosity  $> 60\%$ , because these characteristics are considered a requisite for successful bone ingrowth and full vascularization of the implants. Residual micro-porosity ( $< \sim 10 \mu\text{m}$ ) in the printed part (i.e. not the designed macro-porosity) was also recognized to be important for increasing the surface area, which leads to higher protein absorption and ion exchange. It should be noted that small pores ( $< \sim 500 \mu\text{m}$ ) cannot be printed because of resolution limits and, more importantly, because of the difficulty in removing the excess powder.

Calcium phosphate scaffolds made by P-3DP tend to have exactly this bimodal porosity: a designed porosity produced by P-3DP, in the range of  $\sim 0.5\text{--}2 \text{ mm}$ , and micro-porosity in the struts due to incomplete densification after binder/powder reaction and/or after sintering. In particular, sintering of the 3D-printed material to high density is hindered by the large particle size (indicatively 30-100  $\mu\text{m}$ ) of the powder used for printing, which is necessary in order to have a suitable level of flowability during the deposition of the layers. Even though the flowability can be improved by granulation of a fine ( $< 10 \mu\text{m}$ ) powder, many authors recognized that during the heat treatment a good level of densification can be achieved within the single granules, but only sintering necks are formed between the granules. (Chumnanklang et al., 2007; Barbara Leukers et al., 2005)

Parts made by P-3DP generally have a high level of residual porosity and this limits their mechanical properties. Chumnanklang et al. made HA samples by P-3DP which had 20–40 vol% micro-porosity and a 3-points-bending strength  $< 1.5 \text{ MPa}$ . (Chumnanklang et al., 2007) Klammert et al. developed a P-3DP process for Brushite ( $\text{CaHPO}_4 \cdot 2\text{H}_2\text{O}$ ) which had a micro-porosity of 38.8 vol% and a compressive strength of 23.4 MPa, and similarly for Monetite ( $\text{CaHPO}_4$ ), obtaining 43.8 vol% of micro-porosity and 15.3 MPa compressive strength. (Klammert et al., 2009) Castilho et al. measured the compressive strength of calcium phosphate cylinders, which reached a maximum of 23.8 MPa for a micro-porosity of 43.1 vol%. (Castilho et al., 2014a)

Besides applications for tissue engineering, P-3DP of silicate ceramics for different applications, including art and architecture, and foundry sands are rapidly growing markets. (“<http://www.voxeljet.de/en/services/castings/>; accessed on 28/02/2015,” 2015; Huson and Hoskins, 2014)

(ii) Monolithic components

P-3DP is very well suited to generate porous ceramic structures. Still, a major issue, hampering a completely autonomous production of parts and even restricting the freedom of design by means of these technologies, is the low density and stability of the parts during the building process, which is a direct result of the low powder packing in the powder-bed (as low as 25% TD (theoretical density)). The powder bed surrounding the part has an essential role, since it should support the structure during building, until it's ready for removal. Furthermore, powders with appreciable flowability for the deposition of thin layers are in a particle size range  $>20\ \mu\text{m}$  which generally does not provide sufficient sintering activity to form dense ceramics. One straightforward approach to increase the density of the powder bed and to use more fine powders is the deposition of ceramic slurries instead of dry powders. This strategy will be introduced in a following section. Another approach is the gas flow assisted powder deposition. (Zocca et al., 2014) While the first approach results in powder beds with powder packing densities  $>55\%$  TD, and thus sufficient for a full densification in subsequent sintering steps, the latter has just shown its potential for the deposition of fine powders ( $<20\ \mu\text{m}$  particle size) with appreciable packing densities which, however, still not exceed 45% TD when using commercial alumina powders ( $d_{50} = 17\ \mu\text{m}$ ). The low powder packing density has two major causes: the particle shape, which is generally far from spherical, and the tendency to form agglomerates. Also, particle charging due to the low electrical conductivity of ceramic materials might contribute to low packing densities.

Even though, as discussed above, the microstructure of parts obtained by P-3DP usually contains a high amount of residual porosity, some authors achieved higher densities after the heat treatment process. Three different approaches have been mainly investigated with this aim.

The first approach consists in modifying the composition of the ceramic material in order to enhance the sintering, by addition of dopants or of a viscous liquid-forming phase. Fielding et al., for example, obtained 95% density when adding ZnO and SiO<sub>2</sub> to TCP, (Fielding et al., 2012b) while Suwanprateeb et al. took advantage of liquid phase sintering producing a 97.5% dense HA + HA/wollastonite glass-ceramic composite. (Suwanprateeb et al., 2009)

The second approach is the infiltration of a porous preform produced by P-3DP. Melcher et al. used P-3DP to print alumina preforms which had a porosity of 36% after sintering, and infiltrated them



with Cu/Cu<sub>2</sub>O. (Melcher et al., 2006) The resulting Al<sub>2</sub>O<sub>3</sub>/Cu/CuO material had a flexural strength of 236 MPa and fracture toughness of 5.5 MPa m<sup>1/2</sup> thanks to the crack bridging mechanism of the metallic phase. A similar process was followed to infiltrate alumina preforms with glass. (Zhang et al., 2009) Another interesting material system achievable with this approach is the formation of RBSiC ceramics (reaction-bonded silicon carbide). In a first example, Fu et al. printed by P-3DP a mixture of Si, SiC and dextrin. (Fu et al., 2013) Successive infiltration with a liquid silicone resin and pyrolysis at 1000°C in nitrogen yielded carbon from the dextrin and an amorphous SiOC residue from the silicone resin. Infiltration of liquid silicon at 1500°C in vacuum finally led to the RBSiC material. Moon et al., instead, printed by P-3DP a carbon preform which had 48% open porosity, by using a binder based on furfuryl resin. (Moon et al., 2001) Following infiltration of Si at 1450°C in nitrogen led to the desired RBSiC composite. It is interesting to notice that in this latter example part of the carbon was derived from the polymeric binder, and this allowed the generation of functionally graded parts by varying the dosage of carbon-yielding binder and thus controlling the amount of SiC formed.

The first two approaches may be however difficult to apply to pure technical ceramics, such as alumina or silicon nitride. A third approach has been developed which consists of cold isostatic pressing (CIP) or warm isostatic pressing (WIP) the green body printed by P-3DP, before sintering. Yoo et al. obtained almost dense parts (99.2% relative density) by applying WIP to alumina parts (with MgO dopant) which had a flexural strength of 324 MPa after sintering. (Yoo et al., 1993) This method has been applied also to other ceramic systems, such as Ti<sub>3</sub>SiC<sub>2</sub>, yielding almost dense microstructures, but it poses geometrical limitations when applied to complex geometries, such as parts with internal cavities. (Sun et al., 2002, p. 2)

Concluding, P-3DP is very attractive because it has almost no limitation regarding the parts geometry (except for closed porosity) and dimension; however, it is potentially able to produce ceramic monolithic parts only for specific material systems, typically involving post-printing infiltration with metals or semimetals.

### **II.I.I.II Powder-based selective laser sintering (P-SLS)**

The P-SLS process works similarly to the P-3DP one, with the difference that the cross sections of the part to be built are inscribed by means of a laser beam. The local densification of the powders can be obtained by directly sintering the ceramic powder, or by mixing the powder with a binder phase (inorganic or, more often, polymeric) which is then melted by the laser light. Direct laser sintering of ceramics is complicated by the poor resistance of this class of materials to thermal shock. Furthermore, the short interaction time between laser and powder limits material diffusion,

leading to poor sintering. (Deckers et al., 2014; Juste et al., 2014; Kruth et al., 2007; P. Regenfuss et al., 2007) Binders within the powder which can be thermally activated, on the other hand, have been successfully used to shape porous ceramic parts, for applications and with results similar to those produced by P-3DP. (JP. Kruth et al., 2005; Kamatchi Subramanian et al., 1995) In the context of also this AM technology, preceramic polymers can offer some interesting opportunities, as highlighted by the work of Friedel et al., which used a laser light to selectively melt and crosslink a solid silicone resin mixed with SiC powders, to generate complex structures later sintered and infiltrated with a Si melt. (Friedel et al., 2005)

#### (i) Porous components

Kolan et al. produced bioglass scaffolds with 50% porosity and pores in the range 300–800  $\mu\text{m}$  by using an acrylic binder, followed by sintering at 675–695°C. (Kolan et al., 2011) Liu et al. deposited layers of a slurry made of hydroxyapatite powder and silica sol, exploiting the gelling of silica as binding mechanism, followed by sintering at 1200°C. (Liu et al., 2012) The produced scaffolds had pores in the range 750–1050  $\mu\text{m}$  and a porosity of 25–32%.

Another approach in the production of scaffolds for tissue engineering applications is the use of a bio-compatible polymer as binder. Simpson et al. reported the shaping of 95/5 Poly(L-lactide-co-glycolide) and HA/TCP composites, (Simpson et al., 2008) while Tan et al. employed a PEEK/HA composite. (Tan et al., 2003) It is worth noting that, in this case, the parts produced are a biopolymer-ceramic composite and they do not necessitate a sintering post-treatment, hence they are potentially ready to use as they come out of the SLS machine.

#### (ii) Monolithic components

Similarly to P-3DP, there are some rare examples in which dense monolithic ceramics have been obtained by P-SLS by infiltration with metals or semimetals after printing a porous ceramic preform. One of the early results concerns the generation of Si/SiC parts. Within the SLS process, SiC particles are glued together as a result of the formation of SiO<sub>2</sub> in oxidizing atmospheres, that is, ambient air. The highly porous parts have been used as preforms for the silicon infiltration. (Löschau et al., 1999) More recent work concentrates on selective laser melting (SLM), where the formation of a liquid phase ensures rapid densification. (Wilkes et al., 2013) The use of dense alumina and zirconia spherical particles (30  $\mu\text{m}$ ) as feedstock results in a high packing density of the particles in the powder bed. Preheating of the powder bed to a temperature of at least 1600°C reduces the thermal shock within the part to be built. Alumina-Zirconia eutectic mixtures reduce the

melting temperature of the powder bed to about 1860°C. With this approach, dense ceramic parts with remarkable mechanical properties could be generated via SLM. Nonetheless, crack formation within the ceramic bodies could not be avoided completely and an uncontrolled infiltration of the preheated powder bed by the liquid phase formed within the laser spot results in an ill-defined outer contour of the parts generated. Even though there is currently no strategy in sight which would allow the formation of dense monolithic ceramic parts via SLM, with precise contour and properties similar to conventional manufactured ceramic parts, the laser based technologies SLS and SLM are the only processes which could potentially deliver ready to use ceramic parts from ceramic materials that require sintering.

### **II.I.I.III Stereolithography (SL)**

The stereolithography technique is based on the photopolymerization of a liquid resin filled with ceramic particles, in a layer-by-layer fashion similarly to the other indirect AM technologies.

Typical compositions for the slurry include a monomer solution, a photo-initiator and additives for the dispersion of the ceramic powder, with a concentration of 40–60 vol%. (Chartier et al., 2008; Griffith and Halloran, 1996; Homa and Schwentenwein, 2015; Weizhao Zhou et al., 2010)

Contrary to powder-based AM, in stereolithography the material surrounding the part is liquid and therefore it is unable to provide any support; for this reason, depending on the specific geometry of the part, support structures are built together with the part, requiring subsequent removal. (Weizhao Zhou et al., 2010) Due to the high green densities and the use of fine ceramic particles, stereolithography permits the production of almost dense ceramic parts after a sintering post-treatment. (Griffith and Halloran, 1996) There are different technical solution for the SL process on the market. Lithoz (Lithoz GmbH, Vienna, Austria) follows an approach with the part built not fully immersed in the liquid feedstock, but mounted upside down on the building platform and dipped in a thin slurry layer deposited on a glass plate. The striking advantage of this strategy is the small amount of slurry required for building the part. (Homa and Schwentenwein, 2015).

#### **(i) Porous components**

The utilization of this technique was investigated by several authors for the generation of porous ceramics for various applications, taking advantage of the high precision that this technology provides and the possibility of obtaining dense struts. Kirihara et al. produced various types of samples possessing an ordered porosity, all with a total porosity value of 75 vol%. (Kirihara, 2014) YSZ lattices had about 100 µm long and thick struts with a lattice constant of 250 µm, and they

were designed for anode electrodes in solid oxide fuel cells.  $\text{Al}_2\text{O}_3$  parts were created based on the diamond structure, and their properties for an application as photonic crystals were simulated and measured. Finally, hydroxylapatite could be shaped into a dendrite structure with graded porosity, for tissue engineering applications. In all cases, the struts density ranged between 95 and 98%. Chu et al. also produced hydroxylapatite porous implants with a designed porosity of 40% and orthogonal pores. (Chu et al., 2002) The authors measured their mechanical properties and in-vivo behavior, reporting a high compressive strength of 30 MPa. Chartier et al. made  $\text{Al}_2\text{O}_3$  parts with a highly concentrated ceramic suspension (60 vol%) and recoating layers as thin as 25  $\mu\text{m}$ . (Chartier et al., 2002) 1 mm- and 2 mm-2D porous meshes were produced to demonstrate the process resolution.

Weiguo et al. produced bioinspired osteochondral scaffolds by first generating a porous  $\beta$ -TCP scaffold by SL followed by debinding and sintering and successively simulating a cartilage phase by freeze casting and cross-linking of a type I collagen suspension. (Weiguo Bian et al., 2012) In parallel to the traditional stereolithography process, a novel nano-stereolithography technique employs a two-photon equipment to achieve the cross-linking of a resin with a resolution down to 200 nm. Pham et al. modified a polyvinylsilazane preceramic polymer and used it to shape complex micron-sized structures. (Pham et al., 2006) The polymer was subsequently pyrolyzed at 600°C in nitrogen to obtain a SiCN ceramic. Silica nanoparticles were added to obtain a reduced and isotropic shrinkage. In particular, the generation of a  $9 \times 9 \times 9 \mu\text{m}^3$  scaffold with approximately 1  $\mu\text{m}$  cells was reported.

#### (ii) Monolithic components

Generally, it is possible to produce dense monolithic ceramic parts via SL, because powder compacts with powder packing densities higher than 55% can be generated. The only restriction is imposed by the debinding step, which is required to remove the binding additives from the green compacts before sintering. The thermally activated debinding steadily transforms the binder into gaseous species, and is one of the most critical steps in the SL process due to the possible formation of defects in the brown compact. Since thermal debinding takes place in the volume of the part and dissociation and combustion products must leave the bulk by diffusion, the heating process has to be carried out very slowly keeping the pressure inside the part below a critical threshold avoiding the formation of cracks and voids. On the other hand, there already exists a vast expertise on the thermally and solvent based debinding of ceramic green compacts, from injection molding of ceramics. Injection molding also uses pastes with high organic content, as binders, plasticizers, dispersants and lubricants, to produce parts with high complexity. (Chartier et al., 2001) Thus,

regarding the production of dense monolithic parts, a clear restriction of the SL process is, similarly to injection moulding, the maximum volume or wall thickness of the ceramic green body at which debinding can be achieved in a reasonable time. (Wroblewska, 2001) At wall thicknesses of about 1 cm, debinding already requires a thermal treatment over a time period of several days.

#### **II.I.I.IV Slurry-based 3DP (S-3DP) and slurry-based SLS (S-SLS)**

S-3DP and S-SLS are technologies which are a logic extension of powder based technologies. Instead of spreading a dry powder into thin layers, a ceramic slurry or slip is used in order to increase the powder packing density in the powder bed. Already in the milestone patent “Three-dimensional printing techniques” by Sachs et al., filed in 1989, the dispersion of powders "in a liquid vehicle" is suggested "to provide the desired uniform depositions of such powders at the required rates and densities". (Sachs et al., 1993) In a later patent by Sachs et al., filed in 1998, the use of liquid dispersions of powdered materials for the built up of a powder bed in a layer by layer fashion is explicitly described. (Sachs et al., 2003)

A major concern at that time was, however, the deposition of uniform layers with a flat and smooth surface. Since then, technologies capable of repeatedly depositing thin layers of ceramic slurries to build up dense powder beds for S-3DP and S-SLS have been developed. (Mühler et al., 2015; Tang and Yen, 2015; Yen, 2014) A survey of recently published work reveals a great potential of this technology for the manufacture of dense powder compacts, comparable to those produced by classical powder processing, that is with low organic content.

In S-3DP and S-SLS a liquid suspension of ceramic particles is spread as a thin layer comparable to tape casting, while within this layer a cast is formed comparable to slip casting. In the slip casting process, the slip is brought into contact with a porous body, the casting mold. When a liquid is wetting a porous body, capillary forces draw the liquid phase of the suspension into the porous mold. The particles start to form a powder compact, the cast, at the molds surface. The cast formation kinetics obeys a square-root-of-time law by depositing individual particles from the suspension to the surface of the mold. In case of the Layerwise Slurry Deposition (LSD) process the mold is formed by the previously deposited and dried layers. (Tian et al., 2011) Slip casting results in the formation of powder compacts with densities potentially exceeding 60% TD. Furthermore, due to the free settling of the powder particles from the suspension, no obvious interface is formed between individual layers. The formation of a cast starts as soon as the slurry is in contact with previously deposited and dry layers. Hence, the speed of the doctor blade relative to the dry layers must be high enough to prevent collision of the cast with the doctor blade. On the other hand, when the speed of the doctor blade is too high, layer deposition is not uniform, because shear stresses

within the suspension will result in an inhomogeneous deposition. For commercial silicate ceramic slurries, a speed of the doctor blade of 50 mm/s is typically chosen. For technical ceramics, the cast grows significantly faster and the speed of the doctor blade must be increased to 100 mm/s or higher. In the P-3DP and P-SLS powder-based processes, the part built is easily released from the powder bed, but this is not the case for the slurry based process. After deposition of all layers required for building up the desired geometry, the laser sintered or printed body is embedded in the powder bed which now is a block of densely packed particles. For the release of the part, the powder compact must be dissolved by a solvent. In case water based slurries are used for the layer deposition, water can act as a solvent for the powder bed.

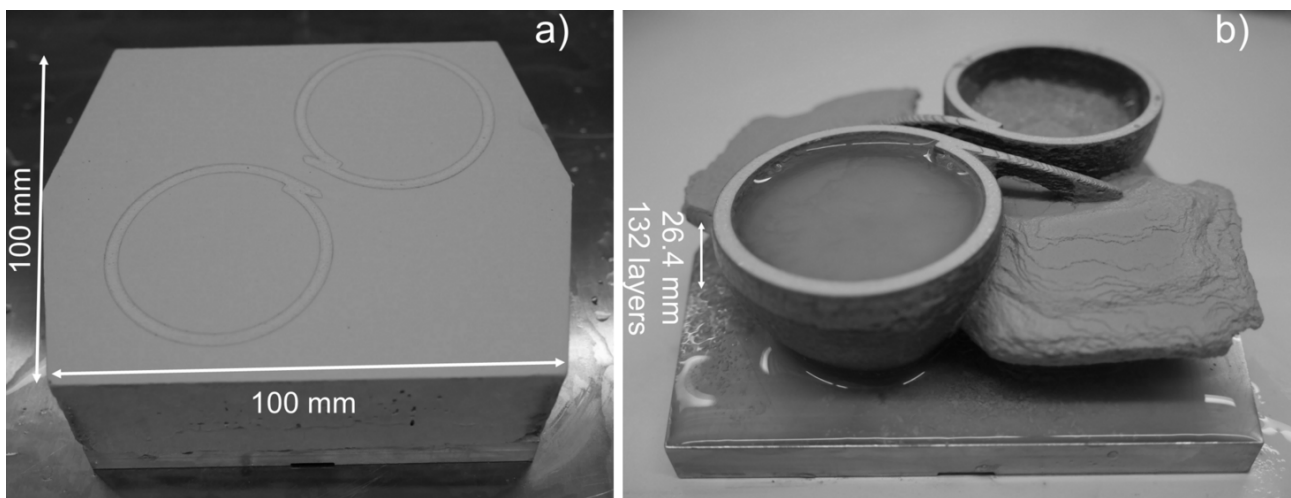


**Figure 2.** Release of two espresso cups made of porcelain by employing the Layerwise Slurry Deposition (LSD) technology. a) powder bed, formed by 132 layers with a thickness of 200  $\mu\text{m}$ , containing the two laser-sintered cups; b) cups partially released from the powder bed.

Figure 2 shows an example for the release of two espresso cups fabricated by the S-SLS process. The use of a ceramic suspension for layer deposition in additive manufacturing is an upcoming technology, and only few results are available. The advantage of slurry based layer deposition is its potential to produce powder compacts with high powder packing densities, typically exceeding 55% TD. For the manufacture of a powder compact with properties comparable to those produced by classical powder processing, S-3DP has the highest potential. By the use of small amounts of organic or inorganic binders provided by a printing head, the particles in the densely packed powder bed are locally glued together, and compacts generated by this technology don't require any additional treatment prior to sintering. Thus, we can forecast that S-3DP will be more and more used for the printing of ceramic powder compact. The laser treatment in S-SLS, however, will affect

the microstructure of the powder compact typically in a direction which is not favorable for the manufacture of advanced ceramic.

#### **II.I.I.V Laminated object manufacturing (LOM)**

Originally known as Layered Laminated Manufacturing (LLM), later on commercialized under the trade name Laminated Object Manufacturing (LOM) by Helysis or CerLAM and MetLAM by Javelin 3D, this AM process deals with the 3D building of parts by the lamination of paper, tapes or similar shapes at low-medium temperature and pressure. LOM has been considered as an alternative for the lamination of green ceramic tapes into 3D dense or semi-dense parts. (Cui et al., 2003; Gomes et al., 2008; John Kechagias, 2007; Klosterman et al., 1998, 1997; Rodrigues et al., 2000; Weisensel et al., 2004; Windsheimer et al., 2007)

The main advantage of this technique is the possibility of producing laminates directly from green tapes, which in turn are produced by extrusion, (Zhang et al., 1999) tape casting, (Cui et al., 2003; Gomes et al., 2008) or preceramic paper. (Weisensel et al., 2004; Windsheimer et al., 2007) In addition, LOM processing: 1) does not introduce an extra organic component that must be eliminated during the thermal treatment process, such as for stereolithography; 2) compared to low temperature lamination process, the applied pressure and temperature are lower, which prevents delamination caused by an inhomogeneous pressure distribution in complex shapes; 3) does not require higher capillary forces to promote the union between adjacent tapes during thermal treatment; 4) allows the lamination of water-based green tapes, which is not successfully achieved by thermo-compression, for example.

Compared to some conventional manufacturing processes such as injection molding, (Giassi et al., 2005) extrusion, (Bertan et al., 2009) or roll pressing, (Reitz et al., 2006) LOM parts exhibit moderate values of flexural strength at relatively high porosities. (Gomes et al., 2011, 2008) Values of mechanical strength for silicon nitride parts obtained by LOM of  $\sim 475 \pm 34$  MPa have been reported, (Liu et al., 2015) which is comparable to silicon nitride ceramics prepared by pressureless sintering (Ling and Yang, 2005; Penas et al., 2001; Ye et al., 2005) and higher than for the components fabricated by gel casting ( $54.5 \pm 2.3$  MPa). (Wang et al., 2013; Yu et al., 2009)

The main drawbacks of this technology, as in most lamination process, are related with the quality of the interfaces between tapes and presence of defects. Common issues being reported are delamination, interfacial porosities and differential shrinkage. (Gomes et al., 2011, 2008)

## **II.I.II Direct AM technologies**

### **II.I.II.I Direct inkjet printing (DIP)**

Direct inkjet printing is a technology which uses a ceramic suspension to build up structures by the successive deposition of individual drops provided by a printing head. The ceramic suspension, or ink, consists of ceramic particles (typically >20 vol%) dispersed in a liquid carrier containing different additives to stabilize the suspension, adjusts its viscosity and surface tension, and to control the spreading and drying of the deposited droplets. (Özkol et al., 2010; Teng and Edirisinghe, 1998) As liquid carrier, water or organic liquids can be used, depending on the specific requirements of the printing head. In order to ensure that ceramic particles can be fed as a suspension through the individual deposition nozzles of the printing head, their size ( $d_{50}$ ) is typically kept in the sub-micrometer range at a narrow particle size distribution. (Wätjen et al., 2014) Different to powder based 3D printing (P-3DP) DIP builds up structures directly from the material provided by the ink. DIP technology is capable to generate complex structures with a high powder packing density, as it uses ceramic suspensions. Together with a good sintering activity of the generated green parts, ensured by the use of submicron powders, DIP can provide parts from oxide and non-oxide ceramics with appreciable mechanical properties. (Cappi et al., 2008; Özkol et al., 2012; Tomov et al., 2010) Furthermore, due to the small volume (picoliter) of the individual droplets provided by the printing head, the generation of structures with well controllable material gradients is possible in multi material DIP setups. (Özkol et al., 2010) The printing of complex shaped structures with overhangs and undercuts can be realized by printing support structures with an ink providing a sacrificial material (e.g. carbon black), which is conveniently removed during firing in oxidizing conditions. Currently, DIP of ceramic materials is industrially developed for the fabrication of 2D components (e.g. printed electronics) ("<http://www.ceradrop.fr/en/>; accessed on 28/02/2015," 2015) but not yet well exploited for making 3D parts.

An alternative approach is the direct printing of a preceramic polymer solution, which takes advantage of the solubility of many preceramic polymers in several solvents. Mott et al. used polycarbosilane to produce silicon carbide parts using DIP, with or without the use of SiC particles in the ink. (Mott and Evans, 2001)

### **II.I.II.II Filament extrusion 3D-printing: Robocasting, Direct ink writing (DIW), Fused deposition modeling (FDM)**

The direct deposition of ceramic slurries is arguably the most used AM technology for the generation of porous structures. It consists in the extrusion through a nozzle of a viscous ceramic paste in the form of a filament. The control of the rheological properties of the filament is essential



to prevent deformation of the part after extrusion and sagging of the filaments, especially when the geometry includes spanning features as in most porous components. The technique was originally patented and developed by Cesarano at the Sandia National Laboratories in the USA under the name of “Robocasting”. (Cesarano and Calvert, 2000) In Robocasting, a ceramic suspension with a high solid loading undergoes a transformation from a pseudoplastic to a dilatant behavior when extruded in air, triggered by minimal drying of the slurry. Drying in air, however, limits the minimum diameter of the printing nozzle to about 500  $\mu\text{m}$ , otherwise clogging is experienced. In order to overcome these issues, inks have been developed which have a reversible gel transformation and are deposited in a non-wetting (often oil) bath. Briefly, they behave like a viscous gel when loaded in the printing head, but as they are extruded the shear stress breaks the gel structure and the viscosity decreases of several orders of magnitude. After extrusion, the fluid undergoes a quick gelation increasing again the viscosity to a level before shearing which prevents deformation of the filament. This behavior can be achieved by controlled flocculation of a ceramic suspension (e.g. by a change in pH, ionic strength of the solvent, addition of polyelectrolytes) to form a gel, (Lewis et al., 2006) or by using gelling additives, for example by using an inverse thermo-reversible gel. (Fu et al., 2011a) Recently, Eqtesadi et al. showed that the use of polyelectrolytes and the control of the pH may be a difficult approach for bioglass inks, because of the glass dissolution and leaching of ions in water. In this case, carboxymethyl cellulose was successfully used as an additive to disperse the glass powder and to obtain a suitable rheological behavior. (Eqtesadi et al., 2014) Another possibility is the formulation of a ceramic ink containing a polymeric binder and plasticizer (e.g. PVB and PEG), which can be added up to 23 wt% (relative to the ceramic phase). (de Sousa and Evans, 2003) For fine lattice structures, defects generated by debinding were not reported. These variations of Robocasting have been mostly denominated “direct ink writing” (DIW) technologies.

Typical nozzle sizes are in the range 100-1000  $\mu\text{m}$  and, after drying, the material has a high green density (up to 60%), which allows to achieve an almost complete densification upon sintering. The combination of fine and dense filaments makes the technology particularly attractive for the production of components suitable for several applications, based on structural and functional ceramics.

(i) Porous components

Stuecker et al. reported the production of mullite porous meshes with 100–1000  $\mu\text{m}$  pore sizes and 225–1000  $\mu\text{m}$  filament diameter, obtaining a relative green strut density of 55% and a sintered strut density of 96%. (Stuecker et al., 2003) Smay et al. produced PZT periodic lattices with a diameter

of 200–400  $\mu\text{m}$ , consisting of linear or radial arrays. (Smay et al., 2002) The rod spacing varied from 300 to 1200  $\mu\text{m}$ , thus determining spanning features. The same material system has been used more recently to produce PZT arrays for ultrasonic sensing applications in the 2–30 MHz frequency range. (Smay et al., 2004) These arrays were densified and infiltrated with an epoxy resin to fabricate PZT–polymer composites with 2–2 connectivity. Smay et al. also demonstrated the DIW of ternary mixtures of  $\text{BaTiO}_3$ ,  $\text{BaZrO}_3$ ,  $\text{SrTiO}_3$  by using a nozzle mixer. (Smay et al., 2007) Furthermore, they produced Ni- $\text{BaTiO}_3$  metal-ceramic multilayer structures by using an array of single nozzles, demonstrating that by this technique it is possible to fabricate graded and multi-material porous structures.

Also for this fabrication method, a major part of the research has focused on the shaping of bioceramics into porous scaffolds. Genet et al. modelled the compressive strength of HA porous scaffolds based on a Weibull approach. (Genet et al., 2013) They could fit well experimental data showing a decrease in compressive strength upon increasing rod spacing (i.e. porosity), keeping a constant rod diameter. Interestingly, even when the rod spacing (400–985  $\mu\text{m}$ ) and diameter (200–610  $\mu\text{m}$ ) were varied in order to keep the porosity constant (45 vol%), there was almost a four folds decrease in strength as the rod diameter increased. Franco et al. formulated an ink containing a thermo-reversible gel which had low viscosity at low extrusion temperature and underwent a quick gelation following deposition in a warm (60°C) oil bath. (Franco et al., 2010) They produced HA, TCP and biphasic calcium phosphate (BCP) scaffolds and found that the micro-porosity in the struts varied in a wide range of 5–40% as the content of thermos-reversible gel was increased, and the bending strength decreased accordingly from ~25 MPa to ~2 MPa.

Miranda et al. produced HA scaffolds which had 39% total porosity and 15% strut micro-porosity, and studied the fracture modes under uniaxial compression. (Miranda et al., 2007) These scaffolds had a compressive strength of ~50 MPa, and in a similar work it was shown that this value was doubled after two weeks immersion in simulated body fluid (SBF). (Miranda et al., 2008) Fu et al. produced particularly strong bioglass scaffolds with completely dense rods of 100  $\mu\text{m}$  diameter and a total porosity of 60%. (Fu et al., 2011b) These scaffolds had unidirectional pores and, as expected, anisotropic mechanical properties, reaching 136 MPa in the channels direction and 55 MPa in perpendicular direction. The dependence of the compressive strength on the porosity in the 60–80% range was also in good agreement with the Gibson-Ashby model for closed-cells cellular ceramics. (“Cellular Solids Structure and Properties | Materials science,” n.d.)

It is worth noting, however, that by DIW it is also possible to obtain scaffolds with porous struts by adding a porogen to the ceramic paste. (Cesarano et al., 2005; Dellinger et al., 2007) Dellinger et al. added PMMA microspheres to the ink and produced scaffolds with three levels of porosity:

macropores (100–600  $\mu\text{m}$ ) were designed by controlling the arrangement and spacing between rods of HA; micropores (1–30  $\mu\text{m}$ ) were produced within the rods by including PMMA microspheres; submicron pores (less than 1  $\mu\text{m}$ ) were the result of incomplete sintering. (Dellinger et al., 2007) A further degree of versatility for this 3D printing technique can be achieved when using extrusion nozzles which enable the fabrication of cross-sections different from the standard circular one, such as square, hexagonal and other complex micron-sized geometries, (Lewis, 2006) or even hollow filaments. (Schlordt et al., 2013)

In parallel with the extrusion of ceramic pastes, and in analogy with the most popular process used for the production of polymeric components, another approach has been developed: the fused deposition modelling of ceramics (FDM). This technique is based on the extrusion of a mixture of a ceramic powder mixed with a significant amount of a polymer, which is melted during the extrusion because the printing head is heated, and solidifies by cooling immediately after in order to prevent deformation of the filament. Ideally, in analogy with FDM of conventional polymers, a continuous filament should be produced and fed to the printing head, but it is very difficult to prepare a filament with a high loading of ceramic particles that is not brittle and can be collected in spools to be continuously supplied to the printing head. After printing, the polymeric binder is burnt out and the ceramic phase is sintered. Grida et al. extruded a mixture of 55 vol% zirconia in wax through nozzles with diameter between 76 and 510  $\mu\text{m}$ . (Grida and Evans, 2003) The minimum diameter of the nozzles is usually larger in FDM than in DIW. The same authors observed that fine log-pile structures could be produced with a 100  $\mu\text{m}$  diameter filament but not with a 76  $\mu\text{m}$  filament. The reason was that the latter filament solidified too quickly in ambient air. Park et al. instead extruded 40 wt% HA mixed with PCL at 100°C through nozzles with diameter 400–600  $\mu\text{m}$ . (Park et al., 2011) They also measured the influence of the deposition pattern on the compressive modulus and they studied the attachment and proliferation of osteoblast-like cells. Kalita et al. similarly produced composites polypropylene-TCP composites by FDM, and obtained scaffolds with a compressive strength of 12.7 MPa for 36% total porosity and a pore size of 160  $\mu\text{m}$ . (Kalita et al., 2003) Bandyopadhyay et al. investigated the processing of piezocomposites by FDM, both using a negative approach (producing a polymeric mold and filling it with a ceramic slurry), and a positive approach, extruding a polymeric filament loaded with 50-55 vol% PZT powder. A spool of filament (1.75 mm in diameter) was first produced and extruded through the nozzle of a commercial FDM 3D-printer, at a temperature of 140-200°C, in order to produce a 3-3 piezocomposite ladder structure after sintering and impregnation with epoxy resin. (Bandyopadhyay et al., 1997) At Rutgers University (New Jersey, USA), an FDM apparatus has been developed

which is able to deposit up to four different materials in the same layers, employing four deposition units. (M.A. Jafari et al., 2000) Jafari et al., in the same work also produced a multilayer piezoelectric component transducer composed of soft and hard PZT, and they suggested the fabrication of components based even more complex composite materials, for example through the simultaneous deposition of ceramic, metal, electrode and fugitive phases.

## (ii) Monolithic components

Previously, we mentioned that extrusion-based AM produces potentially dense struts; however, there are issues when this process is used to produce monolithic ceramics, according to our definition. First of all, in technologies which make use of a high amount of polymeric binder, such as FDM, the debinding is problematic. Even for DIW, which uses a feedstock which is almost free of organics, the stacking of filaments creates a textured structure which is far from that of a homogeneous ceramic monolith produced by traditional ceramic technologies and this, as a consequence, affects also the surface quality and the mechanical properties of the printed part. As an example, which also illustrates the difference between AM technologies for ceramics in terms of surface finish of the printed part, we show in Figure 3 images of a zirconia impeller produced by SL (Figure 3a) and of alumina crucibles (Figure 3b). Note that, with SL, a much smoother surface can be obtained, leading to parts with excellent strength.

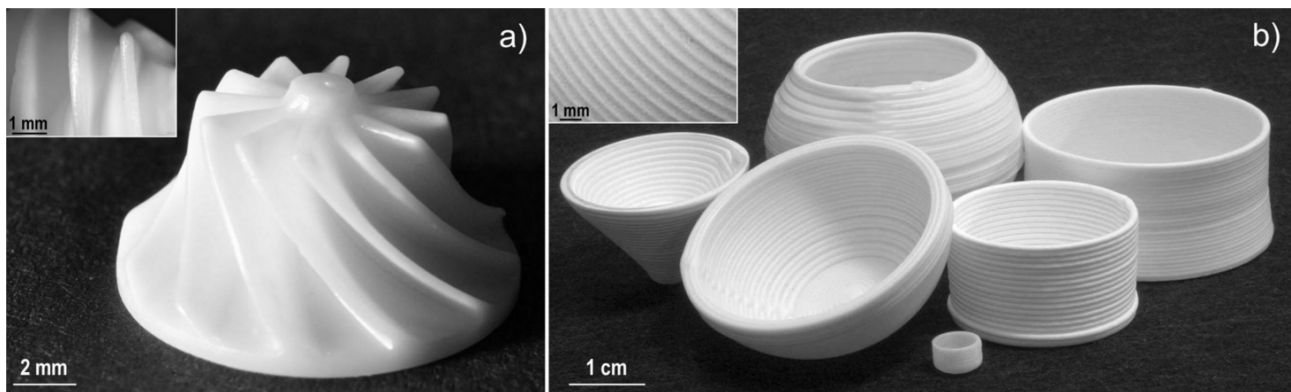


**Figure 3.** Optical photographs of: a) zirconia impeller produced by stereolithography (image courtesy of Lithoz GmbH, Austria); b) alumina crucibles and labware produced by Robocasting (image courtesy of Joe Cesarano, Robocasting Enterprises, USA).

We should also mention that it is possible to couple LOM with computer numerical control (CNC) machining that, at the same time, shapes the object and produces a good surface finish. (Travitzky et al., 2014) In any case, the surface texture is not always problematic, but since it is a specific characteristic of these extrusion-based technologies, it has to be taken into account when designing

a component. Concluding, extrusion-based AM technologies are particularly suitable for producing arrays of separate struts, but are not able to produce proper monolithic ceramics according to a most general definition.

### **II.I.III Negative AM technologies**

While most current research focuses on the use of AM technologies that can directly produce ceramic components, negative replica methods are attractive because they can overcome at least some of the limitations in the physical, functional and geometrical characteristics of components produced. In this approach, a sacrificial polymeric mold is fabricated by AM and then, generally, impregnated with a ceramic slurry. After polymer removal (by decomposition, burn-out or dissolution) and sintering, a ceramic component is obtained. The fabrication of molds by AM adds a step to the processing route, but it allows the use of AM technologies for polymeric materials, some of which are at a greater stage of development compared to AM of ceramics, implying an easier process and often better resolution and surface quality. We should also note that negative replica methods have been long used for the casting of metals, by producing using AM either a ceramic mold or a wax pattern for the investment casting process. (Munish Chhabra and Rupinder Singh, 2011)

Almost every AM technology can be used to fabricate the mold. Detsch et al. used a printer which deposits dropwise a wax, and impregnated the wax mold with a HA slurry. (Detsch et al., 2008) They also replicated a similar geometry by Robocasting, obtaining scaffolds with 44% porosity in the case of negative AM and 37% for the sample produced by Robocasting. In both cases, the pore size and strut diameter were 300  $\mu\text{m}$  and 500  $\mu\text{m}$  respectively, and the strut relative density reached 96% after sintering, indicating the two approaches are fully interchangeable.

A similar fabrication route was followed to produce by SL epoxy molds to generate  $\text{TiO}_2/\text{SiO}_2$  diamond structures for application as photonic crystals. (Yin et al., 2004) SL has also been used to produce resin molds for HA scaffolds with 50% geometrical porosity; in this case, a gel-casting technique was employed to improve the strength of the ceramic green body. (Woesz et al., 2005)

Bose et al. produced molds by fused deposition modelling (FDM) of a commercial thermoplastic polymer, which were subsequently impregnated with TCP or  $\text{Al}_2\text{O}_3$  slurries in order to produce porous scaffolds, and investigated the influence of the pore size (300-500  $\mu\text{m}$ ) and porosity (25-45%) on in-vitro cell tests. (Bose et al., 2003) Guo et al. instead produced polystyrene molds by SLS, which were then used as molds for PZT ceramic components obtained by gelcasting; the selection of the polymer and of the decomposition thermal treatment is essential to avoid deformation of the parts, which was instead observed when using molds produced by FDM of ABS

polymer. (Guo et al., 2004) Ortona et al. applied a technology (“Polyjet”) which dropwise deposits a photo-curable resin to produce a polymeric template possessing a complex, regular three dimensional cellular structure. (Ortona et al., 2012) In this case, the polymeric template was coated with a SiC slurry and after pyrolysis it was reactively infiltrated with molten Si to generate RBSiC cellular structures with hollow struts. Finally, Franchin et. al used FDM to fabricate polymeric scaffolds which were infiltrated by a geopolymer slurry, resulting in parts with different pore geometries. (Franchin and Colombo, 2015)

In this work of thesis, two different approaches have been followed. In a first project, a powder composed of a preceramic polymer with or without fillers has been 3d-printed using a binder jetting technique. In a second project, pastes of preceramic polymers and fillers have been selectively deposited by means of an extrusion-based technology through a syringe. The former falls into the “jetting of binder” category and specifically the “powder-based three-dimensional printing”; the second falls into the category of “extrusion” of a paste.

It seems useful in this context to introduce an overview on preceramic polymers in the next paragraph.

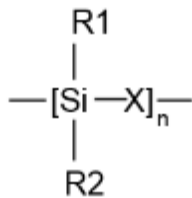
## **II.II Polymer-derived ceramics**

Preceramic polymers form a special class of polymers which can be converted to a ceramic material with a high mass yield. Ceramics produced from these polymeric precursors are usually denoted as “polymer-derived ceramics”.

In the last decades, this class of materials has attracted the attention of the scientific and industrial community due to a combination of outstanding material and processing properties. Polymer-derived ceramics can be produced in a wide range of compositions depending on the precursor used. The most known are Si-based ceramics such as SiCN, SiC, SiOC or more complex quaternary systems like SiOCN or SiBCN. Some of these compositions, e.g., SiOC, are unique because they cannot be produced by any other way but the molecular route. Other systems, such as SiC, are very interesting because it is possible to produce components at much lower processing temperatures (1100–1300 °C) compared to traditional powder-based ceramic technology. The most noteworthy properties of polymer-derived ceramics are excellent oxidation resistance and good thermo-mechanical properties up to very high temperatures, even 1500 °C or higher, besides special functional properties such as piezoresistivity or luminescence (Colombo et al., 2010) (Colombo, 2010). The other evident advantage of using a polymeric precursor is that the material can be

shaped using a wide range of polymer-forming technologies, which allows avoiding the general drawbacks and shaping limitations of the traditional ceramic processing. Forming techniques that have been applied to preceramic polymers are extrusion, injection molding, foaming, joining, infiltration, pressing, coating, spinning, and many others.

Preceramic polymers are mainly silicon-based and their chemical composition can be simplified and represented as:



where X determines the polymer backbone and thus its class. Specifically:

<b>X group</b>	<b>Polymer class</b>
X= Si	Poly(organosilanes)
X= CH <sub>2</sub>	Poly(organocarbosilanes)
X= O	Poly(organosiloxanes)
X= NH	Poly(organosilazanes)
X= [N=C=N]	Poly(organosilylcarbodiimides)

R1 and R2 are organic side groups which influence the functional properties of the polymer, such as viscosity, and also important because they can contribute to the final chemistry of the corresponding polymer-derived ceramic by providing carbon in the structure.

Other more complex preceramic polymer systems exist and have been reviewed in literature (Colombo et al., 2010) and it is not in the scope of this thesis to extensively introduce all of them, therefore the interested reader will find useful information in the bibliography.

A standard procedure for the production of polymer-derived ceramics comprises three steps:

- 1) **Shaping of the preceramic polymer** into the component's shape. This step generally takes advantage of the polymeric nature of the material, therefore plastic-forming technologies can be used.
- 2) **Cross-linking**. The material is cured forming an unmeltable thermoset, which is able to retain its shape during the polymer-to-ceramic conversion. Cross-linking can be often

achieved thermally (usually at  $T < 200^{\circ}\text{C}$ ) during shaping by carefully controlling the rheology of the system by the addition of a catalyst and by regulating temperature and time. In specific cases there are alternative ways of curing the material as well, such as oxidative treatment, e-beam curing, UV-curing or treatment in alkaline solution (Perale et al., 2008). Cross-linking is also important because it increases the ceramic yield by forming a more stable structure which prevents the evaporation of oligomers during heat treatment. This in turns implies a lower gas release and thus a lower formation of bubbles and possibly defects in the material.

- 3) **Polymer-to-ceramic conversion.** During heating at higher temperature, the polymer starts to decompose and organic groups are released. The specific process depends on the chemistry of the polymer, treatment atmosphere, presence of fillers, heating conditions etc. In most cases the conversion is complete at about  $1000^{\circ}\text{C}$ , giving a completely ceramic part as result. The composition clearly depends on the system in use: in inert atmosphere, for example, polycarbosilanes give an amorphous SiC structure, polysiloxanes and polysilsesquioxanes a SiCO amorphous structure and polysilazanes an amorphous SiCN. These phases are particularly stable to crystallization compared to most other amorphous materials, even though heating at high temperature ( $> 1300^{\circ}\text{C}$ ) eventually leads to crystallization reactions and/or decomposition (e.g. by carbothermal reactions).

As for cross-linking, there are alternative processes that allow the polymer-to-ceramic transformation, such as ion-irradiation or local heating by means of a laser source, but these applications will not be considered in this work.

During the polymer-to-ceramic conversion, decomposition leads to gas development and a high shrinkage, often leading to massive cracking of bulk parts. One of the most successful strategies to avoid this drawback is the addition of fillers to the polymer. There are mainly two types of fillers:

- 1) Passive fillers: they do not react neither with the polymer residue nor with the atmosphere, thus they are simply replacing part of the polymer volume with a stable material which is not subject to decomposition reactions in the desired temperature range. This strategy obviously does not allow to compensate completely for the shrinkage and cracking of the polymer, but it is aimed to reducing the total shrinkage and gas release of the system.
- 2) Active fillers: they react with the ceramic residue from the polymer, or with its decomposition products, and/or with the treatment atmosphere. In particular the group of Professor Greil devoted numerous studies on the realization of compositions with almost zero shrinkage, by addition of transition metals as active fillers (Greil, 1998) (Greil and Seibold, 1992). These metals can react with the decomposition products from the polymer



forming the corresponding metal carbide, or with a reactive atmosphere, e.g. nitrogen to form a metal nitride.

A different approach for using active fillers is to use a filler which can react directly with the ceramic residue from the polymer rather than with its decomposition products. A very interesting application is the pyrolysis of a preceramic polymer in oxidizing atmosphere, giving a reactive SiO<sub>2</sub> ceramic residue which can be reacted with an active filler to generate a desired silicate phase.

This last method has been widely applied by the working group of Professors Colombo and Bernardo in Padova, which developed different silicate ceramic compositions, both technical ceramics (mullite (Bernardo et al., 2006), zircon, cordierite, SiAlON (Colombo et al., 2013)) and bioceramics (wollastonite (Bernardo et al., 2012), hardystonite (Bernardo et al., 2014), hardystonite (Elsayed et al., 2014)). The use of nano-sized active fillers increased their reactivity and allowed the formation of the desired phases with high purity and at a lower temperature compared to the formation of these phases through a standard ceramic processing technology. For example mullite was produced at temperatures as low as 1250°C, while temperatures above 1500°C are needed with the use of traditional raw materials.

A specific preceramic polymer has been used in most experiments part of this work of thesis, which will be discussed in chapters 1,2 and 3. This polymer is a commercial product labelled “MK” (Wacker Chemie, Germany) and it will be referred to with this name from here on.

It is a poly(organosilsesquioxane), which has a characteristic -Si-(O)<sub>1.5</sub>- backbone and methyl lateral groups. This polymer has a T<sub>g</sub> of 40-60°C, but it is also functionalized with approximately 2 mol% hydroxyl and ethoxy groups (Harshe, 2004), which allows a cross-linking reaction with release of water and ethanol. Cross-linking is usually thermally activated at temperatures 150-200°C for practical applications, but the reaction can be accelerated by the addition of an appropriate catalyst. In this context it is worth noting that the use of a catalyst is not problematic if a high amount of fillers is mixed with the polymer; in this case, the fillers prevent the structure from collapsing even when the temperature surpasses the polymer’s T<sub>g</sub>.

The reactions of formation of wollastonite and hardystonite from a mixture of preceramic polymer and fillers are reported in the following, since specifically these two ceramic phases have been investigated in chapters 2 and 3.



## References

- ASTM Standard F2792, 2012. Standard Terminology for Additive Manufacturing Technologies, ASTM International, West Conshohocken, PA, 2012.
- Bak, D., 2003. Rapid prototyping or rapid production? 3D printing processes move industry towards the latter. *Assem. Autom.* 23, 340–345. doi:10.1108/01445150310501190
- Bandyopadhyay, A., Panda, R.K., Janas, V.F., Agarwala, M.K., Danforth, S.C., Safari, A., 1997. Processing of Piezocomposites by Fused Deposition Technique. *J. Am. Ceram. Soc.* 80, 1366–1372. doi:10.1111/j.1151-2916.1997.tb02993.x
- Bergmann, C., Lindner, M., Zhang, W., Koczur, K., Kirsten, A., Telle, R., Fischer, H., 2010. 3D printing of bone substitute implants using calcium phosphate and bioactive glasses. *J. Eur. Ceram. Soc.* 30, 2563–2567. doi:10.1016/j.jeurceramsoc.2010.04.037
- Bernardo, E., Carlotti, J.-F., Dias, P.M., Fiocco, L., Colombo, P., Treccani, L., Hess, U., Rezwan, K., 2014. Novel akermanite-based bioceramics from preceramic polymers and oxide fillers. *Ceram. Int.* 40, 1029–1035. doi:10.1016/j.ceramint.2013.06.100
- Bernardo, E., Colombo, P., Cacciotti, I., Bianco, A., Bedini, R., Pecci, R., Pardun, K., Treccani, L., Rezwan, K., 2012. Porous wollastonite–hydroxyapatite bioceramics from a preceramic polymer and micro- or nano-sized fillers. *J. Eur. Ceram. Soc.* 32, 399–408.
- Bernardo, E., Colombo, P., Pippel, E., Woltersdorf, J., 2006. Novel mullite synthesis based on alumina nanoparticles and a preceramic polymer. *J. Am. Ceram. Soc.* 89, 1577–1583.
- Bertan, F.M., Montedo, O.R.K., Rambo, C.R., Hotza, D., de Oliveira, A.P.N., 2009. Extruded ZrSiO<sub>4</sub> particulate-reinforced LZSA glass–ceramics matrix composite. *J. Mater. Process. Technol.* 209, 1134–1142. doi:10.1016/j.jmatprotec.2008.03.018
- Bose, S., Darsell, J., Kintner, M., Hosick, H., Bandyopadhyay, A., 2003. Pore size and pore volume effects on alumina and TCP ceramic scaffolds. *Mater. Sci. Eng. C* 23, 479–486. doi:10.1016/S0928-4931(02)00129-7
- Bourell, D.L., Marcus, H.L., Barlow, J.W., Beaman, J.J., 1992. Selective laser sintering of metals and ceramics. *Int. J. Powder Metall.* 28, 369–381.
- Butscher, A., Bohner, M., Doebelin, N., Galea, L., Loeffel, O., Müller, R., 2013. Moisture based three-dimensional printing of calcium phosphate structures for scaffold engineering. *Acta Biomater.* 9, 5369–5378.
- Butscher, A., Bohner, M., Hofmann, S., Gauckler, L., Müller, R., 2011. Structural and material approaches to bone tissue engineering in powder-based three-dimensional printing. *Acta Biomater.* 7, 907–920. doi:10.1016/j.actbio.2010.09.039
- Calvert, P., 2007. Printing Cells. *Science* 318, 208–209. doi:10.1126/science.1144212
- Cappi, B., Özkol, E., Ebert, J., Telle, R., 2008. Direct inkjet printing of Si<sub>3</sub>N<sub>4</sub>: Characterization of ink, green bodies and microstructure. *J. Eur. Ceram. Soc.* 28, 2625–2628. doi:10.1016/j.jeurceramsoc.2008.03.004
- Castilho, M., Gouveia, B., Pires, I., Rodrigues, J., Pereira, M., Campbell, R.I., Campbell, R.I., 2014a. The role of shell/core saturation level on the accuracy and mechanical characteristics of porous calcium phosphate models produced by 3Dprinting. *Rapid Prototyp. J.* 21.
- Castilho, M., Moseke, C., Ewald, A., Gbureck, U., Groll, J., Pires, I., Teßmar, J., Vorndran, E., 2014b. Direct 3D powder printing of biphasic calcium phosphate scaffolds for substitution of complex bone defects. *Biofabrication* 6, 015006. doi:10.1088/1758-5082/6/1/015006
- Cellular Solids Structure and Properties | Materials science [WWW Document], n.d. . Camb. Univ. Press. URL <http://www.cambridge.org/us/academic/subjects/engineering/materials-science/cellular-solids-structure-and-properties-2nd-edition> (accessed 2.9.15).
- Cesarano, J., Calvert, P.D., 2000. Inventor; Sandia Corporation, Assignee. Freeforming objects with low-binder slurry. US Patent 6027326 A; 2000 February 22. US6027326 A.
- Cesarano, J., Dellinger, J.G., Saavedra, M.P., Gill, D.D., Jamison, R.D., Grosser, B.A., Sinn-Hanlon, J.M., Goldwasser, M.S., 2005. Customization of Load-Bearing Hydroxyapatite

- Lattice Scaffolds. *Int. J. Appl. Ceram. Technol.* 2, 212–220. doi:10.1111/j.1744-7402.2005.02026.x
- Cesaretti, G., Dini, E., De Kestelier, X., Colla, V., Pambaguian, L., 2014. Building components for an outpost on the Lunar soil by means of a novel 3D printing technology. *Acta Astronaut.* 93, 430–450. doi:10.1016/j.actaastro.2013.07.034
- Chartier, T., Chaput, C., Doreau, F., Loiseau, M., 2002. Stereolithography of structural complex ceramic parts. *J. Mater. Sci.* 37, 3141–3147. doi:10.1023/A:1016102210277
- Chartier, T., Delhomme, E., Baumard, J.F., Veltl, G., Ducloux, F., 2001. Injection moulding of hollow silicon nitride parts using fusible alloy cores. *Ceram. Int.* 27, 821–827.
- Chartier, T., Duterte, C., Delhote, N., Baillargeat, D., Verdeyme, S., Delage, C., Chaput, C., 2008. Fabrication of Millimeter Wave Components Via Ceramic Stereo-and Microstereolithography Processes. *J. Am. Ceram. Soc.* 91, 2469–2474.
- Chumnanklang, R., Panyathanmaporn, T., Sitthiseripratip, K., Suwanprateeb, J., 2007. 3D printing of hydroxyapatite: Effect of binder concentration in pre-coated particle on part strength. *Mater. Sci. Eng. C* 27, 914–921. doi:10.1016/j.msec.2006.11.004
- Chu, T.M.G., Orton, D.G., Hollister, S.J., Feinberg, S.E., Halloran, J.W., 2002. Mechanical and in vivo performance of hydroxyapatite implants with controlled architectures. *Biomaterials* 23, 1283–1293.
- Colombo, P., 2010. Polymer derived ceramics: from nano-structure to applications. DEStech Publications, Inc.
- Colombo, P., Bernardo, E., Parciannello, G., 2013. Multifunctional advanced ceramics from preceramic polymers and nano-sized active fillers. *J. Eur. Ceram. Soc.* 33, 453–469. doi:10.1016/j.jeurceramsoc.2012.10.006
- Colombo, P., Mera, G., Riedel, R., Sorarù, G.D., 2010. Polymer-Derived Ceramics: 40 Years of Research and Innovation in Advanced Ceramics. *J. Am. Ceram. Soc.* 93, 1805–1837. doi:10.1111/j.1551-2916.2010.03876.x
- Crump, S., 1992. Inventor; Stratasys, Assignee. Apparatus and method for creating three-dimensional objects. US Patent 5121329 A; 1992 June 9.
- Cui, X., Ouyang, S., Yu, Z., Wang, C., Huang, Y., 2003. A study on green tapes for LOM with water-based tape casting processing. *Mater. Lett.* 57, 1300–1304. doi:10.1016/S0167-577X(02)00975-8
- Deckard, C.R., 1989. Inventor; Board of Regents, The University of Texas System, Assignee. Method and apparatus for producing parts by selective sintering. US Patent 4,863,538; September 5.
- Deckers, J., Vleugels, J., Kruth, J.-P., 2014. Additive manufacturing of ceramics: A review [WWW Document]. URL <https://lirias.kuleuven.be/handle/123456789/459498> (accessed 2.16.15).
- Dellinger, J.G., Cesarano, J., Jamison, R.D., 2007. Robotic deposition of model hydroxyapatite scaffolds with multiple architectures and multiscale porosity for bone tissue engineering. *J. Biomed. Mater. Res. A* 82A, 383–394. doi:10.1002/jbm.a.31072
- De Sousa, F.C.G., Evans, J.R.G., 2003. Sintered Hydroxyapatite Latticework for Bone Substitute. *J. Am. Ceram. Soc.* 86, 517–519. doi:10.1111/j.1151-2916.2003.tb03332.x
- Detsch, R., Uhl, F., Deisinger, U., Ziegler, G., 2008. 3D-Cultivation of bone marrow stromal cells on hydroxyapatite scaffolds fabricated by dispense-plotting and negative mould technique. *J. Mater. Sci. Mater. Med.* 19, 1491–1496. doi:10.1007/s10856-007-3297-x
- Elsayed, H., Zocca, A., Bernardo, E., Gomes, C.M., Günster, J., Colombo, P., 2014. Development of bioactive silicate-based glass-ceramics from preceramic polymer and fillers. *J. Eur. Ceram. Soc.* under review.
- Eqtesadi, S., Motealleh, A., Miranda, P., Pajares, A., Lemos, A., Ferreira, J.M.F., 2014. Robocasting of 45S5 bioactive glass scaffolds for bone tissue engineering. *J. Eur. Ceram. Soc.* 34, 107–118. doi:10.1016/j.jeurceramsoc.2013.08.003

- Fielding, G.A., Bandyopadhyay, A., Bose, S., 2012a. Effects of silica and zinc oxide doping on mechanical and biological properties of 3D printed tricalcium phosphate tissue engineering scaffolds. *Dent. Mater.* 28, 113–122. doi:10.1016/j.dental.2011.09.010
- Fielding, G.A., Bandyopadhyay, A., Bose, S., 2012b. Effects of silica and zinc oxide doping on mechanical and biological properties of 3D printed tricalcium phosphate tissue engineering scaffolds. *Dent. Mater.* 28, 113–122. doi:10.1016/j.dental.2011.09.010
- Franchin, G., Colombo, P., 2015. Porous geopolymer components through inverse replica of 3D printed sacrificial templates. *J Ceram Sci Tech* in press.
- Franco, J., Hunger, P., Launey, M.E., Tomsia, A.P., Saiz, E., 2010. Direct-Write Assembly of Calcium Phosphate Scaffolds Using a Water-Based Hydrogel. *Acta Biomater.* 6, 218–228. doi:10.1016/j.actbio.2009.06.031
- Friedel, T., Travitzky, N., Niebling, F., Scheffler, M., Greil, P., 2005. Fabrication of polymer derived ceramic parts by selective laser curing. *J. Eur. Ceram. Soc., European Materials Research Society 2004, Symposium Q: Polymer Derived Ceramics (PDCs) 25*, 193–197. doi:10.1016/j.jeurceramsoc.2004.07.017
- Fu, Q., Saiz, E., Tomsia, A.P., 2011a. Direct ink writing of highly porous and strong glass scaffolds for load-bearing bone defects repair and regeneration. *Acta Biomater.* 7, 3547–3554.
- Fu, Q., Saiz, E., Tomsia, A.P., 2011b. Bioinspired Strong and Highly Porous Glass Scaffolds. *Adv. Funct. Mater.* 21, 1058–1063. doi:10.1002/adfm.201002030
- Fu, Z., Schlier, L., Travitzky, N., Greil, P., 2013. Three-dimensional printing of SiSiC lattice truss structures. *Mater. Sci. Eng. A* 560, 851–856. doi:10.1016/j.msea.2012.09.107
- Genet, M., Houmard, M., Eslava, S., Saiz, E., Tomsia, A.P., 2013. A two-scale Weibull approach to the failure of porous ceramic structures made by robocasting: Possibilities and limits. *J. Eur. Ceram. Soc.* 33, 679–688. doi:10.1016/j.jeurceramsoc.2012.11.001
- Giassi, L., Hotza, D., Alarcon, O.E., Fredel, M.C., Novaes de Oliveira, A.P., 2005. Sintering and Crystallization of LZSA Glass Powder Compacts Formed by Injection Moulding. *Am. Ceram. Soc. Bull.* 84, 9301–9306.
- Gomes, C.M., Oliveira, A.P.N., Hotza, D., Travitzky, N., Greil, P., 2008. LZSA glass-ceramic laminates: Fabrication and mechanical properties. *J. Mater. Process. Technol.* 206, 194–201. doi:10.1016/j.jmatprotec.2007.12.011
- Gomes, C., Travitzky, N., Greil, P., Acchar, W., Birol, H., Oliveira, A.P.N. de, Hotza, D., 2011. Laminated object manufacturing of LZSA glass-ceramics. *Rapid Prototyp. J.* 17, 424–428. doi:10.1108/13552541111184152
- Greil, P., 1998. Near Net Shape Manufacturing of Polymer Derived Ceramics. *J. Eur. Ceram. Soc.* 18, 1905–1914. doi:10.1016/S0955-2219(98)00129-0
- Greil, P., Seibold, M., 1992. Modelling of dimensional changes during polymer-ceramic conversion for bulk component fabrication. *J. Mater. Sci.* 27, 1053–1060. doi:10.1007/BF01197660
- Grida, I., Evans, J.R., 2003. Extrusion freeforming of ceramics through fine nozzles. *J. Eur. Ceram. Soc.* 23, 629–635.
- Griffith, M.L., Halloran, J.W., 1996. Freeform fabrication of ceramics via stereolithography. *J. Am. Ceram. Soc.* 79, 2601–2608.
- Guo, D., Li, L., Cai, K., Gui, Z., Nan, C., 2004. Rapid Prototyping of Piezoelectric Ceramics via Selective Laser Sintering and Gelcasting. *J. Am. Ceram. Soc.* 87, 17–22. doi:10.1111/j.1151-2916.2004.tb19938.x
- Harshe, R.R., 2004. Synthesis and processing of amorphous Si(Al)OC bulk ceramics: high temperature properties and applications (PhD dissertation). Darmstadt TU.
- Homa, J., Schwentenwein, M., 2015. A novel additive manufacturing technology for high-performance ceramics. *Adv. Process. Manuf. Technol. Nanostructured Multifunct. Mater. CESP Vol. 35* 33.
- <http://www.ceradrop.fr/en/>; accessed on 28/02/2015, 2015.
- <http://www.voxeljet.de/en/services/castings/>; accessed on 28/02/2015, 2015.

- Huson, D., Hoskins, S., 2014. 3D Printed Ceramics for Tableware, Artists/Designers and Specialist Applications. *Key Eng. Mater.* 608, 351–357. doi:10.4028/www.scientific.net/KEM.608.351
- John Kechagias, 2007. An experimental investigation of the surface roughness of parts produced by LOM process. *Rapid Prototyp. J.* 13, 17–22. doi:10.1108/13552540710719172
- Jones, N., 2012. Science in three dimensions: The print revolution. *Nature* 487, 22–23. doi:10.1038/487022a
- J-P. Kruth, P. Mercelis, J. Van Vaerenbergh, L. Froyen, M. Rombouts, 2005. Binding mechanisms in selective laser sintering and selective laser melting. *Rapid Prototyp. J.* 11, 26–36. doi:10.1108/13552540510573365
- Juste, E., Petit, F., Lardot, V., Cambier, F., 2014. Shaping of ceramic parts by selective laser melting of powder bed. *J. Mater. Res.* 29, 2086–2094.
- Kalita, S.J., Bose, S., Hosick, H.L., Bandyopadhyay, A., 2003. Development of controlled porosity polymer-ceramic composite scaffolds via fused deposition modeling. *Mater. Sci. Eng. C* 23, 611–620. doi:10.1016/S0928-4931(03)00052-3
- Kamatchi Subramanian, Neal Vail, Joel Barlow, Harris Marcus, 1995. Selective laser sintering of alumina with polymer binders. *Rapid Prototyp. J.* 1, 24–35. doi:10.1108/13552549510086844
- Kirihara, 2014. creation of functional ceramics structures by using stereolithographic 3D printing. *Trans. JWRI* 43.
- Klammert, U., Reuther, T., Jahn, C., Kraski, B., Kübler, A.C., Gbureck, U., 2009. Cytocompatibility of brushite and monetite cell culture scaffolds made by three-dimensional powder printing. *Acta Biomater.* 5, 727–734. doi:10.1016/j.actbio.2008.08.019
- Klosterman, D., Chartoff, R., Graves, G., Osborne, N., Priore, B., 1998. Interfacial characteristics of composites fabricated by laminated object manufacturing. *Compos. Part Appl. Sci. Manuf.* 29, 1165–1174. doi:10.1016/S1359-835X(98)00088-8
- Klosterman, D., Chartoff, R., Osborne, N., Graves, G., 1997. Automated fabrication of monolithic and ceramic matrix composites via laminated object manufacturing (LOM), in: *Solid Freeform Fabrication Symposium Proceedings*. University of Texas at Austin, pp. 537–549.
- Kolan, K.C.R., Leu, M.C., Hilmas, G.E., Brown, R.F., Velez, M., 2011. Fabrication of 13-93 bioactive glass scaffolds for bone tissue engineering using indirect selective laser sintering. *Biofabrication* 3, 025004. doi:10.1088/1758-5082/3/2/025004
- Kollenberg, W., 2014. Keramik und Multi-Material 3D-Druck (ceramic and multi-material 3D-printing). *Keram Z* 66, 233–36.
- Kruth, J.-P., Levy, G., Klocke, F., Childs, T.H.C., 2007. Consolidation phenomena in laser and powder-bed based layered manufacturing. *CIRP Ann.-Manuf. Technol.* 56, 730–759.
- Kumar, S., Kruth, J.-P., 2010. Composites by rapid prototyping technology. *Mater. Des.* 31, 850–856. doi:10.1016/j.matdes.2009.07.045
- Leukers, B., Gülkan, H., Irsen, S.H., Milz, S., Tille, C., Schieker, M., Seitz, H., 2005. Hydroxyapatite scaffolds for bone tissue engineering made by 3D printing. *J. Mater. Sci. Mater. Med.* 16, 1121–1124. doi:10.1007/s10856-005-4716-5
- Leukers, B., Gülkan, H., Irsen, S.H., Milz, S., Tille, C., Seitz, H., Schieker, M., 2005. Biocompatibility of ceramic scaffolds for bone replacement made by 3D printing. *Mater. Werkst.* 36, 781–787. doi:10.1002/mawe.200500968
- Lewis, J.A., 2006. Direct ink writing of 3D functional materials. *Adv. Funct. Mater.* 16, 2193–2204.
- Lewis, J.A., Smay, J.E., Stuecker, J., Cesarano, J., 2006. Direct Ink Writing of Three-Dimensional Ceramic Structures. *J. Am. Ceram. Soc.* 89, 3599–3609. doi:10.1111/j.1551-2916.2006.01382.x
- Ling, G., Yang, H., 2005. Pressureless sintering of silicon nitride with Magnesia and Yttria. *Mater. Chem. Phys.* 90, 31–34. doi:10.1016/j.matchemphys.2004.08.041

- Liu, D.-M., 1997. Influence of porosity and pore size on the compressive strength of porous hydroxyapatite ceramic. *Ceram. Int.* 23, 135–139. doi:10.1016/S0272-8842(96)00009-0
- Liu, F.-H., Shen, Y.-K., Lee, J.-L., 2012. Selective laser sintering of a hydroxyapatite-silica scaffold on cultured MG63 osteoblasts in vitro. *Int. J. Precis. Eng. Manuf.* 13, 439–444. doi:10.1007/s12541-012-0056-9
- Liu, S., Ye, F., Liu, L., Liu, Q., 2015. Feasibility of preparing of silicon nitride ceramics components by aqueous tape casting in combination with laminated object manufacturing. *Mater. Des.* 66, Part A, 331–335. doi:10.1016/j.matdes.2014.10.079
- Löschau, W., Lenk, R., Scharek, S., Teichgraber, M., Nowotny, S., Richter, C., 1999. Prototyping of complex-shaped parts and tools of Si/SiC-ceramics by selective laser sintering. *Adv. Sci. Technol.* B567–B573.
- M.A. Jafari, W. Han, F. Mohammadi, A. Safari, S.C. Danforth, N. Langrana, 2000. A novel system for fused deposition of advanced multiple ceramics. *Rapid Prototyp. J.* 6, 161–175. doi:10.1108/13552540010337047
- Melcher, R., Martins, S., Travitzky, N., Greil, P., 2006. Fabrication of Al<sub>2</sub>O<sub>3</sub>-based composites by indirect 3D-printing. *Mater. Lett.* 60, 572–575. doi:10.1016/j.matlet.2005.09.059
- Miranda, P., Pajares, A., Saiz, E., Tomsia, A.P., Guiberteau, F., 2007. Fracture modes under uniaxial compression in hydroxyapatite scaffolds fabricated by robocasting. *J. Biomed. Mater. Res. A* 83A, 646–655. doi:10.1002/jbm.a.31272
- Miranda, P., Pajares, A., Saiz, E., Tomsia, A.P., Guiberteau, F., 2008. Mechanical properties of calcium phosphate scaffolds fabricated by robocasting. *J. Biomed. Mater. Res. A* 85A, 218–227. doi:10.1002/jbm.a.31587
- Moon, J., Caballero, A.C., Hozer, L., Chiang, Y.-M., Cima, M.J., 2001. Fabrication of functionally graded reaction infiltrated SiC–Si composite by three-dimensional printing (3DP<sup>TM</sup>) process. *Mater. Sci. Eng. A* 298, 110–119. doi:10.1016/S0921-5093(00)01282-X
- Mott, M., Evans, J.R.G., 2001. Solid Freeforming of Silicon Carbide by Inkjet Printing Using a Polymeric Precursor. *J. Am. Ceram. Soc.* 84, 307–13. doi:10.1111/j.1151-2916.2001.tb00655.x
- Mühler, T., Gomes, C.M., Heinrich, J., Günster, J., 2015. Slurry-Based Additive Manufacturing of Ceramics. *Int. J. Appl. Ceram. Technol.* 12, 18–25. doi:10.1111/ijac.12113
- Munish Chhabra, Rupinder Singh, 2011. Rapid casting solutions: a review. *Rapid Prototyp. J.* 17, 328–350. doi:10.1108/13552541111156469
- Ortona, A., D'Angelo, C., Gianella, S., Gaia, D., 2012. Cellular ceramics produced by rapid prototyping and replication. *Mater. Lett.* 80, 95–98. doi:10.1016/j.matlet.2012.04.050
- Özkol, E., Ebert, J., Telle, R., 2010. An experimental analysis of the influence of the ink properties on the drop formation for direct thermal inkjet printing of high solid content aqueous 3Y-TZP suspensions. *J. Eur. Ceram. Soc.* 30, 1669–1678. doi:10.1016/j.jeurceramsoc.2010.01.004
- Özkol, E., Zhang, W., Ebert, J., Telle, R., 2012. Potentials of the “Direct inkjet printing” method for manufacturing 3Y-TZP based dental restorations. *J. Eur. Ceram. Soc.* 32, 2193–2201. doi:10.1016/j.jeurceramsoc.2012.03.006
- Park, S.A., Lee, S.H., Kim, W.D., 2011. Fabrication of porous polycaprolactone/hydroxyapatite (PCL/HA) blend scaffolds using a 3D plotting system for bone tissue engineering. *Bioprocess Biosyst. Eng.* 34, 505–513. doi:10.1007/s00449-010-0499-2
- Penas, O., Zenati, R., Dubois, J., Fantozzi, G., 2001. Processing, microstructure, mechanical properties of Si<sub>3</sub>N<sub>4</sub> obtained by slip casting and pressureless sintering. *Ceram. Int.* 27, 591–596. doi:10.1016/S0272-8842(01)00006-2
- Perale, G., Giordano, C., Daniele, F., Masi, M., Colombo, P., Gottardo, L., Maccagnan, S., 2008. A novel process for the manufacture of ceramic microelectrodes for biomedical applications. *Int. J. Appl. Ceram. Technol.* 5, 37–43.

- Pham, T.A., Kim, D.-P., Lim, T.-W., Park, S.-H., Yang, D.-Y., Lee, K.-S., 2006. Three-Dimensional SiCN Ceramic Microstructures via Nano-Stereolithography of Inorganic Polymer Photoresists. *Adv. Funct. Mater.* 16, 1235–1241. doi:10.1002/adfm.200600009
- P. Regenfuss, A. Streek, L. Hartwig, S. Klötzer, Th. Brabant, M. Horn, R. Ebert, H. Exner, 2007. Principles of laser micro sintering. *Rapid Prototyp. J.* 13, 204–212. doi:10.1108/13552540710776151
- Reitz, G.M., Montedo, O.R.K., Alarcon, O.E., Hotza, D., Novaes de Oliveira, A.P., 2006. Roll Pressed LZSA Glass-Ceramics. *Adv. Sci. Technol.* 45, 442–446. doi:10.4028/www.scientific.net/AST.45.442
- Rodrigues, S.J., Chartoff, R.P., Klosterman, D.A., Agarwala, M., Hecht, N., 2000. Solid freeform fabrication of functional silicon nitride ceramics by laminated object manufacturing, in: *Proceedings from Solid Freeform Fabrication Symposium*.
- Royal Academy of Engineering, 2013. Additive manufacturing:opportunities and constraints. Royal Academy of Engineering.
- Sachs, E.M., Cima, M.J., Caradonna, M.A., Grau, J., Serdy, J.G., Saxton, P.C., Uhland, S.A., Moon, J., 2003. Inventors; Massachusetts Institute Of Technology, Assignee. Jetting layers of powder and the formation of fine powder beds thereby. US Patent 6,596,224; July 22.
- Sachs, E.M., Haggerty, J.S., Cima, M.J., Williams, P.A., 1993. Inventors; Massachussets Institute of Technology, Assignee. Three-dimensional printing techniques. US Patent 5,204,055; April 20. US Patent 5,204,055.
- Schlördt, T., Schwanke, S., Keppner, F., Fey, T., Travitzky, N., Greil, P., 2013. Robocasting of alumina hollow filament lattice structures. *J. Eur. Ceram. Soc.* 33, 3243–3248. doi:10.1016/j.jeurceramsoc.2013.06.001
- Simpson, R.L., Wiria, F.E., Amis, A.A., Chua, C.K., Leong, K.F., Hansen, U.N., Chandrasekaran, M., Lee, M.W., 2008. Development of a 95/5 poly(L-lactide-co-glycolide)/hydroxylapatite and  $\beta$ -tricalcium phosphate scaffold as bone replacement material via selective laser sintering. *J. Biomed. Mater. Res. B Appl. Biomater.* 84B, 17–25. doi:10.1002/jbm.b.30839
- Smay, J.E., Cesarano, J., Lewis, J.A., 2002. Colloidal Inks for Directed Assembly of 3-D Periodic Structures. *Langmuir* 18, 5429–5437. doi:10.1021/la0257135
- Smay, J.E., Cesarano, J., Tuttle, B.A., Lewis, J.A., 2004. Directed Colloidal Assembly of Linear and Annular Lead Zirconate Titanate Arrays. *J. Am. Ceram. Soc.* 87, 293–295. doi:10.1111/j.1551-2916.2004.00293.x
- Smay, J.E., Nadkarni, S.S., Xu, J., 2007. Direct Writing of Dielectric Ceramics and Base Metal Electrodes. *Int. J. Appl. Ceram. Technol.* 4, 47–52. doi:10.1111/j.1744-7402.2007.02118.x
- Stuecker, J.N., Cesarano III, J., Hirschfeld, D.A., 2003. Control of the viscous behavior of highly concentrated mullite suspensions for robocasting. *J. Mater. Process. Technol.* 142, 318–325. doi:10.1016/S0924-0136(03)00586-7
- Sun, W., Dcosta, D.J., Lin, F., El-Raghy, T., 2002. Freeform fabrication of Ti<sub>3</sub>SiC<sub>2</sub> powder-based structures: Part I—Integrated fabrication process. *J. Mater. Process. Technol.* 127, 343–351. doi:10.1016/S0924-0136(02)00284-4
- Suwanprateeb, J., Sanggam, R., Suvannapruk, W., Panyathanmaporn, T., 2009. Mechanical and in vitro performance of apatite–wollastonite glass ceramic reinforced hydroxyapatite composite fabricated by 3D-printing. *J. Mater. Sci. Mater. Med.* 20, 1281–1289. doi:10.1007/s10856-009-3697-1
- Tang, H.-H., Yen, H.-C., 2015. Slurry-based additive manufacturing of ceramic parts by selective laser burn-out. *J. Eur. Ceram. Soc.* 35, 981–987.
- Tan, K.H., Chua, C.K., Leong, K.F., Cheah, C.M., Cheang, P., Abu Bakar, M.S., Cha, S.W., 2003. Scaffold development using selective laser sintering of polyetheretherketone–hydroxyapatite biocomposite blends. *Biomaterials* 24, 3115–3123. doi:10.1016/S0142-9612(03)00131-5
- Teng, W.D., Edirisinghe, M.J., 1998. Development of Ceramic Inks for Direct Continuous Jet Printing. *J. Am. Ceram. Soc.* 81, 1033–1036. doi:10.1111/j.1151-2916.1998.tb02443.x

- Tian, X., Muhler, T., Gomes, C., Gunster, J., Heinrich, J.G., 2011. Feasibility study on rapid prototyping of porcelain products. *J. Ceram. Sci. Technol.* 2, 217–225.
- Tomov, R.I., Krauz, M., Jewulski, J., Hopkins, S.C., Kluczowski, J.R., Glowacka, D.M., Glowacki, B.A., 2010. Direct ceramic inkjet printing of yttria-stabilized zirconia electrolyte layers for anode-supported solid oxide fuel cells. *J. Power Sources* 195, 7160–7167. doi:10.1016/j.jpowsour.2010.05.044
- Travitzky, N., Bonet, A., Dermeik, B., Fey, T., Filbert-Demut, I., Schlier, L., Schlordt, T., Greil, P., 2014. Additive Manufacturing of Ceramic-Based Materials. *Adv. Eng. Mater.* 16, 729–754. doi:10.1002/adem.201400097
- Wang, S., Jia, D., Yang, Z., Duan, X., Tian, Z., Zhou, Y., 2013. Effect of BN content on microstructures, mechanical and dielectric properties of porous BN/Si<sub>3</sub>N<sub>4</sub> composite ceramics prepared by gel casting. *Ceram. Int.* 39, 4231–4237. doi:10.1016/j.ceramint.2012.11.005
- Wätjen, A.M., Gingter, P., Kramer, M., Telle, R., 2014. Novel Prospects and Possibilities in Additive Manufacturing of Ceramics by means of Direct Inkjet Printing. *Adv. Mech. Eng.* 2014, e141346. doi:10.1155/2014/141346
- Wegrzyn, T.F., Golding, M., Archer, R.H., 2012. Food Layered Manufacture: A new process for constructing solid foods. *Trends Food Sci. Technol.* 27, 66–72. doi:10.1016/j.tifs.2012.04.006
- Weiguo Bian, Dichen Li, Qin Lian, Xiang Li, Weijie Zhang, Kunzheng Wang, Zhongmin Jin, 2012. Fabrication of a bio-inspired beta-Tricalcium phosphate/collagen scaffold based on ceramic stereolithography and gel casting for osteochondral tissue engineering. *Rapid Prototyp. J.* 18, 68–80. doi:10.1108/13552541211193511
- Weisensel, L., Travitzky, N., Sieber, H., Greil, P., 2004. Laminated Object Manufacturing (LOM) of SiSiC Composites. *Adv. Eng. Mater.* 6, 899–903. doi:10.1002/adem.200400112
- Weizhao Zhou, Dichen Li, Hui Wang, 2010. A novel aqueous ceramic suspension for ceramic stereolithography. *Rapid Prototyp. J.* 16, 29–35. doi:10.1108/13552541011011686
- Wilkes, J., Hagedorn, Y.-C., Meiners, W., Wissenbach, K., 2013. Additive manufacturing of ZrO<sub>2</sub>-Al<sub>2</sub>O<sub>3</sub> ceramic components by selective laser melting. *Rapid Prototyp. J.* 19, 51–57.
- Windsheimer, H., Travitzky, N., Hofenauer, A., Greil, P., 2007. Laminated Object Manufacturing of Pre-ceramic-Paper-Derived Si<sup>+</sup>SiC Composites. *Adv. Mater.* 19, 4515–4519. doi:10.1002/adma.200700789
- Woesz, A., Rumpler, M., Stampfl, J., Varga, F., Fratzi-Zelman, N., Roschger, P., Klaushofer, K., Fratzi, P., 2005. Towards bone replacement materials from calcium phosphates via rapid prototyping and ceramic gelcasting. *Mater. Sci. Eng. C, NATO Advanced Study Institute (ASI on Learning from Nature How to design New Implantable Biomaterials: From Biomineralization Fundamentals to Biomimetic Materials and Processing Routes) NATO Advanced Study Institute (ASI on Learning from Nature How to design New Implantable Biomaterials: From Biomineralization Fundamentals to Biomimetic Materials and Processing Routes)* 25, 181–186. doi:10.1016/j.msec.2005.01.014
- Wroblewska, G.H., 2001. Structural Ceramics with Complex Shape-Forming Methods, in: 25th Annual Conference on Composites, Advanced Ceramics, Materials, and Structures: A: Ceramic Engineering and Science Proceedings, Volume 22, Issue 3. Wiley Online Library, pp. 43–50.
- Yadroitsev, I., Shishkovsky, I., Bertrand, P., Smurov, I., 2009. Manufacturing of fine-structured 3D porous filter elements by selective laser melting. *Appl. Surf. Sci.* 255, 5523–5527. doi:10.1016/j.apsusc.2008.07.154
- Ye, F., Liu, L., Zhang, J., Iwasa, M., Su, C.-L., 2005. Synthesis of silicon nitride-barium aluminosilicate self-reinforced ceramic composite by a two-step pressureless sintering. *Compos. Sci. Technol.* 65, 2233–2239. doi:10.1016/j.compscitech.2005.04.015



- Yen, H.C., 2014. Experimental studying on development of slurry-layer casting system for additive manufacturing of ceramics. *Int. J. Adv. Manuf. Technol.* 1–11.
- Yin, H., Kirihara, S., Miyamoto, Y., 2004. Fabrication of Ceramic Photonic Crystals with Diamond Structure for Microwave Applications. *J. Am. Ceram. Soc.* 87, 598–601. doi:10.1111/j.1551-2916.2004.00598.x
- Yoo, J., Cima, M.J., Khanuja, S., Sachs, E.M., 1993. Structural ceramic components by 3D printing, in: *Solid Freeform Fabrication Symposium. DTIC Document*, pp. 40–50.
- Yu, J., Wang, H., Zhang, J., 2009. Neural network modeling and analysis of gel casting preparation of porous Si<sub>3</sub>N<sub>4</sub> ceramics. *Ceram. Int.* 35, 2943–2950. doi:10.1016/j.ceramint.2009.04.008
- Zhang, W., Melcher, R., Travitzky, N., Bordia, R.K., Greil, P., 2009. Three-Dimensional Printing of Complex-Shaped Alumina/Glass Composites. *Adv. Eng. Mater.* 11, 1039–1043. doi:10.1002/adem.200900213
- Zhang, Y., He, X., Han, J., Du, S., 1999. Ceramic green tape extrusion for laminated object manufacturing. *Mater. Lett.* 40, 275–279. doi:10.1016/S0167-577X(99)00089-0
- Zocca, A., Elsayed, H., Bernardo, E., Gomes, C.M., Lopez-Heredia, M., Knabe, C., Colombo, P., Gunster, J., submitted. 3D-printed silicate porous bioceramics by using a non-sacrificial preceramic polymer binder. *Biofabrication* (submitted).
- Zocca, A., Gomes, C.M., Mühler, T., Günster, J., 2014. Powder-Bed Stabilization for Powder-Based Additive Manufacturing. *Adv. Mech. Eng.* 2014. doi:10.1155/2014/491581
- Zocca, A., Gomes, C.M., Staude, A., Bernardo, E., Günster, J., Colombo, P., 2013. SiOC ceramics with ordered porosity by 3D-printing of a preceramic polymer. *J. Mater. Res.* 28, 2243–2252. doi:10.1557/jmr.2013.129

# CHAPTER 1

Partially published in:

Zocca A, Gomes CM, Staude A, Bernardo E, Günster J, Colombo P. SiOC ceramics with ordered porosity by 3D-printing of a preceramic polymer. *Journal of Materials Research* 2013; 17 (28), 2243-52.

## **CHAPTER 1**

### **SiOC porous structures produced by powder-based 3D-printing of a preceramic polymer**

#### **1.1 Porous materials**

Porous materials are particularly interesting because they allow to greatly extend the mechanical and functional properties of dense materials, often achieving attractive characteristics for various applications (Colombo, 2008). Porous structures for example can have higher stiffness and strength compared to an equal mass of dense material, thus having better performances as lightweight materials. For this reason they are often found in natural materials such as bone (Wang and Ni, 2003) (Cooper et al., 2004) and wood (Koponen et al., 1991).

The mean pore size (nm to mm), as well as its distribution and the total porosity (from below 20% to more than 90%) can vary in a wide range depending on the fabrication technique and the material, thus providing a very wide range of properties that cannot be found in dense materials.

Polymers are often produced in a porous form for many applications, from thermal and acoustic insulation to packaging. Ceramics and to a lesser extent also metals (Bhattacharya et al., 2002) (Jee et al., 2000) find use in different fields. Porous ceramics are used when resistance to high temperature or to severely corrosive environments is required, such as in kiln insulation or filtration of molten metals (Brockmeyer and Aubrey, 1987). In other cases a specific functional property of the ceramic material is important along with its porous form, for example in the production of electrodes (Amini et al., 2011) or in bio-compatible implants.

In the following chapters, particularly mechanical properties (paragraph 1.1.2) and biological related properties (chapters 2 and 3) of porous ceramics will be discussed. A wider overview is however available in several excellent reviews and books (Scheffler and Colombo, 2006) (Rice, 1998).

##### **1.1.1 Fabrication of porous materials**

Several techniques have been employed to generate porous ceramics; since most of them are suitable to produce a total porosity and pore size in specific ranges, it seems useful to classify them accordingly.

In general, there are four main approaches (even though others exist) to produce porosity in ceramics (Stuart et al., 2006) (Ohji and Fukushima, 2012) (Colombo, 2006), according to *Table 1*.

	REPLICA	PARTIAL SINTERING	SACRIFICIAL TEMPLATES	DIRECT FOAMING
PORE SIZE	10 $\mu$ m to several mm	100nm to 1mm	1 $\mu$ m to 1mm	10 $\mu$ m to 1mm
POROSITY	20 to >90%	0 to 60%	20 to 90%	40 to 90%

**Table 1** Four main classes of technologies for the production of porous ceramics, and indicative ranges for porosity and pore size achievable.

**Partial sintering**, while it often used to be considered simply as the inability in obtaining full densification, is an effective and simple method to produce porous ceramics. The mean pore size is easily controllable since it is related to the particle size in the green body; typically pores are 2-5 times smaller than the particle size, depending on the degree of sintering (Ohji and Fukushima, 2012). Recent studies focused on the use of advanced techniques and materials to produce strong necks between the particles in the first stages of sintering, allowing the synthesis of high strength porous bodies (Jayaseelan et al., 2002). Addition of Yb<sub>2</sub>O<sub>3</sub> to  $\alpha$ -Si<sub>3</sub>N<sub>4</sub> as sintering additive permits to sinter the material achieving low densification and a transformation of equiaxed  $\alpha$ -Si<sub>3</sub>N<sub>4</sub> grains into  $\beta$ -Si<sub>3</sub>N<sub>4</sub> elongated grains, which increases the mechanical strength as well as the fracture toughness.

The downside of partial sintering is that the porosity is limited to the starting porosity of the green body, which means that porosities higher than 40-50% are not possible.

Replica techniques on the other side, as well as sacrificial templating and direct foaming all allow to reach porosities of 90% or more.

**Replica** consists in the impregnation of a synthetic or natural porous template with a liquid containing ceramic particles or a ceramic precursor; the following heat treatment burns out the template leaving a ceramic porous structure which is the replica of the template. Typically the process is performed by impregnating a polymeric foam (often polyurethane (Luyten et al., 2009)) with a ceramic slurry. More recently, the use of natural materials as template has attracted the interest of several researchers, for example using wood (Sieber et al., 2000) or coral (Roy and Linnehan, 1974). Wood can be heat treated in inert atmosphere to give a carbon template, which

can be infiltrated with liquid or gaseous metals, for example Si to form Si-SiC composites. The aragonite ( $\text{CaCO}_3$ ) phase in coral instead can be converted to hydroxyapatite ( $\text{Ca}_{10}(\text{PO}_4)_6(\text{OH})_2$ ) through a hydrothermal reaction.

The replica technique is suitable for obtaining open cellular ceramics with a pore size typically of  $1\mu\text{m}$  to 2 mm and porosities up to more than 90%. The drawback is that often the mechanical properties are limited by the presence of cracks and mainly by the formation of hollow struts after the decomposition of the template.

In the **sacrificial template** method a continuous matrix of ceramic particles or ceramic precursor contains a sacrificial material that is removed in a following step, leaving porosity in its place.

The geometrical result corresponds to a ceramic phase which is the negative of the sacrificial template, opposite to the replica method where the ceramic phase has a geometry which is a direct replication of the template.

Several sacrificial materials can be used, both organic or inorganic solids and liquids. Organic fillers such as PMMA (polymethylmethacrylate) spheres are mixed with the ceramic phase and subsequently removed by thermal decomposition. The use of hollow or expandable microspheres reduces the amount of gas released (Andersson and Bergström, 2008). The advantage of salts and other inorganic compounds is that they can be removed by immersing them in a suitable solvent, which often can conveniently be water. The use of non-mixable liquids to form emulsions is also attractive for the ability of forming very small and homogeneously distributed droplets of sacrificial material (Imhof and Pine, 1997).

The freeze-casting technique is extremely interesting for the possibility of producing highly anisotropic and aligned pores. In this case water (or less often oil) is used as sacrificial material. The liquid is frozen starting from a cooled plate on one side of the sample. Ice crystals grow unidirectionally perpendicular to the plate and after removing them by sublimation porous channels are left in the ceramic green body.

The sacrificial template method is highly reliable and flexible since the pore size and total porosity can be adjusted by the size and amount of template used (possible ranges are 20-90% porosity and  $1\mu\text{m}$  to 1mm size).

## **Direct foaming**

Direct foaming consists in incorporating air in a ceramic suspension (or ceramic precursor). The foam thus generated is instable and needs to be set and heat treated in order to achieve a sintered ceramic foam.

Air can be introduced in the liquid by many means, such as mechanical agitation, by bubbling compressed air, by additives which release gas etc. In any case however, the foam is not stable and tends to be quickly destabilized by mechanisms such as the Ostwald-ripening. In this way, the porous cells tend to gradually increase their size in order to decrease the total energy of the system, since a foam is thermodynamically instable.

A wet foam has to be stabilized for a sufficient time to complete a setting and drying process. The main two methods for achieving this stabilization are the addition of organic surfactants (Saggio-Woyansky et al., 1992), which help lowering the air-liquid surface energy, and a novel approach consisting in the addition of partially hydrophobic colloidal ceramic particles, that are absorbed at the air-liquid interface (Gonzenbach et al., 2007).

Direct foaming is versatile and allows a control over the amount of porosity (40% to 97%) and also the dimension of the cells (30  $\mu\text{m}$  to 1 mm with surfactants, 10-300  $\mu\text{m}$  with particles), even though the parameters to control are more difficult than for the replica or sacrificial template methods. Furthermore, it is also possible to obtain foams with either open or closed cells and the pore walls can be dense and crack-free, thus the foams often have high specific strength.

As mentioned, the previously cited methods allow some degree of control over the properties of the porous materials produced. However, they are all fundamentally driven by thermodynamic and kinetic processes which generate a distribution of cell dimensions and shape; while it is possible to modify the average properties of the foams and sometimes even their distribution, there is no ultimate control over the individual cells.

For this reason, additive manufacturing (AM) technologies attract great interest for the shaping of porous structures, since every single cell can be designed according to the desired properties.

Ultimately, the only limitations are the resolution of the technique used and the processing time. Most additive manufacturing processes have a resolution limited to about 100  $\mu\text{m}$ ; even when this

value is lower, there is a trade-off between resolution and processing time which limits the maximum dimension of the parts.

Besides this, the freedom in design that AM offers opens up new possibilities and applications in the field of porous materials and in particular porous ceramics. Ordered cellular structures are particularly interesting for lightweight materials, medical prosthesis, filtration, supports for catalysis and also at a smaller scale in fields such as photonics and piezoelectric materials. In all these cases, the design of the porosity improves the properties of the material for the specific applications and even more important it allows to tailor and predict the final outcome.

The application of additive manufacturing to lightweight materials will be discussed in the following sections. The use of AM in the medical field has been the subject of several reviews (for example see (Yeong et al., 2004) (Yang et al., 2002)).

An example of research on AM for filtration and piezoelectric materials can be found in (Galassi, 2006) while porous filters and catalyst supports produced by robocasting are already on the market (Robocasting Enterprises, <http://www.robocasting.net/>).

### **1.1.2 Elastic properties of porous materials**

Modelling and predicting the elastic properties of porous materials is an interesting problem both for theoretical and practical motivations, but it is far from having a trivial solution.

Different approaches have been used in literature and this chapter will review few of them. Nowadays porous parts can be simulated by finite elements simulation which can be fed with morphological information collected by means of 3D-scanning techniques (e.g. high resolution computer tomography) or by modelled structures. However, it is still very important to be able to establish explicit relationships between elastic properties and porosity and simulation can be helpful to validate these models rather than substituting them.

All methods described below make initial assumptions on a model geometry and derive equations based on a micromechanical analysis. A generic review of the main theories can be found in (Roberts and Garboczi, 2000) and (Ramakrishnan and Arunachalam, 1993).

NOTE: the following symbols will be used:

K = bulk modulus

G = shear modulus

E = Young modulus

$\nu$  = Poisson coefficient

$\rho$  = density

P = porosity

The subscript 0 will be used to indicate properties of the dense (zero-porosity) material.

$K/K_0$ ,  $G/G_0$ ,  $E/E_0$ ,  $\rho/\rho_0$ ,  $\nu/\nu_0$  will be referred to as “relative modulus, relative density etc.”

### **Self-consistent method (SCM) and differential methods (DM)**

These methods are based on a structure made of a continuous matrix containing a dilute porosity, which means containing homogeneously distributed spherical pores of infinitesimal size. This model has an exact analytical solution as:

$$\mathbf{K} = \mathbf{K}_0 \left( \mathbf{1} - \mathbf{P} \cdot \mathbf{K}_0 \cdot \frac{3\mathbf{K}_0 + 4\mathbf{G}_0}{4\mathbf{G}_0} \right)$$

*Eq. 1*

$$\mathbf{G} = \mathbf{G}_0 \cdot \left( \mathbf{1} - \mathbf{P} \cdot \mathbf{G}_0 \cdot \left( \frac{6\mathbf{K}_0 + 12\mathbf{G}_0}{9\mathbf{K}_0 + 8\mathbf{G}_0} + \mathbf{1} \right) \right)$$

*Eq. 2*

Given that  $G_0$  and  $K_0$  are constant for a selected matrix material, both equations give a linear dependence of the effective moduli on the porosity.

In order to extend this result to a finite porosity, several methods have been employed, the two most common being the self-consistent method (SCM) and the differential method (DM).

Hill and Budiansky developed a SCM at the same time in the '60s (Hill, 1965) (Budiansky, 1965).

The elasticity equations are imposed for a spherical inclusion in a matrix of unknown effective moduli after application of a constant stress or strain. The results give an expression for the



effective K and G moduli. The model was originally developed for a composite materials of N phases, but after simplifications for the case of a porous material the equations are in the form:

$$\frac{P}{1-\beta} + \frac{(1-P)}{1-\beta \left(\frac{G_0}{G}-1\right)} = 1$$

*Eq. 3*

$$\frac{P}{1-\alpha} + \frac{(1-P)}{1-\alpha \left(\frac{K_0}{K}-1\right)} = 1$$

*Eq. 4*

$$\alpha = \frac{1+\nu}{3(1-\nu)}; \beta = \frac{2(4-5\nu)}{15(1-\nu)}$$

These equations are coupled via the  $\alpha$  and  $\beta$  coefficients and cannot generally be solved independently.

This model provides a reasonable approximation for low porosities, but it should be carefully used for higher porosities, as the same Budiansky pointed out that the elastic moduli converge to zero at 50% porosity, which in general is clearly not what happens in natural and artificial materials.

Differential methods follow a similar approach, but they assume that a composite material has known effective moduli and they develop differential equations to take into account the effect of an infinitesimal increase in the secondary phase.

### **Minimum surface area models (MSA)**

This method is based on the hypothesis that the ratio of the effective moduli and the matrix moduli (which means the moduli of the dense material) is proportional to the minimum ratio of solid contact area to the total cross-sectional area (MSA) of the two phases.

In order to calculate the MSA a structure has to be assumed. A simple case is an array of solid spheres of radius R arranged in a cubic lattice of constant side L:

$$\frac{E}{E_0} = \frac{L^2 - \pi R^2}{L^2} = 1 - \pi \left(\frac{4}{3}\pi\right)^{-\frac{2}{3}} \cdot P^{\frac{2}{3}}$$

*Eq. 5*

Which is easily calculated considering that  $P = \frac{4}{3} \frac{\pi R^3}{L^3}$

This formula is valid for  $R < L/2$ , otherwise the spheres overlap and the areas are different.

This method gives a reasonable agreement with other theories and experimental results if a similar microstructure is assumed, at least in certain ranges of porosity (Roberts and Garboczi, 2000).

Noticeably, the relative elastic moduli are not linearly proportional to porosity, but they are related to it through a power law with an exponent which depends on the model chosen (2/3 in the example given in *Eq. 5*).

### **FEM simulations**

The advantage of FEM simulations is that specific information about the morphology of a porous material can be included in a model. (Roberts and Garboczi, 2000) simulated different structures and compared the simulated results to measured samples.

For example the dependence of the elastic modulus on the porosity could be described by:

$$\frac{E}{E_0} = \left(1 - \frac{P}{P_0}\right)^n$$

*Eq. 6*

This equation was used to interpolate simulation results, therefore their parameters  $n$  and  $P_0$  do not have a particular physical significance. Still, it is interesting that  $P_0 = 0.652$  and  $n = 2.23$  were used to interpolate the results for a random distribution of solid spheres, while  $P_0 = 0.818$  and  $n = 1.65$  for a random distribution of spherical pores. Also in this case, similarly to the MSA method, the relationship between relative elastic moduli and porosity can be expressed as a power law with an exponent which depends on the model used. The cases studied can also be related to the morphology of real foams: random overlapping spheres are an excellent model for a porous partially sintered ceramic, while a distribution of spherical pores is similar to the morphology of

closed-cell foams, produced for example by direct foaming. In this way, the model also assumes a predictive value even though its equations are not directly related to physical quantities.

### 1.1.3 Stretching-dominated vs bending-dominated porous structures

Another possible approach to relate the elastic properties of a porous material to its porosity is to model it as an array of struts arranged by regularly replicating a unit cell. By performing a mechanical analysis on a unit cell it is possible to extend the result to the porous structure.

Compared to the models described in paragraph 1.1.2 the present approach considers structural information, contrary to SCM and DM theories, while at the same time keeping a general significance and an explicit relationship to the physical parameters of the material, opposite to FEM simulations. Naturally, this theory fails to consider deviations from the model which are present in real porous materials, such as defects in the struts, cells of different size, or non-regularly distributed cells.

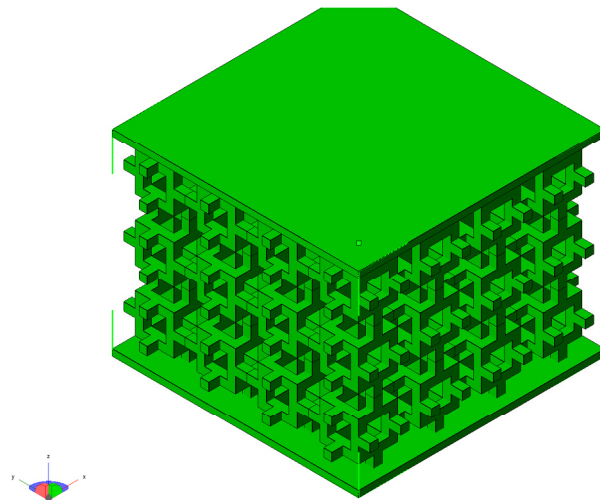


*Figure 1 Model of a Gibson-Ashby foam*

*Figure 1* shows a lattice structure which was used by Gibson and Ashby to model open-cell foams.

The unit cell is cubic and cells are connected to each other through struts in the middle of their sides. This configuration causes the struts to bend when a load is applied on the structure.

Supposing a stress  $\sigma$  applied to the top and bottom plates, every strut is loaded by a load  $F$  which is proportional to  $\sigma L^2$ , with  $L$  being the length of the side of a unit cell.

The strut deforms in bending and the total displacement  $D$  in the middle (see *Figure 2*) is calculated as:

$$D = \frac{FL^3}{E_0J}$$

**Eq. 7**

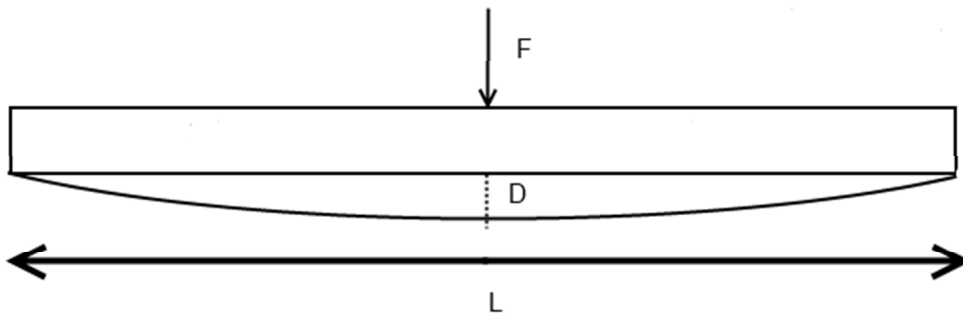


**Figure 2** Model of the bending of a strut

In this model structure,  $L$  is the length of the strut also and  $J$  is the second moment of its cross-sectional area. If the struts have a square cross-section of side  $t$ , then  $J = t^4/12$ .

The strain  $\varepsilon$  of a single cell is proportional to  $D/L$ , which means:

$$\varepsilon \propto \frac{\sigma L^4}{E_0 t^4}$$

**Eq. 8**

and given the relationship  $\sigma = E\varepsilon$ :

$$\frac{E}{E_0} \propto \left(\frac{t}{L}\right)^4$$

**Eq. 9**

From geometrical considerations it is easy to show that the relative density of the structure is proportional to  $(t/L)^2$ , therefore:

$$\frac{E}{E_0} \propto \left(\frac{\rho}{\rho_0}\right)^2$$

**Eq. 10**

Since it is expected that  $E = E_0$  when  $\rho = \rho_0$ , then the proportionality constant can be supposed to be close to 1.

Where  $\rho$  is the density of the porous material and  $\rho_0$  the density of the zero-porosity material, as usual. Therefore, the relative Young modulus is proportional to the square of the relative density.

It can also be noted that *Eq. 10* has the same form as *Eq. 6* when the coefficient  $n=2$ . It has been also mentioned that numerical simulations were well interpolated when  $n=2.23$  in the case of random overlapping spheres, and the two results are not very far apart, which is a confirmation of the effectiveness of the Gibson-Ashby model.

This kind of structure is called bending-dominated, because it deforms through bending of its struts. Every structure with a low connectivity between struts behaves similarly, but structures with a high connectivity have a different response to mechanical loading.

The Maxwell stability criterion states that a pin-joined frame is statically and kinetically determinate when:

$$M = b - 3j + 6 = 0$$

**Eq. 11**

$b$  = number of struts

$j$  = number of joints

If  $M < 0$  such as in *Figure 1*, the structure is a mechanism and the struts bend when they are loaded. If  $M = 0$  instead bending is ideally not possible and the struts can only deform either in tension or in compression.

$M > 0$  means that the frame is over-constrained and that it can be self-stressed, which means that struts can be under stress even when there is no applied external load. The Maxwell criterion can be extended to take into account states of self-stress and mechanisms, but this case will not be treated here.

A structure with  $M \geq 0$  is called stretch-dominated as opposite to bending-dominated. Since struts can deform only in tension or compression, it derives that the strain of the struts has to be linearly proportional to the external load and that the deformation of a cell is linearly proportional to that of the single struts. In mathematical terms:

$$\frac{E}{E_0} \propto \left( \frac{\rho}{\rho_0} \right)$$

*Eq. 12*

The exponent of the power-law is now 1, contrary to the value of 2 in Eq. 10. It is trivial to reach the conclusion that highly porous materials with a stretch-dominated architecture can be much stiffer than materials with a bending-dominated architecture (such as foams), because in the former case the elastic moduli decrease linearly as the porosity increases, while in the latter case this decrease is quadratic.

An example of a stretch-dominated structure is given in

*Figure 3.*

This part is similar to the one proposed by Ashby in (Deshpande et al., 2001) and (Ashby, 2006) and based on a unit cell which is an assembly of octahedra.

This model has  $m=14$  according to *Eq. 11*.

The complexity of these kind of structures requires novel production technologies and additive manufacturing seems especially suitable, since the complexity of design has a low impact on the feasibility and costs of the process.

It is worth mentioning that other approaches have been studied, such as an automated waving of metal wires (Lee et al., 2007).

Additive manufacturing on the other hand has been used both with direct approaches (for example selective laser sintering (Yan et al., 2012)) or indirect approaches, meaning that a sacrificial template has been produced and then used for investment casting (Wang et al., 2003).

The following chapter 1.2 describes one of the few attempts in literature to produce porous stretch-dominated parts made of a ceramic material. The method used consists in the 3D-printing of a preceramic polymer, which is also a novel process, followed by cross-linking and ceramization of the sample.

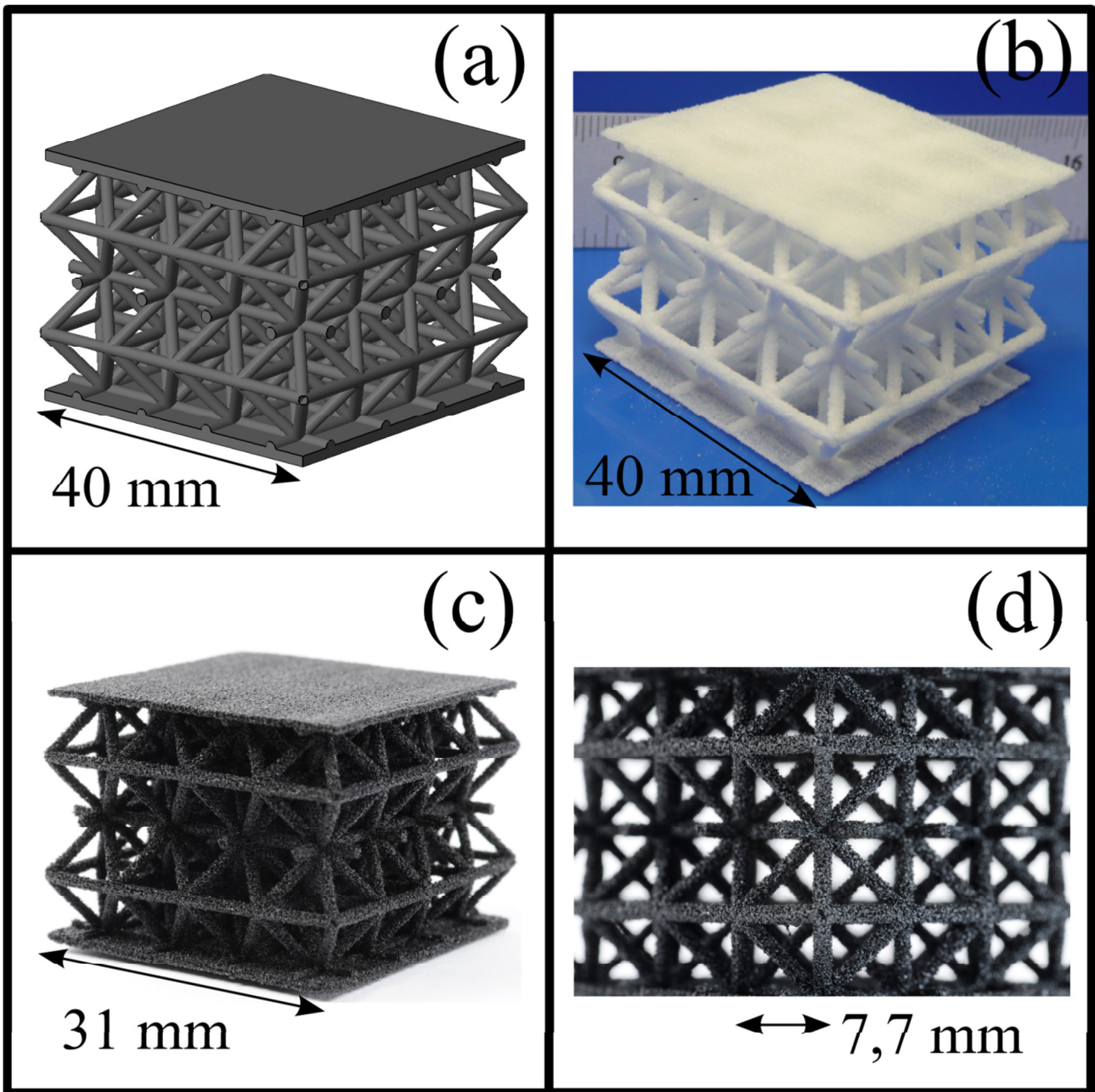


**Figure 3** Example of 3D-printed and ceramized stretch-dominated structure (a) CAD model (b) 3D-printed part in preceramic polymer (MK) (c) SiOC part ceramized at 1000°C (d) detail of the ceramized part.

## 1.2 Three-dimensional printing of preceramic polymers

### 1.2.1 Materials and methods

The powder-based 3D-printing process can be summed up with the following steps, represented by the diagram in *Figure 4*:

- 1) Drawing of a 3D (CAD) model representing the final sample to print
- 2) Slicing of the 3D object to create a stack of images each representing a cross-section of the part
- 3) Deposition of a layer of powder by means of a blade
- 4) A printing head locally inscribes in the layer the corresponding cross-section, by spreading out liquid droplets
- 5) Lowering of the platform by one layer thickness (typically, 100-200  $\mu\text{m}$ )
- 6) Repeating steps 3) – 5) until the height of the part is completed
- 7) Cleaning and extracting the part by removing the surrounding, non-printed, powder.

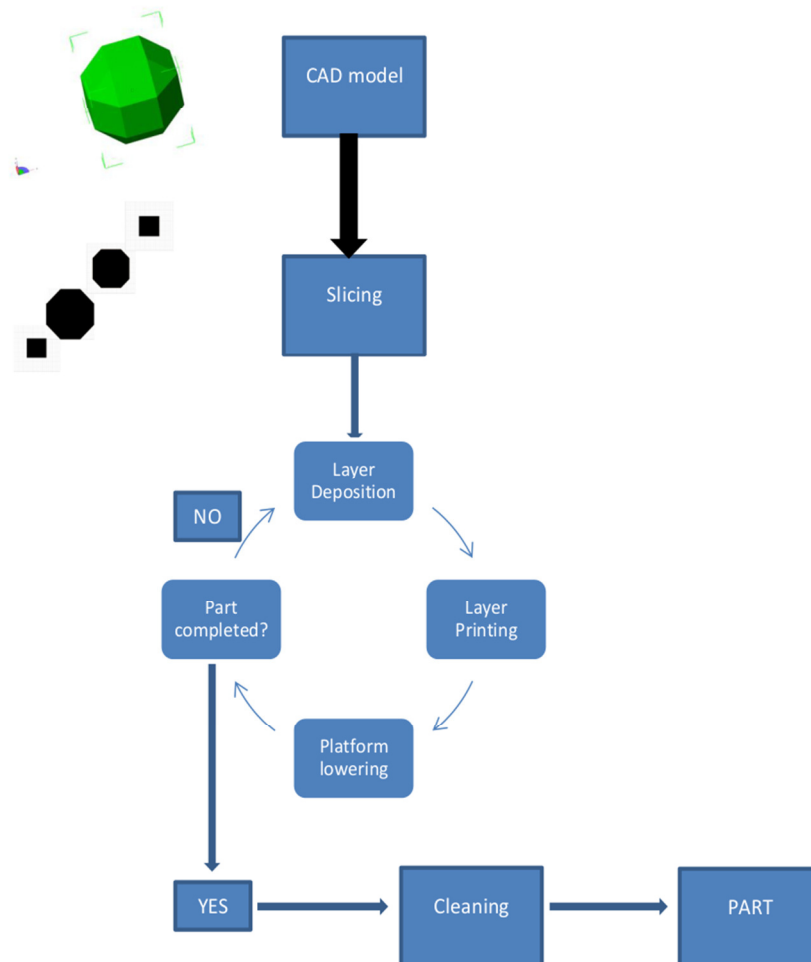


*Figure 4* Diagram of the powder based 3D-printing.



The printer used in this work was a Voxeljet Teststand VTS 16 (Voxeljet Technology GmbH, Germany) mounting a printing head with 128 jets (Spectra SL128-AA, Dimatix Fujifilm, USA) and using a blade recoating system. *Figure 5* shows the main components of this printer model.

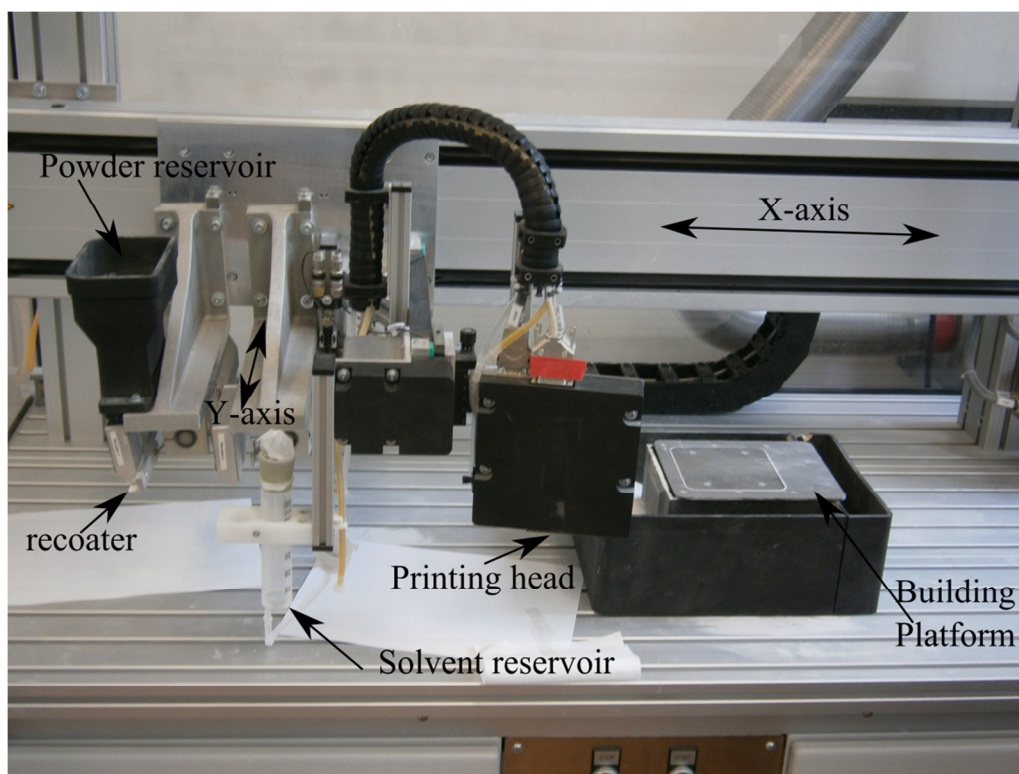


**Figure 5** Main parts composing the powder-based 3D-printer used in this work of thesis (Voxeljet Teststand VTS 16)

A commercial powder of a polymethylsilsesquioxane (PMS) preceramic polymer was used (Silres MK polymer, Wacker, Germany). This polymer was chosen because it is cheap, easily available and provided as a fine powder. The pure MK polymer has a softening temperature of 45-60°C, but it can be cross-linked by catalyzed polycondensation of hydroxyl and ethoxyl groups (which are present approximately in a 2 mol%) (Harshe, 2004).

Two different approaches were followed in order to introduce the cross-linking catalyst in the powder. In the first case, the PMS powder was dissolved in isopropanol (ApplChem, Germany) together with the catalyst zirconium acetylacetonate (ZrAcAc) (Sigma Aldrich, Germany) while stirring. The ratio used was  $\text{ZrAcAc} / \text{PMS} = 1 \text{ wt\%}$ .

The solution was dried under vacuum at moderate temperature and the clear solid obtained was ball milled and sieved in a range 45-90  $\mu\text{m}$ . This powder was 3D-printed using pure isopropanol as the printing liquid.

In the second approach, tin-octoate (TinOc) (Sigma Aldrich, Germany), which is a liquid, was mixed directly with the printing liquid. This strategy allowed us to introduce the catalyst directly during the printing job, avoiding the time consuming procedure of dissolving the polymer and the catalyst together, evaporating the solvent and then milling the mixture to obtain again a powder.

The TinOc could not be added to isopropanol, because it does not dissolve, forming a precipitate. A different solvent was therefore chosen, that is a mixture of 1-hexanol and hexylacetate (Voxeljet, Germany) (the mixture will be called “hexanol mixture” from here on), to which the liquid catalyst was added. After preliminary printing tests, a ratio of catalyst/ (catalyst + solvent) = 7.6 wt% was chosen. This mixture enabled the introduction in the printed powder of 0.9-1 wt% of catalyst. In this case, the pure as received PMS powder was sieved in order to remove the smaller and the bigger fractions, to respectively improve the flowability and make it fit for the layer by layer deposition. The main properties of the resulting powder are presented in *Table 2*.

	<b>D10</b>	<b>D50</b>	<b>D90</b>	<b>D97</b>	<b>Powder bulk density</b>	<b>Hausner Ratio<sup>a</sup></b>
	<b>(<math>\mu\text{m}</math>)</b>	<b>(<math>\mu\text{m}</math>)</b>	<b>(<math>\mu\text{m}</math>)</b>	<b>(<math>\mu\text{m}</math>)</b>	<b>(<math>\text{g}/\text{cm}^3</math>)</b>	
Preceramic powder	14	52	108	141	0.535	1.25

<sup>a</sup>HR <1.11: excellent flow; 1.12-1.18: good flow; 1.19-1.25: fair flow; 1.26-1.34: passable flow; 1.35-1.45: poor flow; 1.46-1.59: very poor flow; >1.60: no flow

**Table 2** Particle size distribution, bulk density and Hausner ratio of the PMS powder after sieving.

The flowability of the powder was evaluated by the Hausner ratio (H), measured according to *Eq. 13* (Hausner, 1981):

$$H = \frac{\rho_{\text{Tapped}}}{\rho_{\text{Bulk}}}$$

*Eq. 13*

where  $\rho_{\text{Bulk}}$  is the freely settled bulk density of the powder, and  $\rho_{\text{Tapped}}$  is the density of the tapped powder after a certain number of standardized tapping cycles.

The main parameter investigated for each printjob was the ratio (R) between the mass of solvent and the mass of powder in a printed part. Since a printed object can be considered to be a repetition of a single voxel (the three dimensional equivalent of a pixel) and that the printing head spits one drop of solvent for each voxel, R is then equivalent to the mass of a single drop divided by the mass of powder in one voxel, according to *Eq. 14*:

$$R = \frac{\text{drop mass}}{dx \cdot dy \cdot dz (\rho_{\text{Bulk}})}$$

***Eq. 14***

where  $dx \cdot dy$  is the lateral pixel area on the substrate where one droplet is spit and  $dz$  is the layer thickness; the value  $dx \cdot dy \cdot dz$  is therefore the volume of one voxel.

In order to ensure a precise control of the concentration of catalyst and solvent in the printed samples, the drop mass was measured prior to each printing job by measuring the mass of 30000 drops spit for each of the 128 jets and dividing the obtained value by the total amount of drops (30000 x 128); the measurement was repeated three times and averaged (0.01 g resolution). When necessary, the value of R was adjusted by modifying the value of  $dx$  [ $\mu\text{m}$ ], which is related to the printing head velocity ( $v$  [ $\mu\text{m/s}$ ]) and to the spitting frequency ( $f$  [Hz]) by *Eq. 15*:

$$dx = \frac{v}{f}$$

***Eq. 15***

The value of  $dy$  was fixed to 83  $\mu\text{m}$ , determined by the geometrical configuration of the printer, while  $dz$  (layer thickness) was chosen as 100  $\mu\text{m}$ , in a series of preliminary experiments conducted in order to optimize the spreading of the layers.

The mass ratio between catalyst and PMS powder in a printed part can be calculated from the following *Eq. 16*:

$$\frac{\text{catalyst}}{\text{PMS}} \text{wt}\% = \frac{\text{catalyst in 1 voxel}}{\text{powder in one voxel}} = \frac{\text{drop mass} \cdot 7.6/100}{dx \cdot dy \cdot dz (\rho_{\text{Bulk}})} = R \cdot 7.6/100$$

***Eq. 16***

The printed parts were left immersed in the support powder bed overnight to evaporate the excess solvent, and were finally cleaned by means of a brush and a compressed air gun.

The green parts were cross-linked by slowly (30°C/h) heating them up to 100°C or 150°C (100°C where not differently stated) in a muffle furnace in air, and were then ceramized by heating at 1000°C or 1200°C in nitrogen atmosphere with a heating ramp of 1°C/min and a dwell time of 1 h at the maximum temperature.

The skeleton density was measured with a helium pycnometer (Accupyc 1330, Micrometric Instrument Corporation, USA), while the bulk density and porosity of the printed parts were obtained by the Archimede's method measuring the dry, saturated and suspended mass in water. For the characterization of samples printed with isopropanol, four tablets of 16 mm diameter and 3 mm thickness (green dimensions) were produced. The samples printed with the hexanol mixture were instead cubes of 12x12x12 mm<sup>3</sup>. Each sample was measured three times, before and after pyrolysis. The Kagome lattices were drawn with a commercial CAD software (Solid Edge ST3, Siemens PLM Software, Germany). Ten prismatic samples of base 4x10 mm<sup>2</sup> and height 10 mm (geometry according to ISO 604 for polymeric materials) were printed and tested under compression (Z005, Zwick/Roell, Ulf, Germany; cross-head speed of 0.5 mm/min), to evaluate the compressive strength of the green parts. The same procedure was repeated for 10 samples after cross-linking at 150°C.

The ceramized material was investigated by means of XRD (X-Ray Diffractometer, PW 1710-Basis, Panalytical GmbH, Germany). One of the produced Kagome structures was scanned by micro-CT and analyzed both in the green and in the ceramic state. Measurements were performed on the BAM 225kV-microCT-device. This device features an X-RAY WorX micro-focus X-ray tube with 225kV acceleration voltage and a focal spot size of approximately 10 μm. The detector was a flat-panel (PerkinElmer) with 2048x2048 pixels at a pitch of 0.2 mm.

The morphology of the printed parts was investigated using an optical microscope (VHX-100 digital microscope, Keyence corporation, Japan) and scanning electron microscopy (SEM; JEOL JSM-6490, Jeol Italia, Italy).

## **1.2.2 Results and discussion**

### **1.2.2.1 Influence of the printing parameters**

The concentration of printing liquid spit in a layer is the most important parameter to consider, and it can be evaluated by the parameter  $R$  introduced in *Eq. 14*.

A preliminary test allowed the definition of a maximum value of  $R$ , above which a layer doesn't remain flat and therefore a new layer cannot be deposited. When a higher amount of material is

introduced, it tends to warp due to stresses introduced by the gradient in solvent concentration, which is mainly generated because the evaporation rate is higher from the top of the layer than from the bottom. This maximum possible amount for the hexanol mixture used as the printing liquid was determined to be as  $R = 15.2\%$  in a series of preliminary experiments.

The influence of  $R$  on the morphology of three dimensional samples was afterwards studied in a wide range between  $7.6\%$  and  $13.5\%$ , as shown in

*Figure 6.*

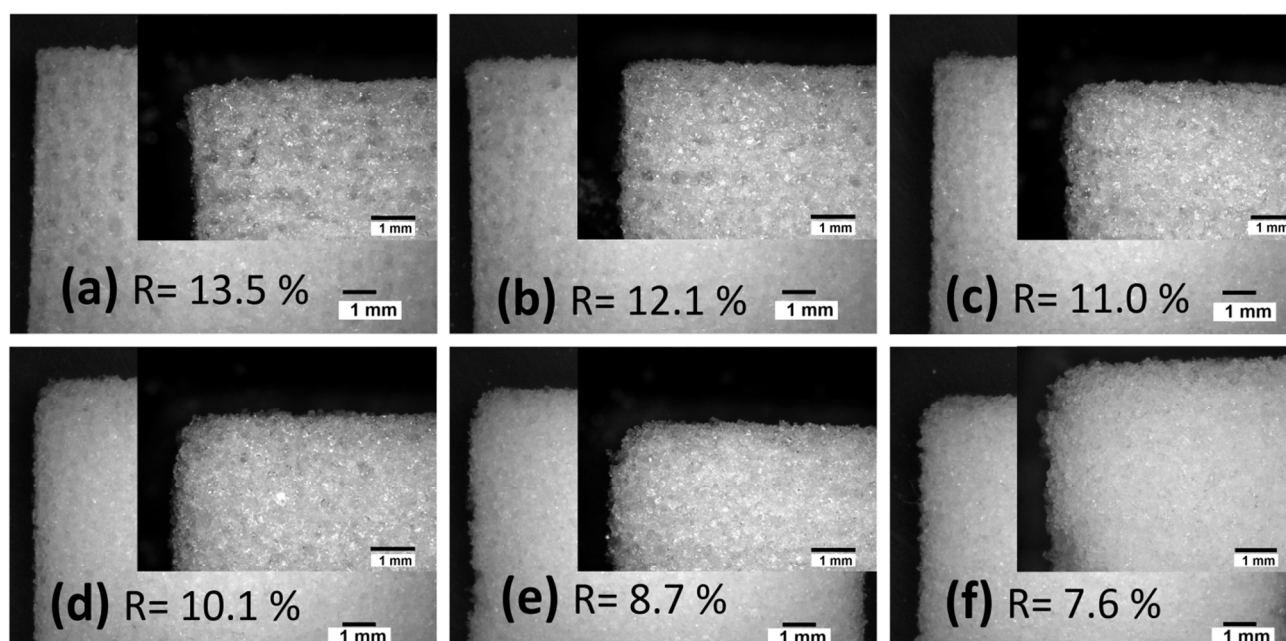


**Figure 6** Optical microscope micrographs showing the morphology of square-section samples printed using different  $R$  values ( $R = \text{solvent/powder mass ratio}$ ; solvent: hexanol mixture). For clarity, each part of the figure shows two micrographs of the same sample at a different magnification: the micrograph in the background represents an overview of the morphology of the part; the micrograph superimposed on the top-right corner is a detail of the corner of the part. Solvent concentration increases from bottom to top and from right to left: (a)  $R = 13.5\%$ ; (b)  $R = 12.1\%$ ; (c)  $R = 11.0\%$ ; (d)  $R = 10.1\%$ ; (e)  $R = 8.7\%$ ; (f)  $R = 7.6\%$

It can be noted how the squares printed with  $R = 7.6\%$  and  $R = 8.7\%$  have round corners and were damaged during cleaning, so these parameters are not useful to produce geometrically precise components. On the opposite side, a value of  $R = 13.5\%$  generated sharp corners and sharp sides, but some shape distortion was present due to the high amount of solvent. This value may however be considered suitable for printing very fine structures, where it is desired to maximize the

mechanical strength of the produced part. Values of  $R= 11.0 \%$  and  $R= 12.1 \%$  can be considered to be optimal, as they enabled to produce samples possessing sharp corners and well defined sides. A slightly lower value  $R= 10.1 \%$  might lead to sharp sides but smoothed corners after cleaning, so it could be considered optimal for printing large parts, where it is preferred to save some solvent and prevent macroscopic distortions.

As discussed before, when the catalyst is mixed with the printing liquid, its concentration is related to  $R$  by *Eq. 16*. A value of  $R= 12.1 \%$  (used for the printed 3D-parts) corresponds to a catalyst concentration of 0.92 wt%, while  $R= 13.5 \%$  corresponds to 1.0 wt%.

Similar studies were performed with isopropanol used as a printing liquid, but in this case distortion of the parts occurs at lower  $R$  values. A value of  $R= 6.0 \%$  was used to print the samples described in section B.

### 1.2.2.2 Optimization of printing and ceramization conditions

In order to investigate the effect of different printing parameters and to optimize them, bulk samples with simple geometry (tablets, T-samples, or cubes, C-samples) were firstly produced. The compressive strength of as printed prism samples was  $3 \pm 1$  MPa, which allowed cleaning and handling the parts easily. The rather high strength of the green samples can be attributed to the printing of a pure preceramic polymer, without the need of an additional binder.

Completion of the cross-linking process at  $150^\circ\text{C}$  led to an increased compressive strength of  $20 \pm 2$  MPa and a brittle behavior, typical of thermo-setting resins.

The main processing parameters and the density and porosity of the green samples are reported in *Table 3*, while characterization data for the ceramized samples are summarized in *Table 4*.

Sample	Printing Liquid	Catalyst	Catalyst added to:	Green Density ( $\text{g/cm}^3$ )	Green Porosity (%)
CT1000	1-hexanol + hexylacetate	TinOc	printing liquid	$0.97 \pm 0.05$	$19 \pm 4$
CT1200	1-hexanol + hexylacetate	TinOc	printing liquid	$0.96 \pm 0.04$	$20 \pm 3$
TZ1200	Isopropanol	ZrAcAc	powder	$0.59 \pm 0.01$	$51 \pm 1$

**Table 3** Printing conditions, green density and green porosity of the different printed samples.

Sample	Mass Loss (%)	Shrinkage X (%)	Shrinkage Y (%)	Shrinkage Z (%)	Ceramic density (g/cm <sup>3</sup> )	Open porosity (%)	Total porosity (%)
CT1000	16 ± 1	19 ± 1	19 ± 1	18.8 ± 0.6	1.67 ± 0.05	13 ± 2	24 ± 3
CT1200	16.5 ± 0.7	22 ± 1	22 ± 1	22.2 ± 0.6	1.84 ± 0.05	11 ± 2	19 ± 2
TZ1200	16 ± 1	32.0 ± 0.2	32.0 ± 0.2	n.d.	1.97 ± 0.01	12.4 ± 0.5	12.9 ± 0.5

**Table 4** Ceramization mass loss, ceramization shrinkage, ceramic density and porosity of the ceramized samples

The mass loss during the polymer to ceramic transformation is reduced by the addition of a catalyst (Harshe, 2004) and it was approximately 16 % for all samples (at 1200 °C, measured by weighting the samples before and after pyrolysis; the same samples used for density measurements were used), indicating that the use of different catalysts or of different methods to introduce them (in the powder or in the printing liquid) did not have a relevant effect on this parameter. The density of the parts printed with the hexanol mixture was quite high (80 % ca.) and considering a low density of the powder bed (45 %, taking into account a density of 1.2 g/cm<sup>3</sup> for the dense polymer) this indicates that a considerable densification occurred due to the surface dissolution of the polymeric particles.

The parts printed with isopropanol (TZ1200) had a much lower green density (49 %), which was due both to a lower concentration of solvent in the part and to its much higher vapor pressure (4.3 kPa for isopropanol and 0.12 kPa for the hexanol mixture, at 20°C).

Wu and Cima (Wu and Cima, 1999) described the solvent-particle interaction during three-dimensional printing, correlating the microstructure formation with the timescales for dissolution and evaporation.

In our case, the use of a solvent with high vapor pressure implies a short evaporation time and a much limited timescale for dissolution, creating a highly porous printed part.

During heat treatment in inert atmosphere, the preceramic first cross-links, with a loss of water, ethanol and methanol caused by polycondensation, then at temperatures between 400 and 800°C the polymer to ceramic transformation completes with further release of hydrogen and methane. The final result of the ceramization process of a pure polysiloxane polymer in inert atmosphere is a black amorphous material of general composition Si<sub>x</sub>O<sub>y</sub>C<sub>z</sub> (Colombo et al., 2010) (Harshe, 2004).

All the samples heat treated at 1000 – 1200°C in N<sub>2</sub> atmosphere were black and the amorphous nature was confirmed by XRD analysis, not reported here for the sake of brevity.

The porosity in the ceramized parts was lower for samples TZ1200 (ZrAcAc added as catalyst) than for samples CT1200 (TinOc as catalyst). In the latter case, the negligible reduction of porosity from the green bodies to the ceramic bodies indicates that viscous flow during pyrolysis was almost negligible, both in the polymeric stage (because of the action of the catalyst) and in the ceramic stage (because the glass transition temperature of amorphous SiOC is > 1400°C). In the case of samples TZ1200, instead, the higher densification (approx. 87% relative density) could be explained with a lower crosslinking efficiency of the ZrAcAc, resulting in some degree of viscous flow during heating from the polymeric state. The ceramization of samples TZ1200 occurred with a very large axial linear shrinkage of 32 %. Despite of the large value, no evident shape distortion was observed, at least for these parts with a simple geometry. A comparison between samples heated at 1000°C (CT1000) and 1200°C (CT1200), see *Table 4*, shows an increase in density from 1.67 g/cm<sup>3</sup> to 1.84 g/cm<sup>3</sup> and in shrinkage from 19 % to 22 % with increasing temperature.

The difference in linear shrinkage between samples TZ1200 and CT1200 (32 % and 22 % respectively) can be related to the much lower green density of the TZ1200 samples compared to the CT1200 samples (0.59 g/cm<sup>3</sup> and 0.96 g/cm<sup>3</sup> respectively).

Shrinkage was isotropic in all the samples, and this factor contributes to the possibility of producing undistorted parts.

The residual porosity present in the samples was due to limited viscous flow of the preceramic particles during pyrolysis. This characteristic depends on a complex interplay between various factors, such as the heating rate, the amount and type of catalyst introduced, the molecular weight distribution of the preceramic polymer (which can change with the time of storage), and the particle packing after printing. In any case, the open porosity in the green samples, which was partially retained in the ceramized parts after heating to high temperature, allowed the release of decomposition gases with no obvious cracking or distortion even for thick components (up to 5 mm), this being usually instead a major issue in the conversion of pure dense preceramic polymer bodies. Severe cracking was observed only in a cube sample with a thickness larger than 10 mm.

Both strategies to introduce the catalyst in the polymer were successful for the printing and ceramization steps.

A few samples were printed and converted using the strategy of mixing the catalyst ZrAcAc in the preceramic powder. Despite the promising results, for printing of larger three dimensional structures the preparation of the powder was inconveniently time consuming, so only the route with the catalyst in the printing liquid was then followed.



### 1.2.2.3 Printing of ordered porous structures

In *Figure 7* are reported images of the Kagome lattice, comparing the three dimensional STL-object and the printed part (before and after ceramization). The complete CAD structure (*Figure 7a*) had dimensions 40 mm x 40 mm x 30 mm, a porosity of 79.9 % including top and bottom plates and a strut thickness of 1.5 mm. *Figure 7* shows that the porous Kagome could be successfully printed, preserving the features of the fine structure both in the polymeric (*Figure 7b*, *Figure 7c*) and in the ceramic state (*Figure 7d*, after ceramization at 1200°C).

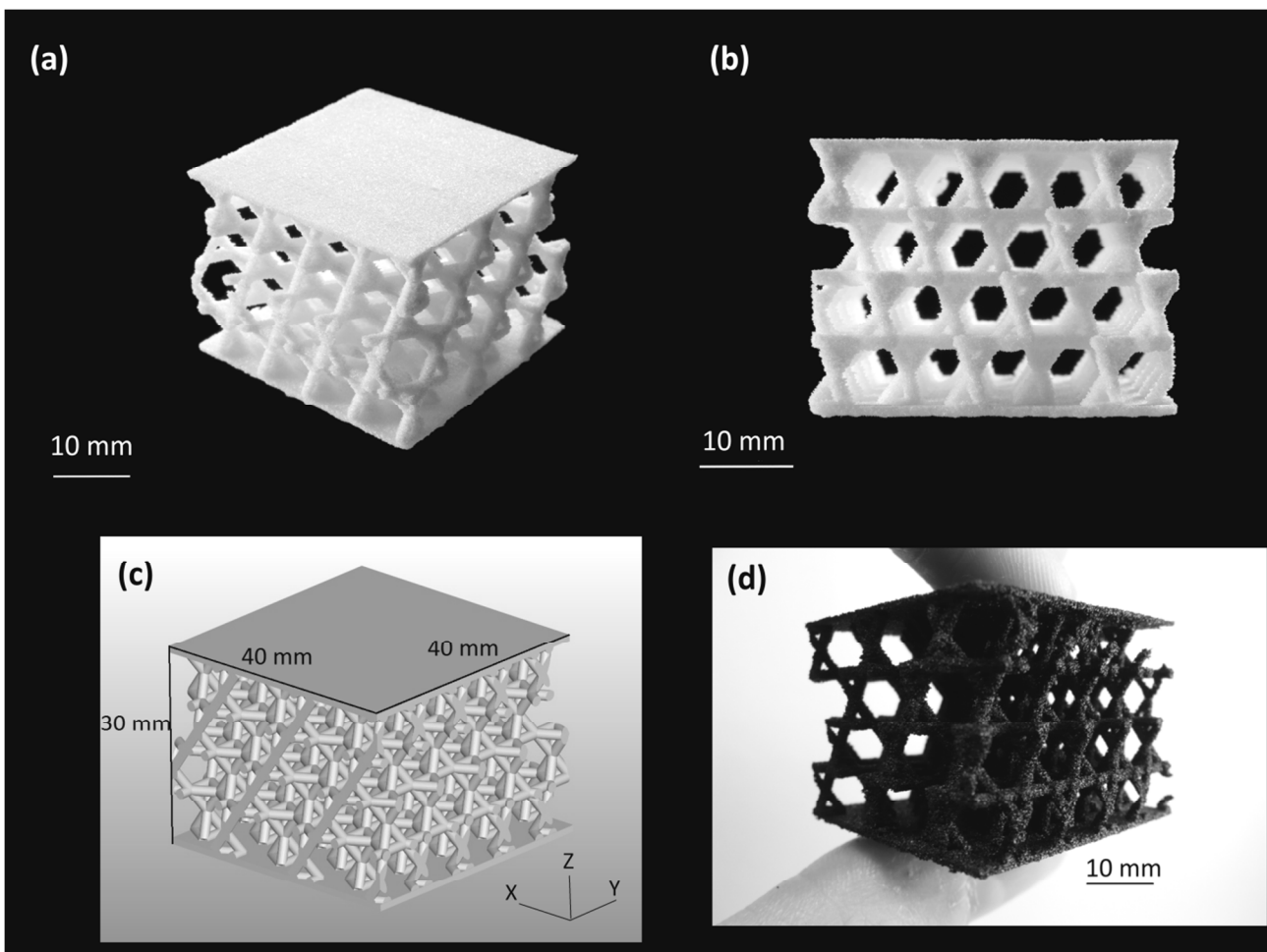


**Figure 7** (a) CAD-model of the Kagome structure; (b) lateral view of the polymeric printed Kagome structure; (c) front view of the polymeric printed Kagome structure; (d) SiOC ceramic structure ceramized at 1200°C.

Single struts from the structure were investigated by means of SEM analysis at the different stages of the process (after printing, after cross-linking, after ceramization), and the relative micrographs are presented in *Figure 8*.

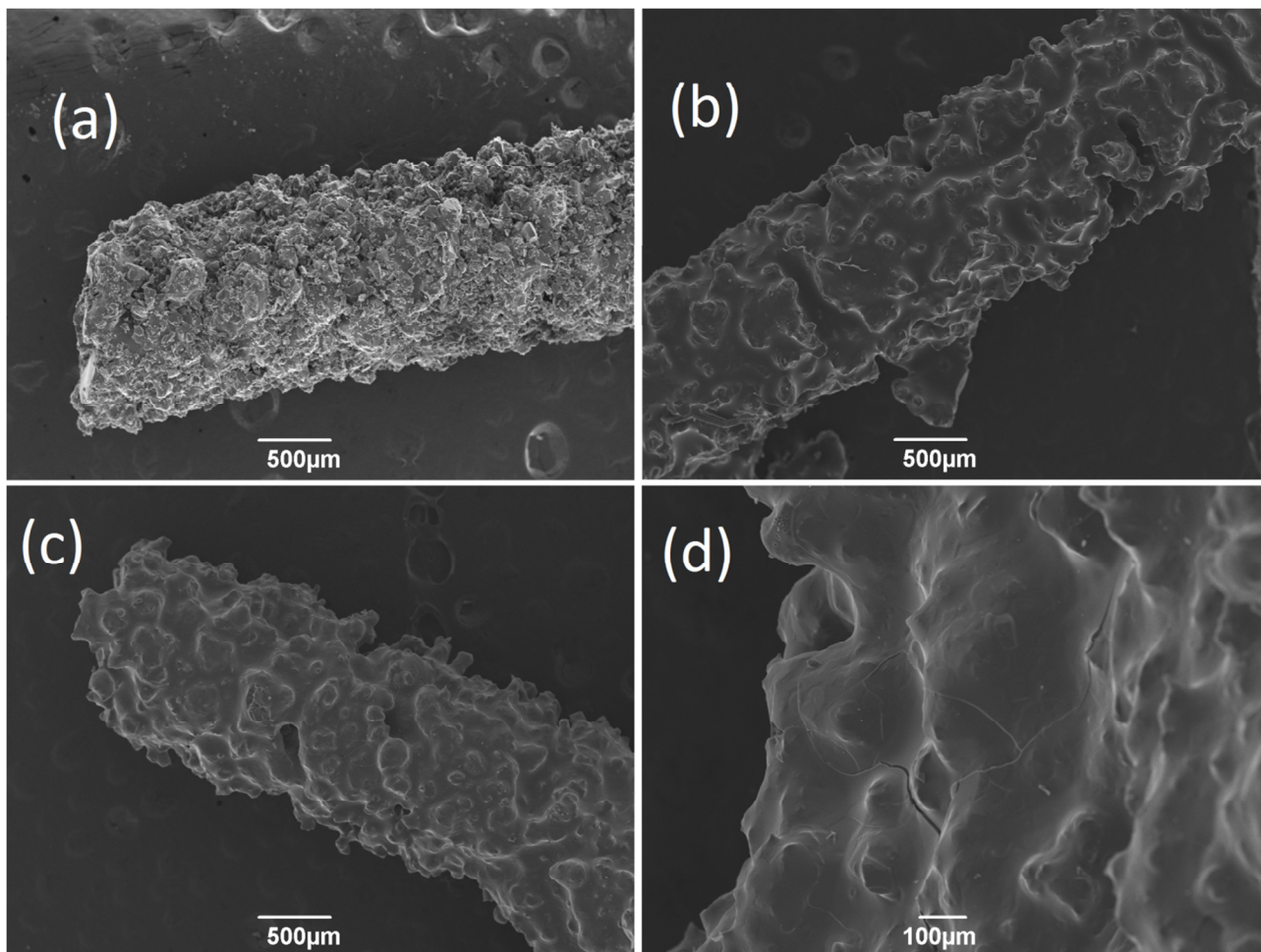


**Figure 8** SEM micrographs of the struts of the Kagome structure: (a) polymeric (as printed); (b) polymeric (after cross-linking at 150°C); (c) ceramized at 1200°C; (d) detail of a ceramized strut, showing the presence of some cracks.

The struts just after printing (*Figure 8a*) are very rough, because the surface is covered with particles, coming from the powder bed, that adhere either electrostatically or because they are only partially dissolved. After cross-linking (*Figure 8b*), the strut appears much smoother, because during heating to the cross-linking temperature melting of the preceramic polymer particles occurs. When the catalyst is introduced through the printing solvent, the particles that are not directly beneath the printed area do not contain any catalyst, so they simply melt during heating.

The surface of the struts is still very irregular, and this can be attributed to the limited resolution of the printer in replicating thin structures (1.5 mm diameter). Strategies to optimize the shape and the surface of the struts, for instance by tailoring the rheological properties of the preceramic polymer through the amount and type of catalyst added, are currently under evaluation.

After ceramization (*Figure 8c*) the morphology is basically unchanged in comparison with the cross-linked structure. In this case, however, the formation of some surface cracks with a length of few hundreds of micrometers could be noted (*Figure 8d*). These cracks were not present in the cross-linked structures, and therefore they developed during the ceramization process, because the release of gases and the high shrinkage associated with the polymer-to-ceramic transformation (Colombo et al., 2010).

In order to evaluate the precision of the geometrical replication of the CAD file by printing of the preceramic polymer, a sample of the Kagome structure was scanned by micro-CT after printing and after ceramization, and the corresponding three-dimensional model was reconstructed. All data obtained from the micro-CT scans are collected in Table IV. The acceleration voltage during measurement was 80 keV, no pre-filter was used. The volume was reconstructed using the standard FDK filtered back-projection algorithm with a resulting voxel size of 31  $\mu\text{m}$ .

For the comparison of the original STL file obtained from CAD drawings with the reconstructed CT volume, the data were analyzed with VGStudio Max 2.1 (VolumeGraphics, Germany). The object surface was determined as the Iso50-surface between air and the lowest material peak in the gray-value histogram. Then a scale correction was applied to fit the dimensions of the CT-model to the exact dimensions of the STL-object.

From the determined scale factors, it could be evinced that the printed part was smaller by a factor 0.996 in the x-y and 0.978 in z direction (height). Since the x (or y) dimension of the STL part is 40 mm, a factor of 0.996 corresponds to an actual size of 39.8 mm, which means that the difference is within the minimum resolution range of the printer. The typical dimension of a printed pixel in x-y is 0.1 mm x 0.1 mm, so a difference of 0.2 mm corresponds to only two pixels.

The scale factor along z was instead equal to 0.978 for a dimension of 30 mm, which corresponds to an actual dimension of 29.3 mm. This 0.7 mm difference could be explained by the partial removal of the support structure at the bottom of the printed part, or to some little distortion due to gravity, because the part was cleaned when the solvent had not yet completely evaporated.

After scale correction, the CT-model was registered on the STL-object to calculate the deviation of the CT-model surface to the STL-object surface. The result is shown in *Figure 9*, where the deviation varies from -0.5 mm (blue color) to +0.5 mm (red color) and the points with an absolute deviation lower than 0.1 mm are in green. Note that the color scale should be interpreted using the

same scale corrections used for the dimensional comparison, but for qualitative considerations this is not relevant.

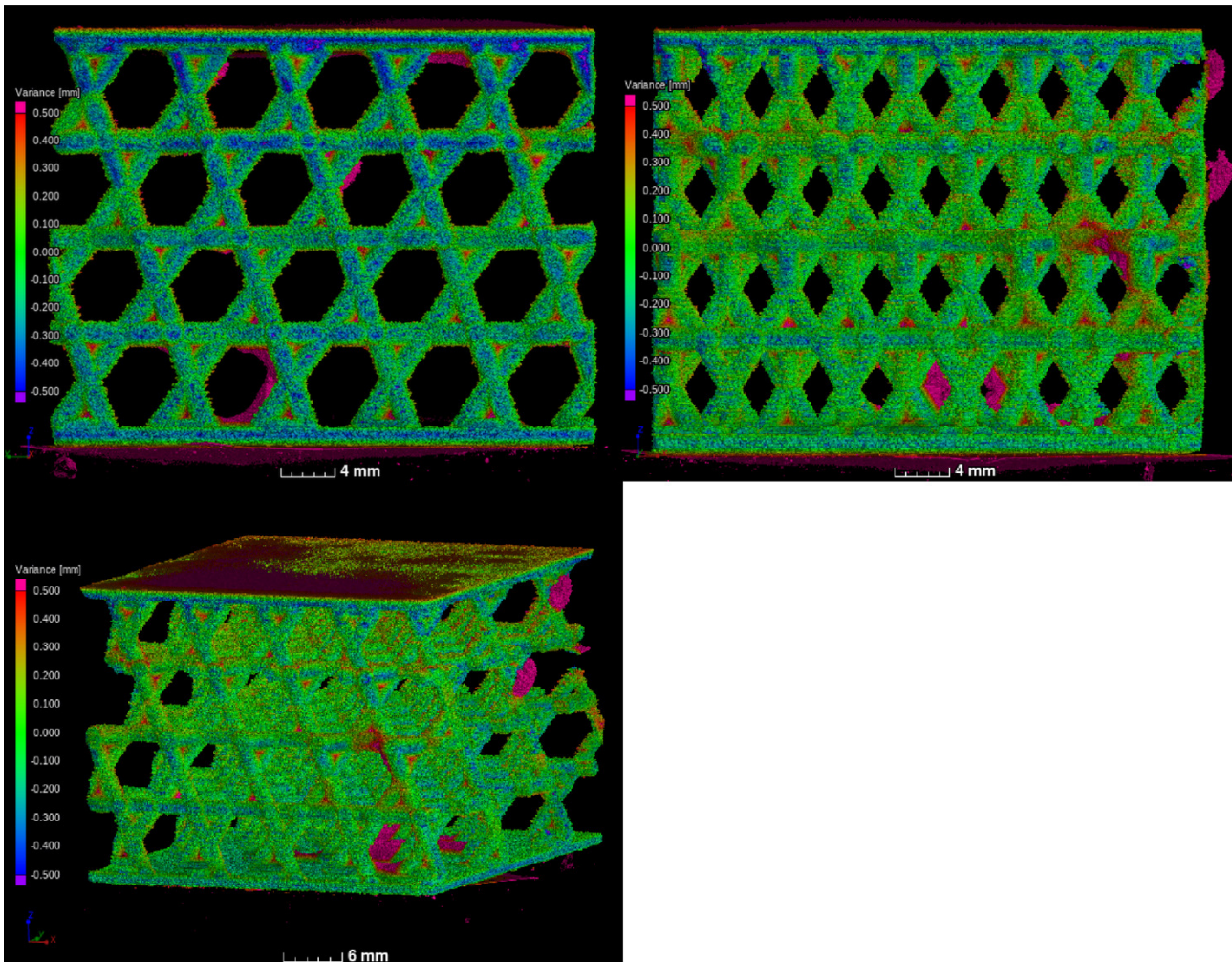


**Figure 9** Screen shots of the three comparisons between the CT-scanned “as printed” part (before cross-linking and ceramization) and the STL-object used as the printing model. Colors represent the point-by-point variance between the two volumes, ranging from -0.5 mm variance (blue) to +0.5 mm (red). a) front view; b) bottom view; c) lateral view.

Most part of the surface of the structure is colored green, which means that it was printed with a precision close to the resolution of the printer (concerning the voxel size). Blue deviations appear in particular along the x-direction of the structure, meaning that some material is missing compared to the STL-object, or that the object is slightly distorted. This is most likely due to a too aggressive cleaning of the part that removed also some material from the struts. There are also some areas

colored red (excess material) inside the structure close to the top and bottom plates, meaning that the non-printed powder was not perfectly cleaned. Some areas colored red can be also noted inside the octahedral cells, because the cells were too small to completely remove the loose powder trapped inside. Finally, two partially broken struts can be noted on the top right side of *Figure 9c*, protruding out of the structure. These are a result of the cleaning procedure.

The total porosity of the CT-model was also calculated using VGStudio Max 2.1. The volume occupied by printed material in the Kagome lattice was calculated after surface determination following the same procedure previously described. The total volume occupied by the structure was determined as the volume of the smallest prism that completely encloses the object (including top and bottom plates). A value of 83 vol% of total porosity was obtained for the complete part. This value can't be directly compared to the total porosity of the STL-object (80 vol% ca.), because the porosity in the struts should be also considered.

A reasonably approximate value can then be calculated supposing that the green struts have the same porosity of the bulk green parts, which is 20 % (see *Table 3*).

The “expected theoretical” total porosity can then be estimated according to *Eq. 17*:

$$\text{Expected porosity} = P(\text{STL}) + (100 - P(\text{STL})) \cdot P(\text{struts}) = (100 - 80) \cdot 0.2 = 84\%$$

*Eq. 17*

where  $P(\text{STL})$  is the % porosity of the STL-object and  $P(\text{struts})$  the porosity of the green struts. The value obtained is very close to the one measured for the printed part, so we can conclude that the total porosity of the model could be very precisely replicated by the printing procedure.

Micro-CT was also used to scan the Kagome structure after ceramization, using the data to measure precisely the shrinkage. The analysis steps applied to the CT-data were the same as described before. The CT measurement parameters were identical to those for the object "as printed", apart from the voxel size of the reconstructed data, which was 24  $\mu\text{m}$ .

The shrinkage measured in the x-y direction was 22.8 %, very similar to the value obtained for the bulk parts (see *Table 5*). The shrinkage measured in the z direction was instead higher, 27.4 %. This is most probably due to the effect of gravity during cross-linking, in a range of temperatures between 50 and 100°C when the structure is not cross-linked enough to be completely stabilized.

Dimensions relative to STL-object		Ceramization shrinkage (%)		Expected Porosity (%)	Actual Porosity (%)
X-Y	Z	X-Y	Z		
0.996	0.978	22.8	27.4	84	83

**Table 5** Dimensions relative to the STL-object, ceramization shrinkage, expected porosity (STL-object) and actual porosity of a printed Kagome structure. Data are obtained from micro-CT scan and analysis of the model of the part before and after pyrolysis.

It was noted that some of the complex printed parts that contained some defects (such as damaged struts) on one side tended to bend on that side during heat treatment. The problem was solved by decreasing the cross-linking heating rate from 30°C/h to 1.5°C/h (up to 100°C). This proves that the catalyst is active enough to sufficiently stabilize the structure even at low temperatures; the precise role of the amount of catalyst and of the heating rate on the strut density and shape retention of the Kagome structure will be the subject of further investigations. In future works, we will also extend this approach to include powders based on a mixture of a preceramic polymer with ceramic or metallic powder fillers, in order to greatly extend the range of compositions and properties achievable (Colombo et al., 2013).

### 1.2.3 Conclusions

Powder-based 3D-printing of a preceramic polymer has been for the first time here reported. Two different printing liquids were employed, depending on the strategy adopted for introducing the cross-linking catalyst (mixing with the preceramic polymer powder or with the printing liquid solvent). Both routes proved successful, but adding the catalyst directly to the printing liquid is the most convenient way of applying 3D-printing to a pure preceramic powder, because it greatly simplifies the process. On the other hand, with this approach the concentration of the catalyst within the powder depends on the amount of printing liquid used. Thus, a careful investigation of the printing parameters prior to the addition of the catalyst to the printing liquid is required.

Furthermore, it is important to densify the structure during printing, because a significant viscous flow prior to the thermally activated cross-linking would distort the parts. This limits the possibility of achieving a further densification by viscous flow during the heat treatment. In order to improve the densification during printing, the use of a hexanol mixture as printing liquid is to be preferred to isopropanol. In addition, the use of tin-octoate as a catalyst was proved to be suitable to stabilize the parts even at low temperatures, when added to the powder with a concentration of 1 wt%.

Residual porosity in the printed parts was present after cross-linking and ceramization, due to the limited viscous flow of the polymer during heating, controlled by the processing parameters.

Complex ceramic parts possessing an ordered, designed porosity according to the corresponding three-dimensional model were successfully produced. Micro-CT analysis of the printed components demonstrated that the local features, overall structure and total porosity could be very well replicated with respect to the starting CAD model, because of the precision of the printing procedure and the optimization of the processing conditions.

## References

- Amini, N., Aguey-Zinsou, K.-F., Guo, Z.-X., 2011. Processing of strong and highly conductive carbon foams as electrode. *Carbon* 49, 3857–3864. doi:10.1016/j.carbon.2011.05.022
- Andersson, L., Bergström, L., 2008. Gas-filled microspheres as an expandable sacrificial template for direct casting of complex-shaped macroporous ceramics. *J. Eur. Ceram. Soc.* 28, 2815–2821. doi:10.1016/j.jeurceramsoc.2008.04.020
- Ashby, M.F., 2006. The properties of foams and lattices. *Philos. Trans. R. Soc. Math. Phys. Eng. Sci.* 364, 15–30. doi:10.1098/rsta.2005.1678
- Bhattacharya, A., Calmidi, V.V., Mahajan, R.L., 2002. Thermophysical properties of high porosity metal foams. *Int. J. Heat Mass Transf.* 45, 1017–1031.
- Brockmeyer, J.W., Aubrey, L.S., 1987. Application of Ceramic Foam Filters in Molten Metal Filtration, in: Smothers, W.J. (Ed.), *Application of Refractories: Ceramic Engineering and Science Proceedings*. John Wiley & Sons, Inc., pp. 63–74.
- Budiansky, B., 1965. On the elastic moduli of some heterogeneous materials. *J. Mech. Phys. Solids* 13, 223–227. doi:10.1016/0022-5096(65)90011-6
- Colombo, P., 2006. Conventional and novel processing methods for cellular ceramics. *Philos. Trans. R. Soc. Math. Phys. Eng. Sci.* 364, 109–124. doi:10.1098/rsta.2005.1683
- Colombo, P., 2008. In Praise of Pores. *Science* 322, 381–383. doi:10.1126/science.1162962
- Colombo, P., Bernardo, E., Parcianello, G., 2013. Multifunctional advanced ceramics from preceramic polymers and nano-sized active fillers. *J. Eur. Ceram. Soc.* 33, 453–469. doi:10.1016/j.jeurceramsoc.2012.10.006
- Colombo, P., Mera, G., Riedel, R., Sorarù, G.D., 2010. Polymer-Derived Ceramics: 40 Years of Research and Innovation in Advanced Ceramics. *J. Am. Ceram. Soc.* 93, 1805–1837. doi:10.1111/j.1551-2916.2010.03876.x
- Cooper, D.M.L., Matyas, J.R., Katzenberg, M.A., Hallgrímsson, B., 2004. Comparison of microcomputed tomographic and microradiographic measurements of cortical bone porosity. *Calcif. Tissue Int.* 74, 437–447.
- Deshpande, V.S., Fleck, N.A., Ashby, M.F., 2001. Effective properties of the octet-truss lattice material. *J. Mech. Phys. Solids* 49, 1747–1769. doi:10.1016/S0022-5096(01)00010-2
- Galassi, C., 2006. Processing of porous ceramics: Piezoelectric materials. *J. Eur. Ceram. Soc.* 26, 2951–2958.
- Gonzenbach, U.T., Studart, A.R., Tervoort, E., Gauckler, L.J., 2007. Macroporous Ceramics from Particle-Stabilized Wet Foams. *J. Am. Ceram. Soc.* 90, 16–22. doi:10.1111/j.1551-2916.2006.01328.x
- Harshe, R.R., 2004. Synthesis and processing of amorphous Si(Al)OC bulk ceramics: high temperature properties and applications (PhD dissertation). Darmstadt TU.
- Hausner, H.H., 1981. Powder characteristics and their effect on powder processing. *Powder Technol.* 30, 3–8. doi:10.1016/0032-5910(81)85021-8
- Hill, R., 1965. A self-consistent mechanics of composite materials. *J. Mech. Phys. Solids* 13, 213–222. doi:10.1016/0022-5096(65)90010-4
- Imhof, A., Pine, D.J., 1997. Ordered macroporous materials by emulsion templating. *Nature* 389, 948–951. doi:10.1038/40105
- Jayaseelan, D.D., Kondo, N., Brito, M.E., Ohji, T., 2002. High-Strength Porous Alumina Ceramics by the Pulse Electric Current Sintering Technique. *J. Am. Ceram. Soc.* 85, 267–269.
- Jee, C.S.Y., Guo, Z.X., Evans, J.R.G., Özgüven, N., 2000. Preparation of high porosity metal foams. *Metall. Mater. Trans. B* 31, 1345–1352.
- Koponen, S., Toratti, T., Kanerva, D.P., 1991. Modelling elastic and shrinkage properties of wood based on cell structure. *Wood Sci. Technol.* 25, 25–32. doi:10.1007/BF00195554



- Lee, Y.-H., Lee, B.-K., Jeon, I., Kang, K.-J., 2007. Wire-woven bulk Kagome truss cores. *Acta Mater.* 55, 6084–6094. doi:10.1016/j.actamat.2007.07.023
- Luyten, J., Mullens, S., Cooymans, J., De Wilde, A.M., Thijs, I., Kemps, R., 2009. Different methods to synthesize ceramic foams. *J. Eur. Ceram. Soc.*, Referred Papers Presented at 3rd International Conference on Shaping of Advanced Ceramics (Shaping 3) 3rd International Conference on Shaping of Advanced Ceramics 29, 829–832. doi:10.1016/j.jeurceramsoc.2008.07.039
- Ohji, T., Fukushima, M., 2012. Macro-porous ceramics: processing and properties. *Int. Mater. Rev.* 57, 115–131. doi:10.1179/1743280411Y.0000000006
- Ramakrishnan, N., Arunachalam, V.S., 1993. Effective Elastic Moduli of Porous Ceramic Materials. *J. Am. Ceram. Soc.* 76, 2745–2752. doi:10.1111/j.1151-2916.1993.tb04011.x
- Rice, R.W., 1998. *Porosity of Ceramics: Properties and Applications*. CRC Press.
- Roberts, A.P., Garboczi, E.J., 2000. Elastic Properties of Model Porous Ceramics. *J. Am. Ceram. Soc.* 83, 3041–3048. doi:10.1111/j.1151-2916.2000.tb01680.x
- Roy, D.M., Linnehan, S.K., 1974. Hydroxyapatite formed from Coral Skeletal Carbonate by Hydrothermal Exchange. *Nature* 247, 220–222. doi:10.1038/247220a0
- Saggio-Woyansky, J., Scott, C.E., Minnear, W.P., 1992. Processing of porous ceramics. *Am. Ceram. Soc. Bull.* 71, 1674–1682.
- Sieber, H., Hoffmann, C., Kaindl, A., Greil, P., 2000. Biomorphic Cellular Ceramics. *Adv. Eng. Mater.* 2, 105–109. doi:10.1002/(SICI)1527-2648(200003)2:3<105::AID-ADEM105>3.0.CO;2-P
- Studart, A.R., Gonzenbach, U.T., Tervoort, E., Gauckler, L.J., 2006. Processing routes to macroporous ceramics: a review. *J. Am. Ceram. Soc.* 89, 1771–1789.
- Wang, J., Evans, A.G., Dharmasena, K., Wadley, H.N.G., 2003. On the performance of truss panels with Kagomé cores. *Int. J. Solids Struct.*, Special issue in Honor of George J. Dvorak 40, 6981–6988. doi:10.1016/S0020-7683(03)00349-4
- Wang, X., Ni, Q., 2003. Determination of cortical bone porosity and pore size distribution using a low field pulsed NMR approach. *J. Orthop. Res.* 21, 312–319.
- Wu, B.M., Cima, M.J., 1999. Effects of solvent-particle interaction kinetics on microstructure formation during three-dimensional printing. *Polym. Eng. Sci.* 39, 249–260. doi:10.1002/pen.11411
- Yan, C., Hao, L., Hussein, A., Raymont, D., 2012. Evaluations of cellular lattice structures manufactured using selective laser melting. *Int. J. Mach. Tools Manuf.* 62, 32–38. doi:10.1016/j.ijmachtools.2012.06.002
- Yang, S.F., Leong, K.F., Du, Z.H., Chua, C.K., 2002. The design of scaffolds for use in tissue engineering. Part II. Rapid prototyping techniques. *Tissue Eng.* 8, 1–11. doi:10.1089/107632702753503009
- Yeong, W.Y., Chua, C.K., Leong, K.F., Chandrasekaran, M., 2004. Rapid prototyping in tissue engineering: challenges and potential. *Trends Biotechnol.* 22, 643–652. doi:10.1016/j.tibtech.2004.10.004

## CHAPTER 2

Partially in publication:

Zocca A, Elsayed H, Bernardo E, Gomes CM, Lopez-Heredia M, Knabe C, Colombo P, Günster J.  
3D-printed silicate porous bioceramics by using a non-sacrificial preceramic polymer binder.  
Submitted to Biofabrication 2015

## CHAPTER 2

### **Bioceramic scaffolds produced by powder-based 3D-printing of preceramic polymers and fillers**

#### **2.1 Bioceramics: role and major classes**

Bioceramics form an important class of biomaterials with important applications in orthopaedics and for dental implants. Ceramic materials are often used to repair or replace parts of hard connective tissues.

It is important to recognize the types of responses that a tissue can have in response to the implantation of a foreign material. Generally they can be classified in four types (L. Hench, in (Ratner, 2004)):

- 1) The material is toxic: the tissue dies
- 2) The material is non-toxic and biologically inert: it is encapsulated by fibrous tissue
- 3) The material is non-toxic and bioactive: a bond between tissue and material forms
- 4) The material is non-toxic and biodegradable: the tissue gradually replaces the material

Naturally, the first case should be carefully avoided by the selection of materials which are non-toxic and which don't have toxic degradation products or contaminations. Instead, bioinert, bioactive and biodegradable ceramics can all be used as biomaterials, depending on the application.

Alumina ( $\text{Al}_2\text{O}_3$ ) and zirconia ( $\text{ZrO}_2$ ) are the two most used bioinert ceramics and they find use mainly in hip joint replacement. A hip joint replacement is composed by an acetabular cup and a head supported by a metal stem (often titanium). Usually a polymeric (UHMW-polyethylene) insert is used in between cup and head.

Alumina and zirconia are used in this application because of their hardness and low friction, along with a high mechanical strength which guarantees the mechanical stability of the implant for possibly dozens of years. Alumina has a higher hardness over zirconia and lower density, while on the other side bio-grade zirconia generally has higher flexural strength and higher toughness than alumina. For such application indeed yttria or yttria and magnesia partially stabilized zirconia are used, in which the microstructure consists of a cubic phase stabilized at room temperature with precipitates of a tetragonal phase. A phase transformation at the crack tip causes a volume expansion which can stop the crack propagation, thus increasing the toughness of the material. The use of implants of a bioinert ceramic is successful as long as only a fibrous capsule of tissue forms

around it, which is the case of alumina implants under compressive loads and with a tight mechanical fit. However, movement can cause a thickening of the fibrous capsule and a loosening of the implant. Another issue is that friction debris can cause irritation and damage of the surrounding biological tissues.

The use of a porous material or of a material with a porous surface can help the fixation of an implant, providing a higher surface for the mechanical attachment of the living tissues or the ingrowth in the case of a porous structure of sufficient porosity (pore size > 100  $\mu\text{m}$  is often considered a lower limit).

*Bioactive* materials have potentially better performances for many applications, since they can directly attach to the tissue without formation of an interfacial layer, but via a chemical bonding. The definition of bioactivity implies that the material elicits a positive reaction of the tissues which can help their regeneration and their attachment.

*Resorbable* biomaterials also form a direct bond to the tissue, but they degrade with the time. The most desirable situation is that the implant carries the mechanical load after implantation and then slowly degrades while it is substituted by living tissue; at the end of an optimized process the implant should be completely resorbed and substituted. This behaviour is optimal for many applications (such as bone implants) but the conditions are also harder to match:

- The implant should have enough mechanical strength to withstand the initial stress by itself.
- The material should resorb gradually and the tissue should grow at a similar rate. If the implant resorbs too quickly, the tissue will have no time to substitute it and this causes a loss of bearing of the mechanical stresses.

Starting from the '80, two important classes of ceramics have started to see use in tissue engineering: calcium phosphates and bio-glasses.

Calcium phosphates (Jarcho, 1981) have a composition which is similar to the ceramic fraction of bone. Indeed, at the conditions of blood ( $T \approx 37^\circ\text{C}$ ,  $\text{pH} \approx 7$ ) the stable calcium phosphate phase is hydroxyapatite (HA,  $\text{Ca}_{10}(\text{PO}_4)_6(\text{OH})_2$ ), which is the main crystalline phase of bone, even though HA in bone contains also traces of different ions ( $\text{OH}^-$ ,  $\text{F}^-$ ,  $\text{CO}_3^{2-}$ ). Other calcium phosphate phases can be synthesized at higher temperatures by solid state reactions or at low temperature by precipitation methods (Elliott, 1994).  $\beta$ -tricalcium phosphate (TCP,  $\text{Ca}_3(\text{PO}_4)_2$ ) is probably the most investigated so far due to its good biocompatibility and resorbability (depending on porosity, microstructure and location of the implant). TCP in blood environment reacts with water to form

HA, which is deposited on its surface. Therefore it is slowly resorbed with time and it is covered by a layer of HA, which favours its properties of osteoconduction (Shimazaki and Mooney, 1985).

In the '70s dates back the discovery of the first artificial material able to create a strong direct bond with hard and soft (some composition) tissues: bioglass (Hench and Paschall, 1973). Unlike conventional soda-lime glass, bioglass has a low amount of network former ( $\text{SiO}_2$ ), high amount of network modifiers and a high  $\text{CaO}/\text{P}_2\text{O}_5$  ratio. The most studied composition was labelled 45S5 and had 45% (mol)  $\text{SiO}_2$  and a ratio  $\text{CaO}/\text{P}_2\text{O}_5= 5$ . This kind of glass has a high surface reactivity and it bonds to bone with little to none layer of fibrous tissue.

The mechanism of glass dissolution in water involves a first step of ionic exchange between alkali in the glass and  $\text{H}^+$  ions from the liquid, with formation of a silica rich layer, often called gel layer. This gel layer (as for soda lime glass e.g.) is in the alkaline pH generally not protective and its dissolution is favoured because the previous exchange reactions increase the pH of the solution. In bioglass, an amorphous protective layer rich in  $\text{CaO}$  and  $\text{P}_2\text{O}_5$  precipitates on the surface and with time it tends to crystallize forming carbonated HA. The formation of this layer is considered to be the reason for the excellent bonding of bioglass to bone. More recent research highlighted that the ions released by bioglass, especially  $\text{Si}^{4+}$ , elicit a positive response in the replication and differentiation of osteoblastic cells (Xynos et al., 2000), also having an influence on several genes (Xynos et al., 2001). There exist glass-ceramics that behave in a similar way as bioglass. An important class is in the apatite/wollastonite (A/W) system, first developed by Kokubu ((Kitsugi et al., 1987). These glass-ceramics develop a Ca-P rich layer on the surface when immersed in simulated body fluid (SBF, a fluid which has approximately the same species and content of ions as blood) which develops into carbonated HA. A correlation has been shown for different glasses and glass-ceramics between the ability of forming an apatite layer on the surface of a material and their ability of bonding to bone (Kokubo and Takadama, 2006). However this approach has been criticized (Bohner and Lemaitre, 2009) and it is not general for all materials; it is a matter of fact that some other silicate ceramics can bond to bone, but do not form an apatite layer in SBF, and there are also examples of the contrary (Walsh et al., 2003).

Other materials can form a strong bond with bone, among these particularly calcium phosphates. Hydroxyapatite (HA,  $\text{Ca}_{10}(\text{PO}_4)_6(\text{OH})_2$ ) has high biocompatibility due to its similarity to the crystalline phase of bone, which is a calcium deficient carbonated HA. The mechanism of HA bonding with bone is different to that of bioglass. While not completely clarified, it involves a dissolution-precipitation step which creates an amorphous layer on the surface containing apatite nanocrystals. Pre-osteoblastic cells attach to the surface and differentiate forming a cellular bone

matrix. This bonding zone shrinks and HA becomes attached to bone through a thin epitaxial layer, resulting in a strong interface with no layer of fibrous tissue interposed between the bone and HA (Hamadouche and Sedel, 2000). The biological incorporation of collagen fibres with HA and chemical bonding of an apatite layer were both necessary to strengthen and toughen a bone bond (Chen et al., 2004). Tricalcium phosphate (TCP,  $\text{Ca}_3(\text{PO}_4)_2$ ) is another important calcium phosphate which is a resorbable phase, which can bind bone and is resorbed by two mechanisms (i) osteoclastic resorption (ii) dissolution reaction of TCP with water to form HA (Hench, 1991). Silicate ceramics have been extensively studied in the recent literature and they will be briefly reviewed in the following paragraph 2.1.1.

### **2.1.1 Silicate bioceramics**

The bioactivity of silicate ceramics is generally considered to be related to the release of ionic products from the material.  $\text{Ca}^{2+}$  and  $\text{Si}^{4+}$  ions can indeed stimulate the proliferation and differentiation of the osteoblasts (Valerio et al., 2004) (Maeno et al., 2005), up-regulating and activating several genes (Hench, 2009). Furthermore, silicate ceramics can stimulate the angiogenesis (Zhai et al., 2012) and also have an antibacterial effect (Hu et al., 2011).

The dissolution rate and the release of ions are very important for the properties of silicate bioceramics as well as the type and amount of ions released from the material. However, an excessive and quick dissolution of the material can also be detrimental to cells. In particular, a mild increase in pH related to the material dissolution can have a positive effect (such as antibacterial), but a steep local increase in pH can be harmful (El-Ghannam et al., 1997). Also, bioceramics with a high dissolution rate such as wollastonite are considered to be osteoinductive, but they lack osteoconductivity because their dissolution does not match the bone growth rate (Wang et al., 2012). Furthermore, it is important to develop ceramic systems with different degradation rates and mechanical properties for different medical applications. Silicate bioceramics are excellent potential candidates for fulfilling these broad requirements, since their biological-related properties vary in a wide range of values, especially concerning their dissolution rate in human blood environment and their ability of forming an apatite layer when immersed in simulated body fluid (SBF).

It was found (Wu and Chang, 2013) that their dissolution rate can vary in a range from very high to very low, and that a high dissolution rate generally corresponds to a good apatite formation ability.

Table 1 reports a list of the most studied silicate bioceramic phases and their characteristics, compared to the properties of other bioceramics and those of bone:

<b>Material</b>	<b>Composition</b>	<b>Bending strength (MPa)</b>	<b>Elastic Modulus (GPa)</b>	<b>Apatite formation in SBF</b>	<b>Dissolution</b>
<b>Wollastonite</b>	CaSiO <sub>3</sub>	95 (a)	46 (a)	Excellent (a)	Quick (a)
<b>Dicalcium silicate</b>	Ca <sub>2</sub> SiO <sub>4</sub>	26-97 (a)	10-40 (a)	Excellent (a)	Quick (a)
<b>Tricalcium silicate</b>	Ca <sub>3</sub> SiO <sub>5</sub>	93 (a)	37 (a)	Excellent (a)	Quick (a)
<b>Magnesium silicate</b>	MgSiO <sub>3</sub>	32 (a)	8.5 (a)	Poor (a)	Very slow (a)
<b>Zinc silicate</b>	Zn <sub>2</sub> SiO <sub>4</sub>	91 (a)	38 (a)	Poor (a)	Very slow (a)
<b>Akermanite</b>	Ca <sub>2</sub> MgSi <sub>2</sub> O <sub>7</sub>	176 (a)	42 (a)	Good (a)	Common (a)
<b>Bredigite</b>	Ca <sub>7</sub> MgSi <sub>4</sub> O <sub>16</sub>	156 (a)	43 (a)	Excellent (a)	Quick (a)
<b>Diopside</b>	CaMgSi <sub>2</sub> O <sub>6</sub>	300 (a)	-	Common (a)	Slow (a)
<b>Hardystonite</b>	Ca <sub>2</sub> ZnSi <sub>2</sub> O <sub>7</sub>	136 (a)	37 (a)	Poor (a)	Very slow (a)
<b>Strontium-hardystonite</b>	Sr <sub>2</sub> ZnSi <sub>2</sub> O <sub>7</sub>	82 (b)	-	Poor (a)	Very slow (a)
<b>Sphene</b>	CaTiSiO <sub>5</sub>	-	-	Poor (a)	Very slow (a)
<b>Baghdadite</b>	Ca <sub>3</sub> ZrSi <sub>2</sub> O <sub>9</sub>	98 (c)	82-120 (c)	Common (a)	Slow (a)
<b>Hydroxyapatite</b>	Ca <sub>10</sub> (PO <sub>4</sub> ) <sub>6</sub> (OH) <sub>2</sub>	38-250 (c)	80-110 (c)		
<b>Bioglass</b>		42 (c)	35 (c)		
		(tensile)			
<b>A/W glass-ceramic</b>		220 (c)	118 (c)		
<b>Cortical bone</b>		50-193 (c)	7-30 (c)		
<b>Spongy bone</b>		10-20 (c)	0.1-5 (c)		

Table 1 Properties of silicate ceramics compared to bone and to other bioceramics. Data are reported from (a) (Wu and Chang, 2013) (b) (Zhang et al., 2012) (c) (Schumacher et al., 2014) and their references.

In this scale, in particular, wollastonite has a high dissolution rate and high apatite formation ability, while other compositions, such as hardystonite, have a low solubility and a low apatite formation ability. These two phases will be of particular interest for chapters 2 and 3. It has also been shown that wollastonite monoliths prepared by pressureless sintering generally have a lower bending strength (20-50 MPa (Endo et al., 1994), 95 MPa (Lin et al., 2005)) than hardystonite (136 MPa (Wu et al., 2005)) monoliths, even though the application of an SPS sintering technique allowed the production of a high strength wollastonite (294 MPa (Long et al., 2006)).

A ceramic implant should have mechanical properties resembling those of bone. It can be noted, however, that ceramics with a high mechanical strength, generally have an elastic modulus higher than cortical bone and especially than spongy bone. This is even more relevant for inert bioceramics such as alumina, which has high strength, but also an elastic modulus of about 300 GPa, which is more than 10 times that of cortical bone. The consequence of this mismatch is that an implant with high elastic modulus will carry more mechanical load than the surrounding bone; when bone is unloaded, it tends to remodel and become thinner, thus causing osteoporosis. This phenomenon is known as “stress-shielding” effect (Woo et al., 1976). For this reason, when the mechanical strength required for an implant is limited, porous ceramics can be used; porous structures can create a scaffold for the ingrowth of new bone and the porosity can be designed to create an implant with a stiffness similar to that of the surrounding bone. It has been shown in paragraph 1.1 how porosity influences the elastic properties of a material.

The following paragraph 2.2 describes the synthesis of silicate bioceramics and composites from preceramic and fillers precursors. Paragraph 2.2.2.2 illustrates the process of 3D-printing for some of these mixtures, finalized to the production of porous scaffolds.

## **2.2 Synthesis of bio-silicate ceramics and composites from preceramic polymers and fillers**

### **2.2.1 AP40 glass-ceramic**

#### **Materials and methods**

AP40 is a proprietary glass (BAM, Berlin, Germany; density 2.799 g/cc) that crystallizes into an apatite/wollastonite (A/W) glass ceramic upon heating. The AP40 glass powder had a composition (wt%): 44.30 SiO<sub>2</sub>, 31.89 CaO, 11.21 P<sub>2</sub>O<sub>5</sub>, 0.20 K<sub>2</sub>O, 4.60 Na<sub>2</sub>O, 2.80 MgO, 5.00 CaF<sub>2</sub> and a density of 2.799 g/cm<sup>3</sup>. It was prepared by mixing pure raw materials for 2h in a tubular mixer followed by melting process for 3h at 1550°C in a platinum crucible. After cooling, large glass



fragments removed from the crucible were ground by means of jaw crusher with decreasing gap between the jaws down to 100  $\mu\text{m}$ ; the resulting powders were carefully sieved to different sizes: (< 25  $\mu\text{m}$ ), (25-45  $\mu\text{m}$ ), (45-90  $\mu\text{m}$ ) and (90-100  $\mu\text{m}$ ).

The crystallization of the AP40 glass powder was assessed by using differential thermal analysis (DTA, Netzsch STA 429, Germany) at 10°C/min in air. The effect of AP40 glass particle size on the crystallization behavior was studied using powders with different size. For the apatite/wollastonite glass-ceramic formation, the AP40 glass powder was heat treated at different temperatures (720 and 900°C) that cover the crystallization range of AP40 and were also used for crystallizing bulk samples in previous works (Reichelt et al., 1986) (Picker et al., 1993). The heating rate was 2°C/min and the holding time was 1h or 5h; then the furnace was turned off and the samples subjected to cooling to room temperature. Some experiments were also conducted using a two-step heating, with holding time at 720°C of 1 or 5h followed by heating at 900°C for 1 or 5h. The crystalline phases evolution was investigated using X-Ray diffraction (XRD, Bruker AXS-D8 advance, Germany). The XRD analysis was performed on powdered samples with  $\text{Cu}_{\alpha 1}$  radiation (10 to 70° 2 $\theta$ , 2 sec/step). A semi-automatic phase identification was provided by the Match! software package (Crystal Impact GbR, Germany), supported by data from PDF-2 database (ICDD-International Centre for Diffraction Data, USA).

## **Results and discussion**

The DTA curves of AP40 glass powder (indicated with the label G) with different particle size are reported in *Figure 1*. The glass transition temperature ( $T_G$ ) was assessed to be ~ 640 °C. In all curves, two exothermic peaks can be easily noted. The first peak ( $T_{C1}$ ) at ~ 770°C can be associated with the crystallization of fluorapatite, according to XRD analysis after the heat treatment at 720°C; the second exothermic peak ( $T_{C2}$ ), at ~ 860-890°C, can be attributed to the crystallization of wollastonite-2M, as confirmed by XRD findings on samples heat treated at 900°C.

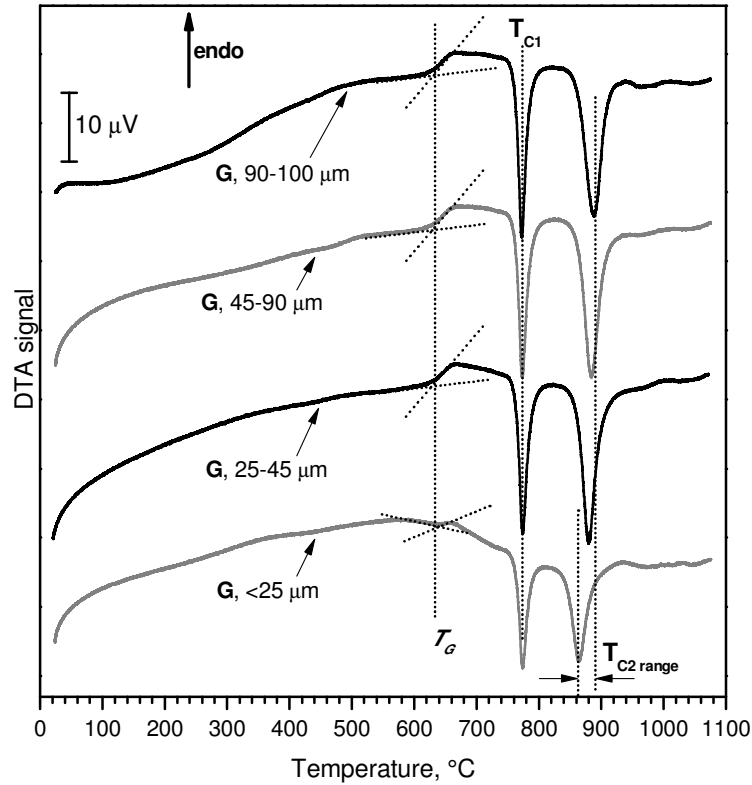


**Figure 1** DTA curves for AP40 glass powders (G) of different particle size.

The fact that the position of the first crystallization peak is nearly independent of the particle size indicates that the crystallization mechanism for the apatite phase is bulk crystallization, rather than surface crystallization. The relatively small differences in the position of the second peak can be instead attributed to an influence of surface crystallization for wollastonite. It was indeed observed that wollastonite crystals grow on the surface of glass particles both in an A/W glass-ceramic (Likitvanichkul and Lacourse, 1998) and in a  $\text{SiO}_2\text{-Al}_2\text{O}_3\text{-CaO-Na}_2\text{O}$  glass (Pérez et al., 2012). The X-ray diffraction patterns of AP40 glass with different particle size after heat treatment at 720°C and 900°C for 1 and 5h are reported in *Figure 2*.

The XRD patterns for AP40 powder heat treated at 720°C for 1h (*Figure 2*) show that crystals of fluorapatite are formed in an amorphous matrix (there is still a clear amorphous hump). After heat treatment at 900°C for 1h, a second crystalline phase of wollastonite-2M developed.

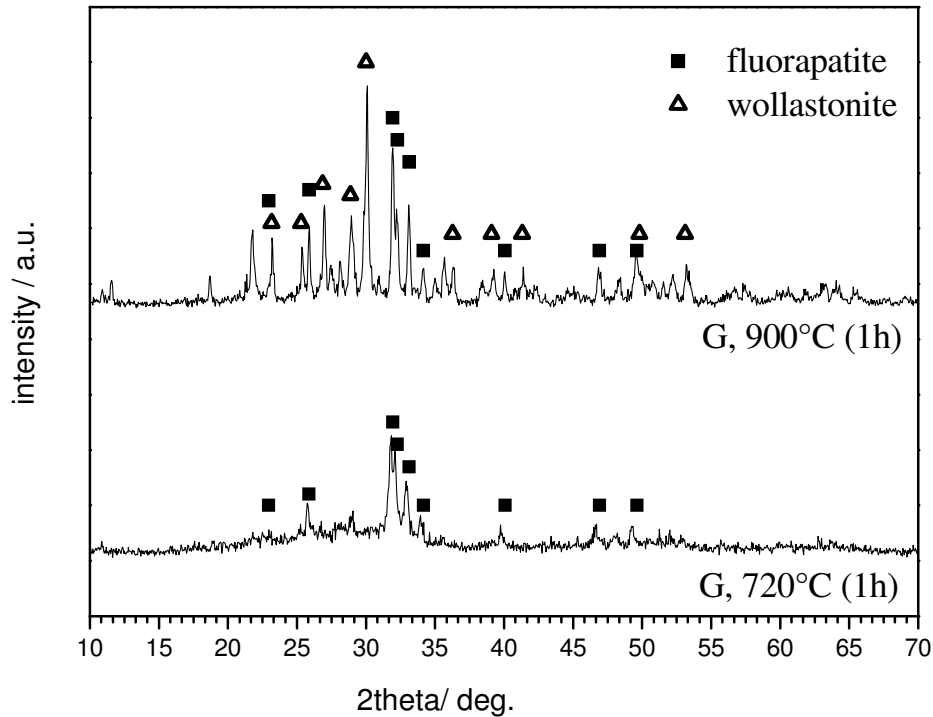


**Figure 2** XRD patterns of AP40 powder < 25 $\mu$ m heat treated at 720°C (1h) and 900°C (1h)

These results confirmed that AP40 belongs to the group of A/W glass-ceramics.

## 2.2.2 AP40/wollastonite composites from preceramic polymer and fillers

### 2.2.2.1 Pressed samples

#### Materials and methods

The preceramic polymer used in the present research was a polymethylsiloxane, SILRES<sup>®</sup> MK (Wacker-Chemie GmbH, Germany) that is known to be converted, after the heating in air, into amorphous silica (SiO<sub>2</sub>) with a ceramic yield of 84 wt%. The MK silicone resin, in powder form, was dissolved in isopropyl alcohol under magnetic stirring for 10 min, then mixed with micro and nano-sized active and passive fillers, followed by sonication to obtain homogenous dispersions which were left to dry overnight at 60°C in air. The active fillers consisted of micro-sized CaCO<sub>3</sub> (<10  $\mu$ m, Sigma–Aldrich Ltd, UK) to obtain wollastonite-based ceramics; the passive filler was represented by AP40 powder. MK polymer and CaCO<sub>3</sub> were mixed in stoichiometric ratio to form

wollastonite. Two composite compositions were chosen, one with a high amount of AP40 inert filler and one with a lower amount. The former, labeled HG (high glass), was designed to give 80 wt% AP40 and 20 wt% wollastonite after heat treatment. The latter, labeled LG (low glass), was designed to give 40 wt% AP40 and 60 wt% wollastonite.

The crystalline phases evolution was investigated by X-Ray diffraction (XRD, Bruker AXS-D8 advance, Germany).

## Results and discussion

Paragraph 4.2.1 showed that AP40 formed an apatite-wollastonite glass-ceramic when heat treated at 900°C. Previous work also demonstrated that wollastonite can be obtained from conversion of preceramic polymer MK and CaCO<sub>3</sub> filler at the same temperature of 900°C (Bernardo et al., 2012).

It was therefore speculated that apatite-wollastonite composite glass-ceramics could be obtained by a mixture of MK, CaCO<sub>3</sub> and AP40 by heat treatment at this temperature.

The results of XRD analysis on pressed tablets of composition HG and LG are reported in *Figure 3*.

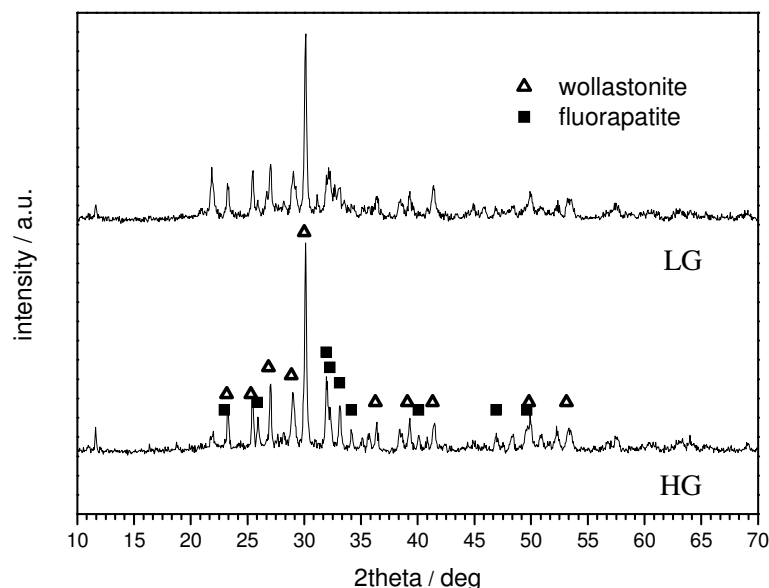


**Figure 3** XRD patterns of composites HG (high glass) and LG (low glass) heat treated at 900°C

The patterns verified that the phases formed are apatite and wollastonite, as it was in the case of AP40. However, as expected the content of wollastonite in formulation HG and LG was higher than that developed from G (AP40 glass). This can be semi-quantitatively deduced from the ratio of the main wollastonite peak and the main apatite peak (compare *Figure 2* and *Figure 3*), which increases in the order LG > HG > G, see (Elsayed et al., 2015). The additional wollastonite in samples HG and LG compared to G derived from the reaction between silica (derived from the MK polymer) and CaO (derived from CaCO<sub>3</sub>). The data indicated that no interaction between the AP40 glass particles and either the preceramic polymer or calcium carbonate occurred, and AP40 was confirmed to behave as a passive filler.

### 2.2.2.2 Powder-based 3D-printing

#### Materials and methods

##### *Preparation of powder mixtures for the 3D-printing process*

By mixing the preceramic polymer, CaCO<sub>3</sub> (Bitossi, Italy) and AP40 glass in specific ratios, different compositions were designed for the 3D-printing process, following *Table 2*.

	<b>G = glass (AP40) (wt% after heat treatment)</b>	<b>HG = high glass (wt% after heat treatment)</b>	<b>LG = low glass (wt% after heat treatment)</b>	<b>W = wollastonite (wt% after heat treatment)</b>
AP40 glass-ceramic	100	80	40	0
Wollastonite (from preceramic polymer)	0	20	60	100

**Table 2** Labelling and designed composition of the composite materials investigated.

Here 3D-printed discs of type G were also produced by 3D-printing an AP40 powder with a commercial 3D-printer (RX-1, Prometal RCT GmbH, Germany) which makes use of a binder

directly mixed with the printing liquid. An as-sieved AP40 powder in the range 45-90  $\mu\text{m}$  was used to achieve a good flowability.

Powder mixtures for the 3D-printing process were prepared by dry mixing the raw materials in a tumbling mixer for 3h followed by a granulation process. Briefly, the granulation was obtained by depositing a thin ( $< 1$  mm) layer of powder and spraying isopropanol from the top; after sieving between 45 and 125  $\mu\text{m}$ , a granulated powder mixture with the desired particle size distribution was obtained.

After the granulation process, the granule size and the size distribution were measured by laser granulometry (Mastersizer S, Malvern Instruments GmbH, Germany). The flowability of the granulated was assessed by the Hausner ratio (HR), according to *Eq. 2* (Hausner, 1981):

$$\text{HR} = \rho_{\text{Tap}} / \rho_{\text{Bulk}} \quad (\text{Eq. 1})$$

Where  $\rho_{\text{Bulk}}$  is the freely settled bulk density ( $\text{g}/\text{cm}^3$ ) of the powder and  $\rho_{\text{Tap}}$  the plateau tap density ( $\text{g}/\text{cm}^3$ ) of the powder. Each measurement of the HR was repeated three times ( $n = 3$ ).

### ***Powder-based 3D-printing process***

In order to print the materials a printing head with 128 jets (Spectra SL128-AA, Dimatix Fujifilm USA, CA) mounted in a commercially available printer (Voxeljet Teststand VTS 16, Voxeljet Technology GmbH, Germany) was used. The system used a blade recoating system. A powder mixture of the polymer, active filler and inactive filler was used to deposit layers with a thickness of 150  $\mu\text{m}$ . A mixture of 1-hexanol and hexylacetate (Voxeljet, Germany) was used as a printing liquid (Zocca et al., 2013). Printing liquid was injected through the nozzles of the printing head in order to obtain the required cross-section of the object for a given layer. This process was repeated until completion of the designed object. The printed part was left to dry in the powder bed overnight. Then, it was extracted from the surrounding powder-bed and gently cleaned with a brush and compressed air. In order to obtain a completely ceramic part, the green samples were subsequently heat treated in air at 900°C for 1 h with a heating rate of 2°C/min.

A mixture of 1-hexanol and hexylacetate (Voxeljet, Germany) was used as a printing liquid (see (Zocca et al., 2013) and paragraph 1.2). The ratio between the mass of solvent and the mass of powder (R) used to print a part was calculated as previously described. Differently from previous experiments, the addition of a cross-linking catalyst was no longer necessary when using a relatively high amount of fillers (as in this work),. This is because the geometry of the part remains

stable thanks to the support provided by the inorganic fillers, even when the temperature is increased above the polymer's T<sub>g</sub>.

For each composition 3D-printed discs with dimensions of 16 mm diameter and 3 mm in thickness were obtained to evaluate their shrinkage and density. The dimensions of the discs and their density were measured before and after heat treatment. Density was obtained by the Archimedes' method using deionized water. Briefly, the dry mass of printed discs was measured after keeping them for 24 hours at 150°C. Afterwards they were placed in boiling water for 5 hours for impregnation and their suspended and immersed masses in water were measured. From the measurements of the dry, suspended and impregnated masses, the apparent density and open porosity values were calculated (ASTM C373-88). Shrinkage was measured using a digital caliper, measuring each tablet on different locations to obtain a representative value. Six samples of type HG (n = 6) and four samples of type LG (n = 4) were measured.

Three-dimensionally printed samples were observed after heat treatment under a scanning electron microscope (SEM) (Zeiss Gemini Supra 40, Carl Zeiss GmbH, Germany), in order to investigate the morphology and the morphological changes.

### ***In vitro cell tests***

MC3T3-E1 subclone 4 cells (ATCC, USA) were used. Medium consisted of DMEM (Gibco, Germany) supplemented with 10% FBS (Sigma-Aldrich, Germany), 2mM L-Glutamine (Gibco, Germany), 50µg/ml of *ascorbic acid* (Sigma-Aldrich, Germany), 5mM β Glycerophosphate (Sigma-Aldrich, Germany) and 50µg/ml of *Penicillin-Streptomycin* (Gibco, Germany). *Cells were cultured in T75 cell culture flasks with 12 ml of medium. The medium was refreshed three times a week. For amplification, cells were grown until confluence in cell culture flasks and then detached with a 0.25% trypsin/0.02% EDTA (BioChrom, Germany) solution and passaged. Cells were seeded on discs with dimensions of 10 mm in diameter by 2.5 mm in height. Before performing the seeding, discs were heat sterilized at 300°C for 3 h and then placed in cell culture medium for 24 h. After this period, medium was removed and a specific amount of cells per disc was seeded on the top of the discs, i.e. 50, 000 cells in an 80 µl drop. After 3, 7 and 14 days of culture, cell proliferation, cytotoxicity and apoptotic behavior were measured by using an AlamarBlue® assay (Invitrogen, Germany), a CellTox Green® assay (Promega, Germany) and a Caspase 3/7® assay (Promega, Germany), respectively. Assays were performed in triplicate (n = 3).*

The CellTox™ Green Cytotoxicity assay measures changes in membrane integrity that occur as a result of cell death. The assay system uses a proprietary dye that preferentially stains the dead cells'

DNA. When the dye binds DNA in compromised cells, the dye's fluorescent properties are substantially enhanced and the fluorescent signal produced by the dye binding to the dead-cell DNA is proportional to cytotoxicity (Promega technical manual).

Caspase is an enzyme involved in cell apoptosis. The assay provides a proluminescent caspase-3/7 substrate, which contains the tetrapeptide sequence DEVD, in a reagent optimized for caspase activity, luciferase activity and cell lysis. The addition of the reagent results in cell lysis, followed by caspase cleavage of the substrate and generation of a luminescent signal, produced by luciferase. The luminescence signal is proportional to the amount of caspase activity (Cai et al., 2001).

Cells seeded at different densities in normal plastic wells were used as standards for comparison purposes for the viability tests, i.e. AlamarBlue®. This standard included different cell densities from  $1 \times 10^6$  to zero, or a blank value for zero live cells. The cytotoxicity assay used only a blank value as comparison point to have a signal for no dead cells, or zero dead cells. For the apoptosis assay the results were only relative to the other samples.

Three-dimensionally printed samples were observed under a scanning electron microscope (SEM) (Zeiss Gemini Supra 40, Carl Zeiss GmbH, Germany) both before and after the in vitro tests, in order to investigate the morphology and the morphological changes.

### ***Statistical analysis***

Results are expressed as mean  $\pm$  standard deviation. Where applicable, statistical significance ( $p < 0.01$ ) of the results was assessed using the student t-test.

## **Results and discussion**

### ***Preparation of powder mixtures for the 3D-printing process***

**Figure 4 (a)** and **(b)**. displays the SEM analysis for the two powder compositions obtained. After granulation both compositions present a similar morphology with an equiaxial particle shape.



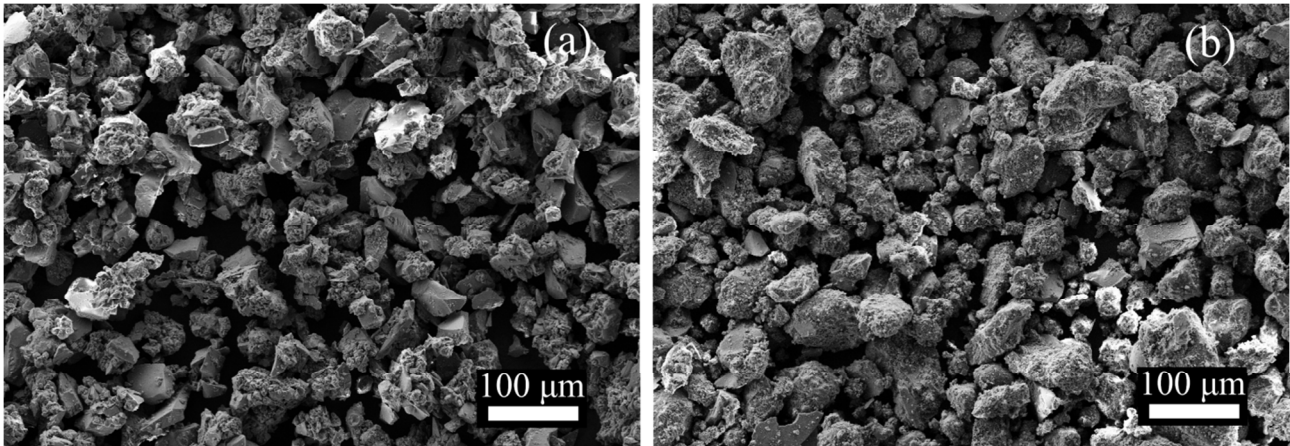


**Figure 4** SEM micrographs of (a) HG and (b) LG granulated powder mixtures used for 3D-printing. HG = high amount of glass filler, LG = low amount of glass filler.

The properties of the granulated powder mixtures are presented in *Table 3*

Powder mixture	d10 (µm)	d50 (µm)	d90 (µm)	Hausner Ratio
HG	14	44	80	1.28 ± 0.01
LG	19	85	146	1.23 ± 0.01

**Table 3** Particle size distribution and Hausner Ratio of the granulated powder mixtures. d10, d50, d90 indicate the diameter at which 10%, 50% and 90% of the particles are smaller than this value. HG = high amount of glass filler, LG = low amount of glass filler.

Granulated powders had a maximum particle size, i.e. the d90 value, and a mean particle size value, i.e. d50, of 80 µm and 44 µm for HG and of 146 µm and 85 µm for LG. Both compositions presented low fractions of small particles as the d10 values for HG and LG were 14 µm and 19 µm, respectively. The distribution values show that LG had a larger mean particle size.

The particle size distribution of both granulated powders was suitable for the layer-by-layer deposition, since the layer thickness used was 150 µm and the particles had mainly a diameter below this value. Powder HG had a mean dimension which was smaller than LG. This can be associated to the fact that composition LG had a higher amount of polymer, which probably favoured the growth of the size of the granules during the granulation process.

The HR values for HG and LG were 1.28 ± 0.01 and 1.23 ± 0.01, respectively. These values corresponded, based on our former experience (Zocca et al., 2014), to a fair flowability which is

sufficient for the deposition of a defect-free layer. A lower HR corresponds to a better flowability, because it is an indication that the powder is more efficiently packed already before tapping, and the increase in packing density after tapping is therefore lower. These HR values also agree with values associated with a fair or acceptable flowability for other powders (Hausner, 1981).

As expected, HG had a slightly worse flowability due to the fact that its mean particle size was smaller. It is known that flowability is greatly dependent on the Bond Number, which is the ratio between the gravitational forces and the interparticle forces that act on the single particles (Nase et al., 2001). Since the interparticle forces increase relative to the gravitational as the particle size decreases, it is expected that powders with a smaller particle size have a worse flowing behavior.

The SEM micrographs in *Figure 4* confirm that both powders were composed of granules of approximately equiaxial shape, which is favorable for the flowability. The observed mean dimension also roughly corresponded to the values reported in *Table 3*; HG had particles in the range close to 50  $\mu\text{m}$ , while LG had mostly larger granules, close to 100  $\mu\text{m}$  in diameter. Both HG and LG contained a similar and relatively low fraction of small particles, compatible with the measured values of  $d_{10}= 14\mu\text{m}$  and  $d_{10}= 19 \mu\text{m}$  respectively.

### ***Powder-based 3D-printing process***

*Table 4* presents the density, shrinkage and porosity results. HG after heat treatment had a radial linear shrinkage smaller than LG and a lower density value. The shrinkage values are in good correlation with the SEM observations, as HG presented the smaller change in its structure. Nevertheless, these values indicate a limited densification during the sintering process. The residual porosity was larger for HG than for LG. From the values of total and open porosity, it could be calculated that 92 % and 96 % of the total porosity was open porosity for samples HG and LG, respectively. The images highlight the fact that the samples were highly porous (> 50%, see *Table 4*) both in the green and in the ceramized state. HG had a more uniform morphology and smaller pores than LG. This characteristic seems to be related to the effect that the different amount of polymer has on the 3D-printing process. LG had a much higher amount of polymer, which was dissolved by the printing liquid and formed after re-precipitation an almost continuous polymeric phase containing the ceramic fillers, leaving relatively large and irregularly distributed pores (*Figure 5c*). After the heat treatment, large cracks formed on the surface (*Figure 5d*) which are due to the ceramization process, which is accompanied by shrinkage, and gas release. HG contained instead a lower- amount of polymer, which was only sufficient to locally bind the adjacent ceramic particles (*Figure 5a*).

<b>Powder mixture</b>	<b>R value</b>	<b>Density (g/cm<sup>3</sup>)</b>	<b>Total porosity (%)</b>	<b>Open porosity (%)</b>	<b>Shrinkage after Ceramization (%)</b>
<b>G</b>	*	1.48 ± 0.07	48 ± 2	48 ± 3	8.1 ± 0.4
<b>HG</b>	0.19	1.00 ± 0.01	63.8 ± 0.7	58.5 ± 0.9	5.2 ± 0.6
<b>LG</b>	0.08	1.30 ± 0.04	53.1 ± 0.7	51.0 ± 1.0	6.7 ± 0.5

\* Not applicable

**Table 4.** Printing parameters and density, porosity and radial shrinkage (measured radially) of printed parts after ceramization at 900°C. G = glass alone, HG = high amount of glass filler, LG = low amount of glass filler.

A continuous polymeric phase, covering the ceramic particles, such as seen in *Figure 5c* and *Figure 5d* could not be observed.

After the heat treatment, the morphology of the sample was comprised by a network of AP40 glass-ceramic particles, formed by sinter-crystallization (*Figure 5b* point 1), and a secondary phase deriving from the ceramization process and reaction of the preceramic polymer with the active filler CaCO<sub>3</sub>, which decomposed forming reactive CaO at the treatment temperature (*Figure 5b* point 2). The porosity of HG was smaller (<50-100 μm) and more homogeneously distributed than that of LG. This morphology is more desirable for the absence of cracks, a higher homogeneity and for the better printing precision that was achievable when printing HG compared to LG. HG had a lower shrinkage and densification compared to G. The densification mechanism for G during heat treatment is the sinter-crystallization of the glass particles; the addition of a secondary phase in HG reasonably partially hinders the densification, resulting in lower shrinkage and higher final porosity.

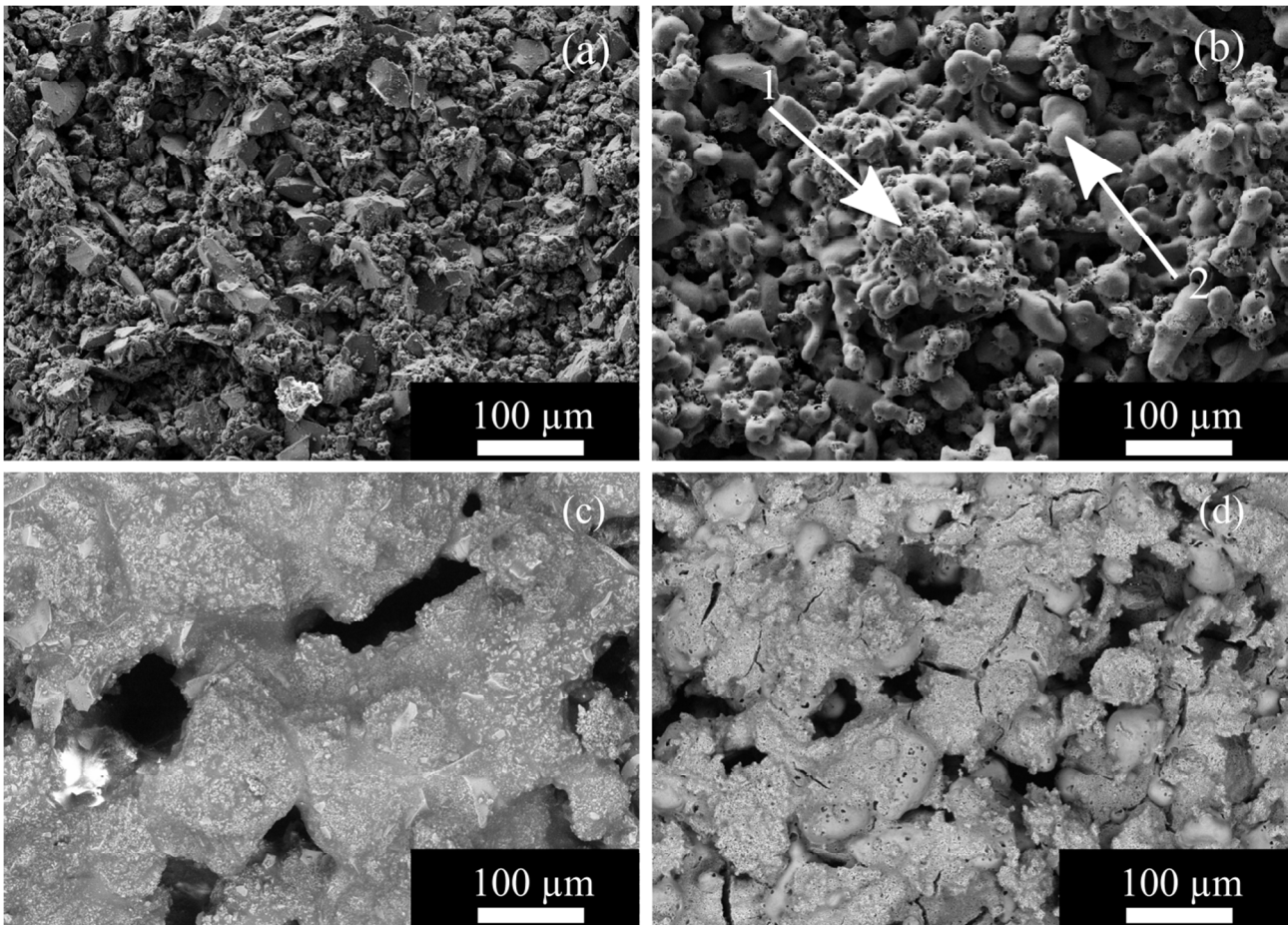


**Figure 5** SEM micrographs of the top surface of the printed samples before and after ceramization: (a,b) printed and ceramized HG, respectively; (c,d) printed and ceramized LG, respectively. Arrows indicate two phases deriving 1) from the reaction of the preceramic polymer and  $\text{CaCO}_3$  filler and 2) network of sintered AP40 particles.

This behavior, however, does not follow a linear trend with decreasing amount of glass filler in LG: the reason may be that the glass particles do not form a continuous network in this case, and the main contribution to the shrinkage becomes the reduction in volume which follows the polymer-to-ceramic transformation and the formation of the wollastonite phase.

Pores of this size are too small for cells ingrowth, since usually a pore size of 200-400 μm (Karageorgiou and Kaplan, 2005) and a large size of the interconnections (Bignon et al., 2003) is considered optimal. However, also the microporosity in the struts of a biomaterial has a role on their overall behavior. Chan et Al. (Chan et al., 2012) suggested that silicate-substitute calcium phosphate graft materials with higher strut porosity are more osteoconductive. They also noted bone formation in small pores < 10 μm, although these pores are probably too small for cells. Bignon et Al. (Bignon et al., 2003) studied the effect of both macropores and strut pores on the growth of osteoblasts and fibroblasts. The size of the macro-interconnections affected the penetration of cells,

however cell migration occurred via emission of cytoplasmic extensions that attached to the microporosity. It is also important to observe that for both 3D-printed samples the open porosity was >90% of the total porosity. 3D-printing of these compositions therefore allows for the production of samples with both a microporosity in the struts and a designed macroporosity, which is easily tailored by the printing process.

*Figure 6* shows the flexibility of the 3D-printing system to produce different geometries from simple (*Figure 6 a-b*) to more complex ones (*Figure 6 c- d*).

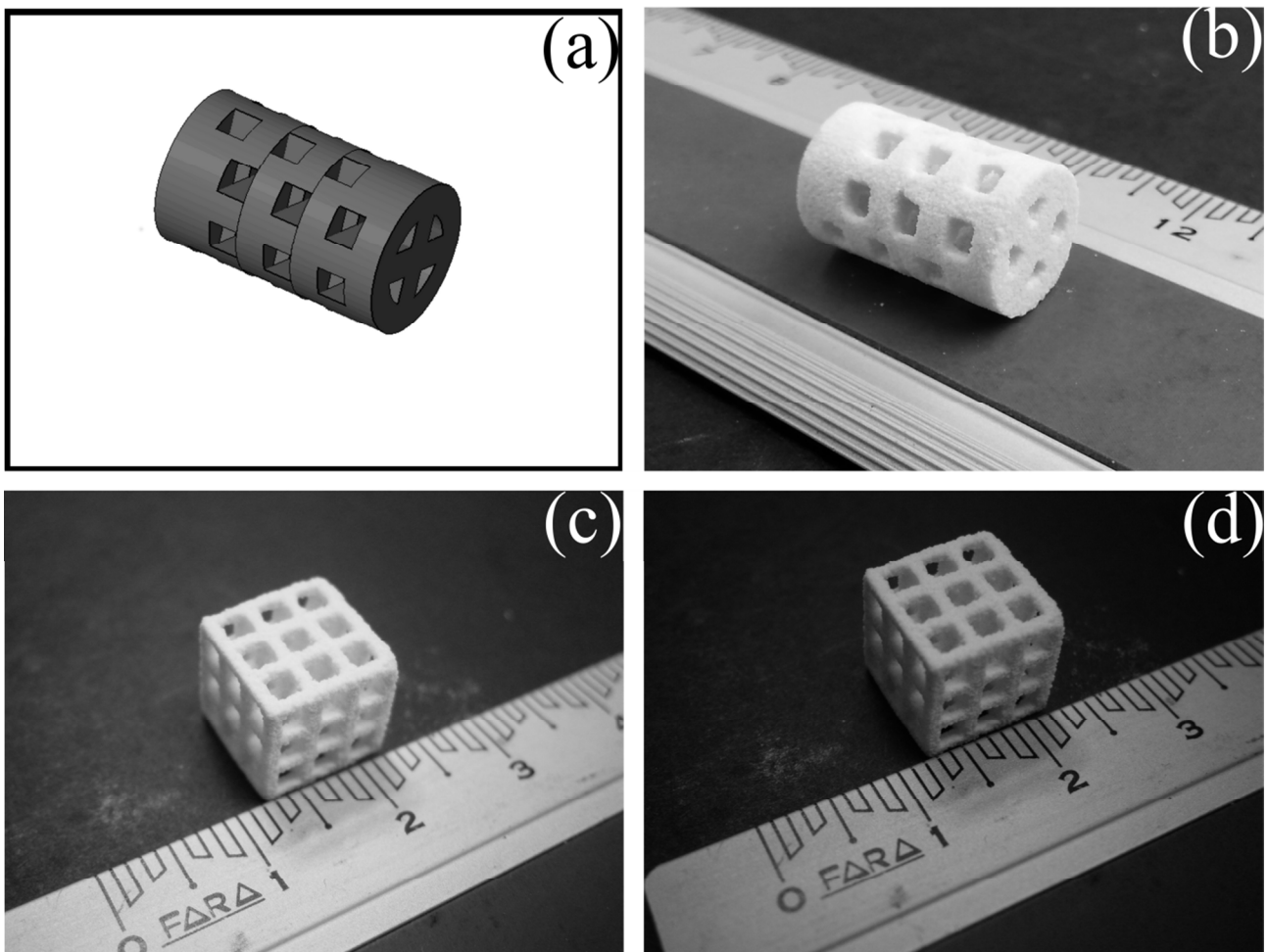


**Figure 6** Images of (a) CAD model of a cylindrical porous scaffold, (b) obtained HG 3D- printed scaffold from (a) and after heat treatment, (c) green body of an obtained HG cubic scaffold after 3D-printing and (d) cubic scaffold from (c) after heat treatment. HG = high amount of glass filler, LG = low amount of glass filler.

Obviously, the influence of porosity on both mechanical properties and resorbability of an implant has to be considered, whereas an increased porosity generally decreases the strength and increases the resorption rate.

### *XRD analysis*

The phase purity of samples HG and LG was also examined by means of XRD analysis on powders obtained by grinding 3D-printed samples after the heat treatment.

*Figure 7b* shows that for HG almost all peaks could be assigned to wollastonite-2M and hydroxylapatite ( $\text{Ca}_{10}(\text{PO}_4)_6(\text{OH})_2$ ) or fluorapatite ( $\text{Ca}_5(\text{PO}_4)_3\text{F}$ ), except for a minor amount of cristobalite. Hydroxylapatite and fluorapatite are not easy to separate since their peaks are in similar positions; it is possible that the sample contains both phases.

Both apatite phases were generated by the crystallization of the AP40 glass, while wollastonite derived both from the crystallization of AP40 and from the reaction between the residues coming from the preceramic polymer and the  $\text{CaCO}_3$  filler upon heat treatment. The presence of an expected amorphous phase (deriving from the AP40) could also be detected by observing the amorphous hump located at about  $30^\circ$  (which is highlighted by the baseline in red in the graph). In the case of HG, therefore, the possibility of achieving a high phase purity was demonstrated.

The presence of wollastonite and apatite was confirmed in LG as well (

*Figure 7a*). However the expected phase purity could not be confirmed in this case, since some peaks that could not be attributed either to wollastonite or to apatite were present. The correct phase identification is rather complex, due to the presence of multiple phases with superimposed peaks, but surely there are secondary phases of cristobalite and larnite, which is a dicalcium silicate ( $\text{C}_2\text{S} = \text{Ca}_2\text{SiO}_4$ ).

The formation of different silicates was consistent with what found in a previous work when using the same silicone resin and a micro-sized  $\text{CaCO}_3$  filler, which led to a non-optimal mixing (Bernardo et al., 2009). It was found that the formation in the shaped component during heating of regions richer in CaO and regions richer in  $\text{SiO}_2$  (from the preceramic polymer) would cause the formation of larnite and cristobalite secondary phases, respectively.

The formation of different silicates was consistent with what found in a previous work when using the same silicone resin and a micro-sized  $\text{CaCO}_3$  filler, which led to a non-optimal mixing (Bernardo et al., 2009). It was found that the formation in the shaped component during heating of regions richer in CaO and regions richer in  $\text{SiO}_2$  (from the preceramic polymer) would cause the formation of larnite and cristobalite secondary phases, respectively.

The formation of different silicates was consistent with what found in a previous work when using the same silicone resin and a micro-sized  $\text{CaCO}_3$  filler, which led to a non-optimal mixing (Bernardo et al., 2009). It was found that the formation in the shaped component during heating of regions richer in  $\text{CaO}$  and regions richer in  $\text{SiO}_2$  (from the preceramic polymer) would cause the formation of larnite and cristobalite secondary phases, respectively.

The formation of different silicates was consistent with what found in a previous work when using the same silicone resin and a micro-sized  $\text{CaCO}_3$  filler, which led to a non-optimal mixing (Bernardo et al., 2009). It was found that the formation in the shaped component during heating of regions richer in  $\text{CaO}$  and regions richer in  $\text{SiO}_2$  (from the preceramic polymer) would cause the formation of larnite and cristobalite secondary phases, respectively.

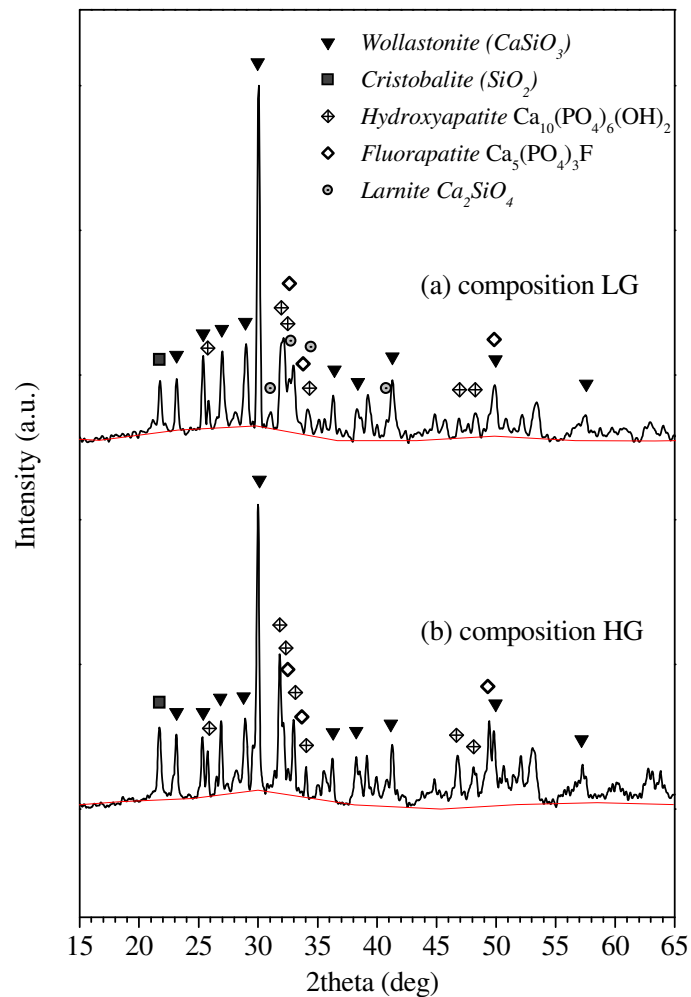


**Figure 7.** X-ray diffraction patterns of 3D-printed sample LG (a) and HG (b), after heat treatment at  $900^\circ\text{C}$ .

### ***In vitro assessment***

A preliminary viability test was performed in order to evaluate the cell proliferation and growth on ceramic discs of composition LG and HG. *Figure 8a* shows the results of the viability assessment of the two samples, *i.e.* HG and LG, at the different time points of 3, 7 and 14 days.

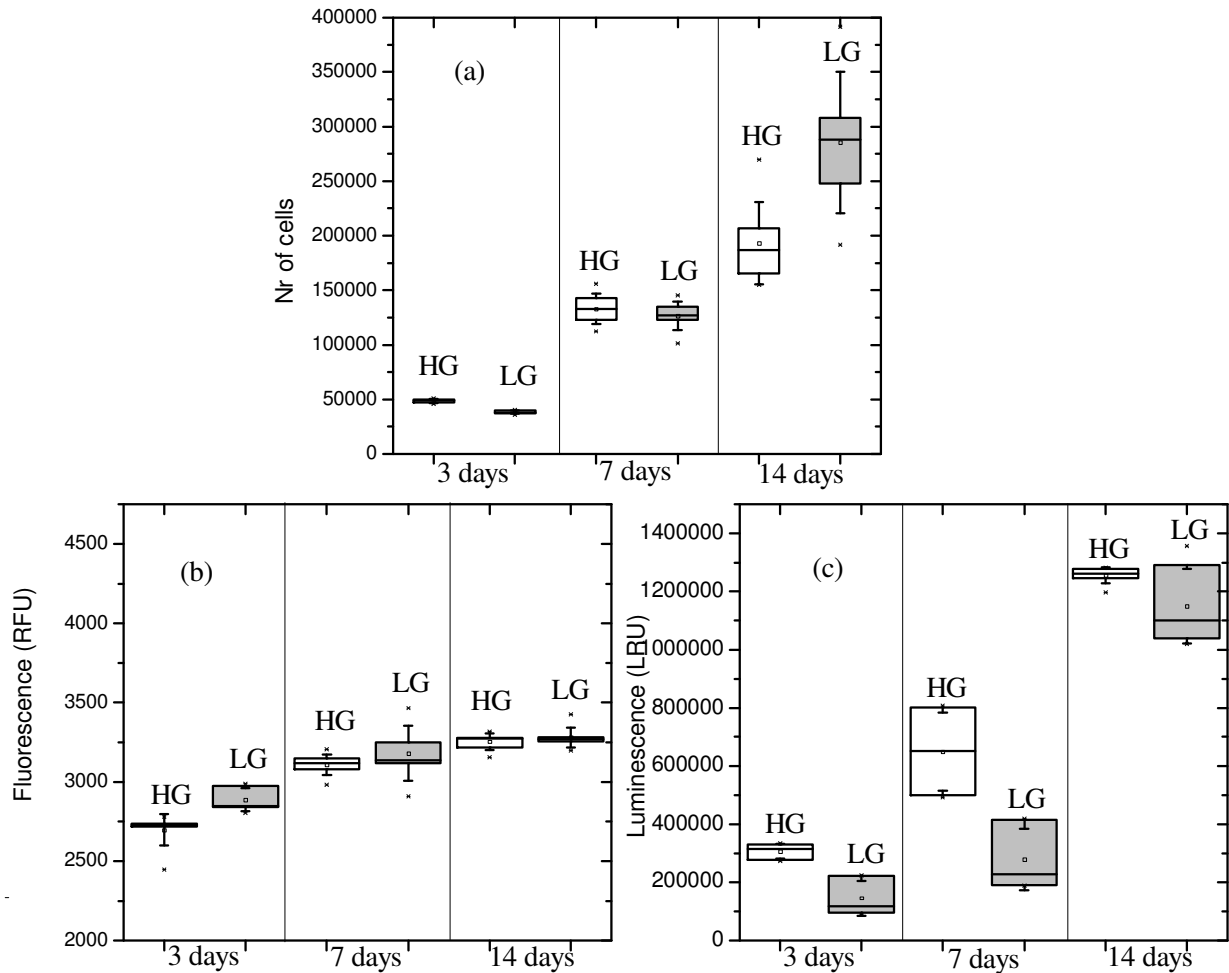


**Figure 8** Results of the *in vitro* assays performed on the HG and LG sintered discs with MC3T3 cells for 3, 7 and 14 days (a) cell viability, (b) cytotoxicity and (c) apoptotic behavior. Boxes show 25,50 and 75 percentiles and whiskers represent standard deviation. HG = high amount of glass filler, LG = low amount of glass filler.

After 3 days the number of cells was kept constant for HG, compared to the initial number of cells seeded; this value was significantly lower for LG ( $p = 1.06 \cdot 10^{-9}$ ). After 7 days the number of cells increased and there were no significant differences between HG and LG ( $p = 0.31$ ). At 14 days the difference on the number of cells between the two materials increased, being significantly higher for LG ( $p = 7.6 \cdot 10^{-4}$ ). In general, after 14 days the number of cells increased significantly on both materials compared to the initial seeding cell number.



The cytotoxicity assay (*Figure 8b*) seems in correlation with the viability assay as the results for LG at 3 days were significantly higher compared to HG. At 7 and 14 days the differences between the two materials were not significant. However, for all the materials and for all the time points the cytotoxicity was lower compared to the well plate with the CellTox Green dye in medium without cells, i.e. zero dead cells.. The lower cytotoxicity values to this zero dead cells value- indicated that the materials obtained by the preceramic polymer route, in combination with the 3D printing process, did not create a cytotoxic environment for the cells. The apoptotic assay (*Figure 8c*) presented a higher significant value for HG compared to LG after 3 and 7 days. At 14 days, there was no significant difference between the two samples ( $p = 0.04$ ). The ratio of the mean number of cells at a given time point divided by the Caspase activity remained similar.

The observations performed by the *in vitro* assessment were also confirmed by SEM observation (*Figure 9*).

At 3 days cells were present on both materials in a reduced number. After seven days a continuous layer of cells formed on the surface of the samples, indicating a good growth and spreading of the cells on the samples. After 14 days, the cells covered the whole surface of both materials.

Cells seeded on LG after 14 days exceeded significantly in number the cells seeded on HG.

The decrease in number of cells after 3 days for LG however may be related to a steep increase in pH which is usually observed during the dissolution of silicate ceramics in aqueous environment (Xiong et al., 2013).

For both samples the apoptotic assessment in combination with the viability and cytotoxicity assessment indicated that the materials allowed the cell to grow without causing an adverse reaction on them and that the long term behavior of 14 days tested here confirmed the absence of a cytotoxic effect from the materials on the cells over the 14 day period.

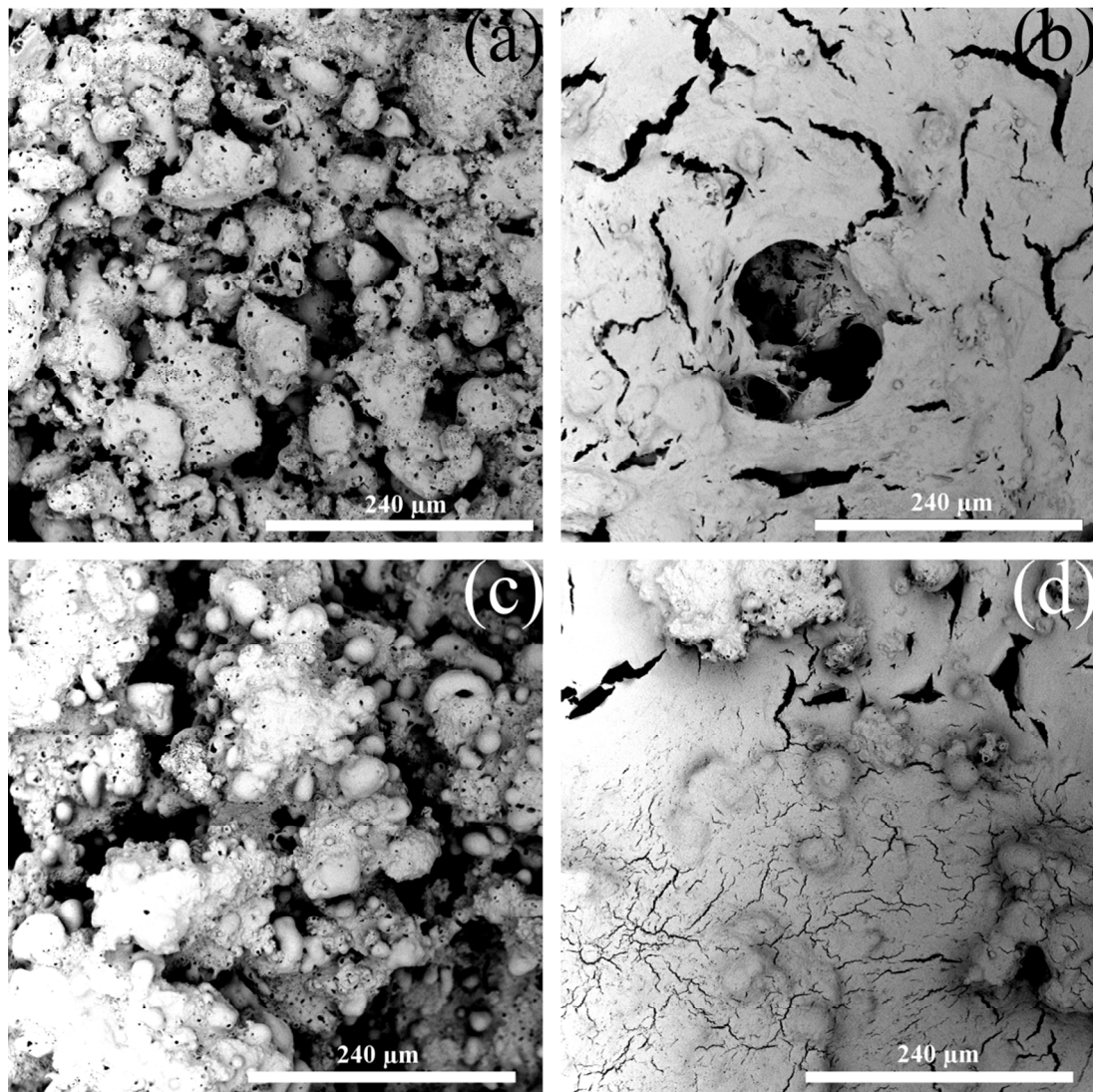


**Figure 9** Representative SEM images of MC3T3 cells seeded on sintered discs (a) 3 days on HG, (b) 14 days on HG, (c) 3 days on LG and (d) 14 days on LG. HG = high amount of glass filler, LG = low amount of glass filler.

## 2.2.3 AP40/hardystonite composites from preceramic polymer and fillers

### 2.2.3.1 Pressed samples

#### Materials and methods

Nano-sized ZnO (30 nm, Inframat® Advanced Materials, USA) was used as additional active filler to form hardystonite ( $\text{Ca}_2\text{ZnSi}_2\text{O}_7$ ). For the other materials and methods refer to paragraph 2.2.2.

## Results and discussion

Pure hardystonite ( $\text{Ca}_2\text{ZnSi}_2\text{O}_7$ ) could be synthesized by heat treatment of a mixture (formulation H1) of MK preceramic polymer and fillers ( $\text{CaCO}_3$ , nano- $\text{ZnO}$ ) at temperatures higher than  $1000^\circ\text{C}$ . The XRD patterns in *Figure 10* proved that hardystonite is developed already at  $1000^\circ\text{C}$  with some minor impurities of willemite ( $\text{ZnSiO}_4$ ); the purity of the hardystonite phase was increased at  $1200^\circ\text{C}$ , at which point the traces of willemite almost disappeared. A limited amount of willemite is anyways not particularly concerning since also this phase is a bioceramic and has good biological and mechanical properties (Zhang et al., 2010).

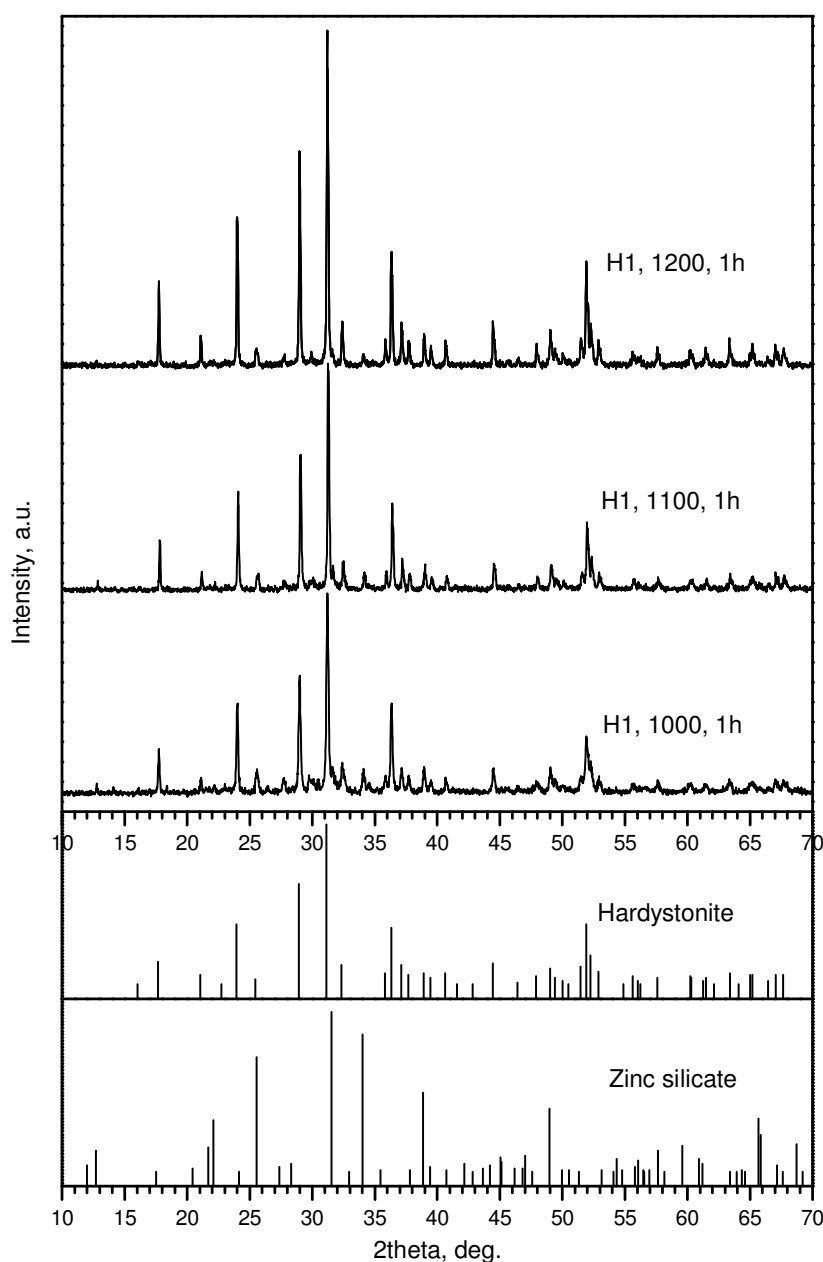


**Figure 10** XRD patterns of formulation H1 heat treated at  $1000^\circ\text{C}$ ,  $1100^\circ\text{C}$ ,  $1200^\circ\text{C}$  in air.

Similarly to the work done for the A/W composites, bioceramic compositions comprising a stoichiometric mixture of MK, CaCO<sub>3</sub> and ZnO to develop hardystonite and AP40 glass added as inert filler were investigated. Composition H4 in particular aimed at producing a material with 60wt% AP40 and 40wt% hardystonite (from preceramic + fillers) after heat treatment.

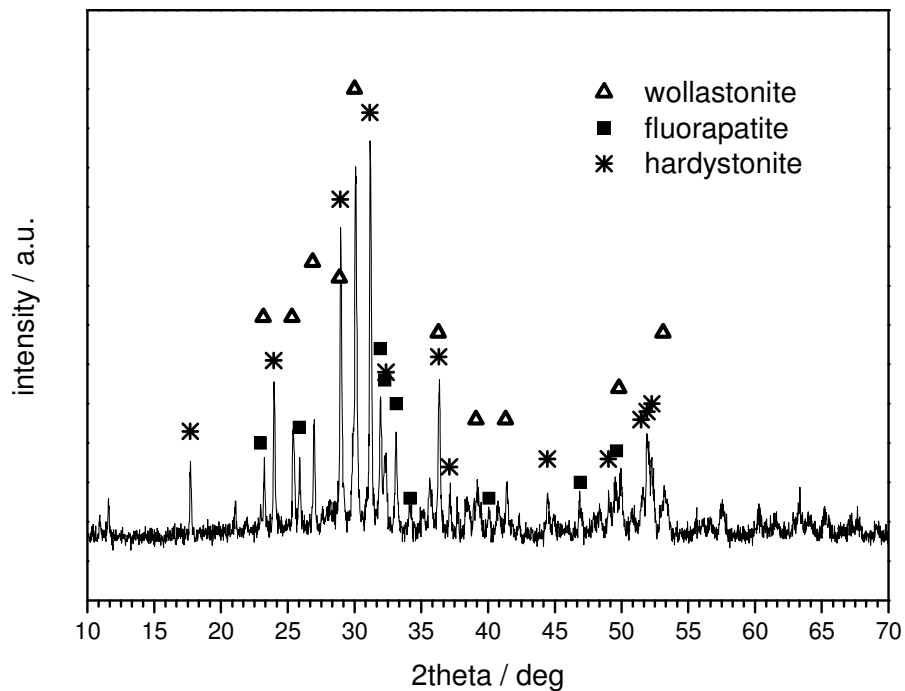


**Figure 11** XRD patterns of composition H4 heat treated in air at 1000°C

Figure 11 shows the XRD patterns for formulation H4 after heating at 1000°C. The data indicate that the phases developed were, as expected, hardystonite (from preceramic + fillers), wollastonite and fluorapatite (from crystallization of AP40). We could not confirm the presence of trace amounts of residual willemite, due to the overlap of the peaks relative to the various crystalline species. We could conclude that also in this case AP40 behaved as an inert filler and did not influence the reaction between MK and fillers, therefore tailored composite compositions can be easily produced.

## 2.3 Characterization and comparison of pressed and 3D-printed samples

### 2.3.1 Dissolution tests

#### *Materials and methods*

The dissolution was measured according to the DIN EN ISO 10993-14 standard, but applied to 3D-printed discs instead of granules. Discs with dimensions of 16 mm in diameter and 3 mm in thickness were produced and three samples were tested for each composition ( $n = 3$ ). Samples HG, LG and samples without AP40 were weighted (MC1 Research RC210P, Sartorius, Germany) before and after the dissolution test. Samples W and samples G were also tested for comparison. Here 3D-printed discs of type A were also produced by 3D-printing an AP40 powder with a commercial 3D-printer (RX-1, Prometal RCT GmbH, Germany) which makes use of a binder directly mixed with the printing liquid. An as-sieved AP40 powder in the range 45-90  $\mu\text{m}$  was used to achieve a good flowability.

Briefly, the samples were immersed in 20 mL of TRIS-HCl solution for each 1g of powder and the sample holder was left at 37 °C under a continuous circular movement. The pH was adjusted at pH = 7.4 by adding HCl to the TRIS buffer solution. The concentration of the single elements and the total dissolution were collected after 120 h (according to the normative) and then every week (168 h) for further 9 weeks. The solution was completely replenished after each measurement.

Samples were measured by ICP-OES (Optima 3000, Perkin-Elmer, USA). The dissolution was normalized by expressing it as mg of dissolved material divided by the weight of the sample.

The printed tablets weighed  $0.75 \pm 0.10$  g. The only exception was for tablets without W: these samples were lighter (0,5 g) because the thickness of the tablets had to be decreased in order to avoid cracking caused by the gas released during heat treatment.

#### **Results and discussion**

The dissolution results are presented in *Figure 12*. Here the total dissolution for 3D-printed compositions HG, LG, G and W is presented after ceramization.

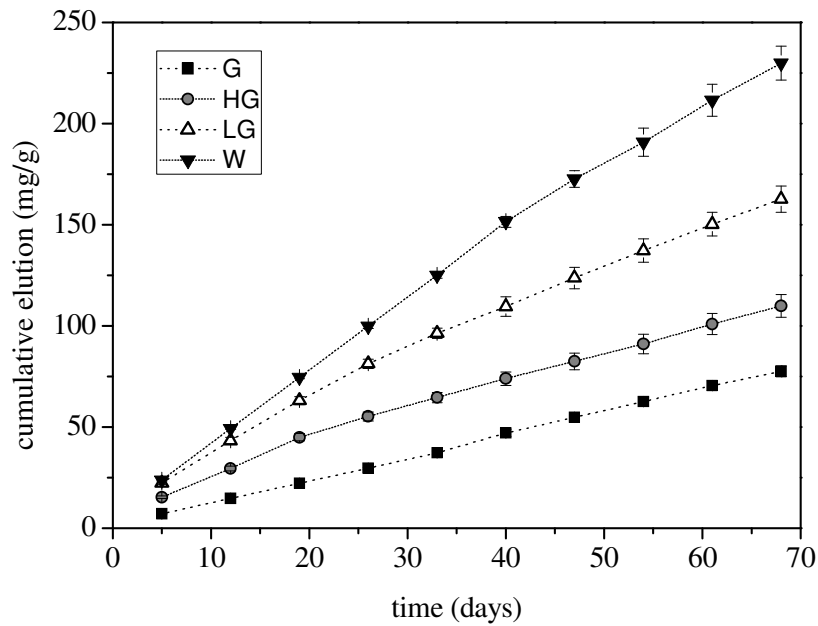


**Figure 12** Cumulative dissolution results for sintered samples. G= glass alone, HG = high amount of glass filler, LG = low amount of glass filler, W= no glass filler.

The total dissolution (*Figure 12*) at the first time point was in the range from  $7.2 \pm 0.2$  mg/g for sample A to  $23.8 \pm 0.3$  mg/g for sample W. Sample W, *i.e.* wollastonite, presented the highest dissolution rate, followed by LG, HG and A, respectively, after 68 days.

It is well known that wollastonite has the highest dissolution rate amongst the most studied silicate bioceramics, and that this rate is often considered excessive. Wang et al. (Wang et al., 2012) showed that wollastonite was osteostimulative, but lacked osteoconductivity due to its rapid degradation. After 10 weeks, W indeed lost more than 20 wt% of its mass, while G lost less than 10 wt%. Generally a high dissolution rate corresponds to a high pH increase which is also a concern for potential applications, because the ionic release in the solution causes alkalisation (Xiong et al., 2013). A limited rise in pH may be beneficial because a positive correlation between this increase and the proliferation of osteoblasts (Valerio et al., 2004) has been demonstrated; however, it is clear that a steep increase in pH is not beneficial to bone growth (Wu et al., 2007).

In our work, the dissolution rate was effectively controlled by controlling the AP40 glass filler amount in the composites content. AP40 had a moderate dissolution rate (as confirmed by the results in *Figure 12*, therefore its addition as filler allows the formation of bioceramic composites with an additional degree of freedom to regulate the dissolution rate by modifying the relative amount of the silicate phases (Ploska et al., 2004). The dissolution of LG and HG was indeed intermediate between the values obtained for W and for G.

Further studies are necessary in order to correlate the ions release and the results of the in-vitro tests. In particular, it would be useful to measure the concentration of ions during the in-vitro tests, since it is likely that their release in culture medium would be different from the release in TRIS-HCl buffer.

Another possible approach to regulate the dissolution of our bioceramic composites was to use different silicate phases. *Figure 13* shows the cumulative elution of pressed tablets of similar composition designed to give 60wt% AP40 after heat treatment; the difference was that the remaining 40wt% is given by hardystonite for sample H4 and by wollastonite for sample W4.

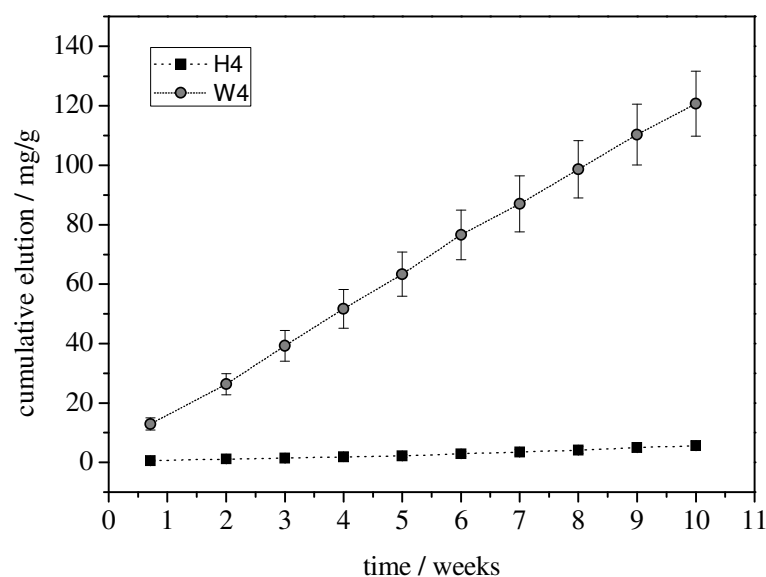


**Figure 13** Cumulative dissolution of pressed tablets of composition H4 and W4, as a function of the immersion time in a TRIS/HCl solution.

This results shows that clearly that sample W4 degraded very quickly compared to H4: after 10 weeks W4 lost about 12% of its original weight, while H4 only about 0.5%. This is consistent with results found in literature, compare with *Table 1*.

### 2.3.2 Physical and mechanical properties

#### Materials and methods

Biaxial flexural mechanical strength was measured using the ball on three balls (B3B) test (Zwick/Roell Z005, Germany), according to the method developed by Boerger et al. (Börger et al.,

2002). This method requires the knowledge of the Poisson coefficient of the tested material, therefore the coefficient of the ceramic mixtures was estimated with a rule of mixtures starting from the coefficients of the individual phases (A/W glass-ceramic (Kokubo et al., 1985), wollastonite (Demidenko and Stetsovskii, 2003), hardystonite (Haussühl and Liebertz, 2004)).

The porosity was taken into account by following three different models and averaging (Arnold et al., 1996) (Ramakrishnan and Arunachalam, 1993) (Roberts and Garboczi, 2000). A possible error of 5% on the maximum stress could be estimated (Börger et al., 2004). The calculated Weibull characteristic parameters are reported in *Table 5*.

The degree of densification of the processed samples was assessed by the Archimedes' method (ASTM373) and also by means of a gas helium pycnometer (Pycnomatic ATC, Porotec GmbH, Germany). At least 5 samples were tested for each formulation. Results are reported as mean  $\pm$  standard deviation.

## **Results and discussion**

The ball-on-three balls mechanical strength of printed HG-S tablets is reported in *Table 5*. Samples made of AP40 glass-ceramic were also produced for comparison by 3D-printing an AP40 powder (45-90  $\mu\text{m}$ ) with a commercial 3D-printer (RX-1, Prometal RCT GmbH, Germany).

Considering AP40 as our reference, sample G ( $< 25\mu\text{m}$ ) had a Weibull strength of about 45 MPa at 900°C, which was almost doubled at 1000°C. It was observed that even though the porosity at the two temperatures is similar ( $\approx 19\%$ ), the sample at 1000°C had a porosity finer and more homogeneously distributed compared to the sample at 900°C (Elsayed et al., 2014).

G (45-90  $\mu\text{m}$ ) had a larger particle size than G ( $< 25 \mu\text{m}$ ) and, as expected, this limited its densification during the sintering process, resulting in a porosity of  $\approx 29\%$  and a lower strength of 32 MPa. Composites HG had further lower strength ( $\approx 24$  MPa) due to the higher porosity of  $\approx 57\%$ . Concerning 3D-printed samples, we can state that HG tablets had a mechanical strength slightly lower than G tablets, considering that their Weibull strengths were 5.9 MPa and 7.9 MPa, respectively, but their porosity was almost 30% higher (64% and 50% respectively).

The absolute strength values measured were rather low, due to the high porosity present in the samples, making them suitable only for applications as non-load bearing biomaterial components. The mechanical strength could be improved by decreasing the particle size of the raw materials (AP40 in particular) and/or by optimizing the heat treatment in order to increase the density of the strut of the samples.

Pressed samples containing hardystonite and heat treated at 1000°C achieved a better densification compared to samples containing wollastonite (heat treated at 900°C). These samples had a quite



high mechanical strength of almost 67.6 MPa, which is in the range of the bending strength of cortical bone.

Sample	Heat treatment temperature (°C)	Notes	Weibull characteristic strength (MPa)	Weibull modulus	Total porosity (vol%)
G (<25µm)	900	Pressed	45.0	7.6	19.3±0.7
G (<25µm)	1000	Pressed	89.4	6.1	19.5±1.3
G (45-90µm)	900	Pressed	31.7	24.2	28.7±0.7
HG	900	Pressed	23.6	6.6	57.0±2.4
HG	900	3D-printed	5.9	6.6	63.8±0.7
G (45-90 µm)	900	3D-printed	7.9	3.7	49.3±1.4
H4	1000	Pressed	67.6	10.4	32.4±1.3

**Table 5.** Mechanical properties of 3D-printed tablets heat treated at 900°C.

Finally, a compressive strength of  $1.0\pm 0.3$  MPa (15 samples) was measured for the porous cylindrical scaffold in *Figure 6b*. These scaffolds had a total porosity of  $78\pm 1\%$  (measured geometrically) including both the designed macro-porosity and the porosity in the struts. The designed macro-porosity (calculated on the CAD drawing) was 37.9%; including in the model a porosity in the struts of 63.8% from *Table 5*, we estimated a total porosity of  $37.9\% \text{ (macro porosity)} + (100-37.9)\% \cdot 0.638 = 77.5\%$

which is similar to the geometrically measured density of our scaffolds, thus confirming our model.

## 2.4 Conclusions

Mixtures of a preceramic polymer and fillers were successfully shaped into complex porous scaffolds by means of powder-based three-dimensional printing. The ceramic parts produced after heat treatment consisted of wollastonite, produced by the reaction of  $\text{SiO}_2$  deriving from the preceramic polymer and  $\text{CaO}$  from  $\text{CaCO}_3$  added as an active filler, and apatite-wollastonite derived from a glass powder added as inert filler. Solubility tests performed in TRIS-HCl demonstrated that the solubility could be regulated by the addition of the apatite-wollastonite inert filler and that the total dissolution increased with the amount of wollastonite. Samples printed in the form of tablets were highly porous (up to 64% total porosity) and had a low biaxial flexural strength (~ 6 MPa). However the use of these raw materials allowed the shaping of complex porous scaffolds having a high porosity (almost 80%) comprising a designed ordered macro-porosity and micro-porosity in the struts.

Preliminary in vitro cell tests demonstrated that the materials were not cytotoxic and that cells grew well on their surface, forming an almost dense layer after two weeks. Future work will be focused on understanding the relationship between the release of ions from the material and their effect on cells growth and attachment.

## References

- Arnold, M., Boccaccini, A.R., Ondracek, G., 1996. Prediction of the Poisson's ratio of porous materials. *J. Mater. Sci.* 31, 1643–1646. doi:10.1007/BF00357876
- Bernardo, E., Colombo, P., Dainese, E., Lucchetta, G., Bariani, P.F., 2012. Novel 3D Wollastonite-Based Scaffolds from Pre ceramic Polymers Containing Micro- and Nano-Sized Reactive Particles. *Adv. Eng. Mater.* 14, 269–274. doi:10.1002/adem.201100241
- Bernardo, E., Tomasella, E., Colombo, P., 2009. Development of multiphase bioceramics from a filler-containing pre ceramic polymer. *Ceram. Int.* 35, 1415–1421. doi:10.1016/j.ceramint.2008.07.003
- Bignon, A., Chouteau, J., Chevalier, J., Fantozzi, G., Carret, J.-P., Chavassieux, P., Boivin, G., Melin, M., Hartmann, D., 2003. Effect of micro- and macroporosity of bone substitutes on their mechanical properties and cellular response. *J. Mater. Sci. Mater. Med.* 14, 1089–1097. doi:10.1023/B:JMSM.0000004006.90399.b4
- Bohner, M., Lemaître, J., 2009. Can bioactivity be tested in vitro with SBF solution? *Biomaterials* 30, 2175–2179. doi:10.1016/j.biomaterials.2009.01.008
- Börger, A., Supancic, P., Danzer, R., 2004. The ball on three balls test for strength testing of brittle discs: Part II: analysis of possible errors in the strength determination. *J. Eur. Ceram. Soc.* 24, 2917–2928. doi:10.1016/j.jeurceramsoc.2003.10.035
- Börger, A., Supancic, P., Danzer, R., 2002. The ball on three balls test for strength testing of brittle discs: stress distribution in the disc. *J. Eur. Ceram. Soc.* 22, 1425–1436. doi:10.1016/S0955-2219(01)00458-7
- Cai, S.X., Zhang, H.-Z., Guastella, J., Drewe, J., Yang, W., Weber, E., 2001. Design and synthesis of rhodamine 110 derivative and caspase-3 substrate for enzyme and cell-based fluorescent assay. *Bioorg. Med. Chem. Lett.* 11, 39–42.
- Chan, O., Coathup, M.J., Nesbitt, A., Ho, C.-Y., Hing, K.A., Buckland, T., Campion, C., Blunn, G.W., 2012. The effects of microporosity on osteoinduction of calcium phosphate bone graft substitute biomaterials. *Acta Biomater.* 8, 2788–2794. doi:10.1016/j.actbio.2012.03.038
- Chen, Q.Z., Wong, C.T., Lu, W.W., Cheung, K.M.C., Leong, J.C.Y., Luk, K.D.K., 2004. Strengthening mechanisms of bone bonding to crystalline hydroxyapatite in vivo. *Biomaterials* 25, 4243–4254. doi:10.1016/j.biomaterials.2003.11.017
- Demidenko, N.I., Stetsovskii, A.P., 2003. Correlation Between Elastic Properties of Wollastonite-Based Materials and Sintering Temperature. *Glass Ceram.* 60, 217–218. doi:10.1023/A:1027335124793
- El-Ghannam, A., Ducheyne, P., Shapiro, I.M., 1997. Formation of surface reaction products on bioactive glass and their effects on the expression of the osteoblastic phenotype and the deposition of mineralized extracellular matrix. *Biomaterials* 18, 295–303. doi:10.1016/S0142-9612(96)00059-2
- Elliott, J.C., 1994. Structure and chemistry of the apatites and other calcium orthophosphates. Elsevier, Amsterdam [The Netherlands], New York.
- Elsayed, H., Zocca, A., Bernardo, E., Gomes, C.M., Günster, J., Colombo, P., 2015. Development of bioactive silicate-based glass-ceramics from pre ceramic polymer and fillers. *J. Eur. Ceram. Soc.* 35, 731–739. doi:10.1016/j.jeurceramsoc.2014.09.020
- Elsayed, H., Zocca, A., Bernardo, E., Gomes, C.M., Günster, J., Colombo, P., 2014. Development of bioactive silicate-based glass-ceramics from pre ceramic polymer and fillers. *J. Eur. Ceram. Soc.* under review.
- Endo, T., Sugiura, S., Sakamaki, M., Takizawa, H., Shimada, M., 1994. Sintering and mechanical properties of  $\beta$ -wollastonite. *J. Mater. Sci.* 29, 1501–1506. doi:10.1007/BF00368916
- Hamadouche, M., Sedel, L., 2000. Ceramics in orthopaedics. *J. BONE Jt. Surg.-Br. Vol.-* 82, 1095–1099.
- Hausner, H.H., 1981. Powder characteristics and their effect on powder processing. *Powder Technol.* 30, 3–8. doi:10.1016/0032-5910(81)85021-8

- Hausühl, S., Liebertz, J., 2004. Elastic and thermoelastic properties of synthetic Ca<sub>2</sub>MgSi<sub>2</sub>O<sub>7</sub> (åkermanite) and Ca<sub>2</sub>ZnSi<sub>2</sub>O<sub>7</sub> (hardystonite). *Phys. Chem. Miner.* 31, 565–567. doi:10.1007/s00269-004-0416-9
- Hench, L.L., 2009. Genetic design of bioactive glass. *J. Eur. Ceram. Soc.* 29, 1257–1265.
- Hench, L.L., 1991. Bioceramics: From Concept to Clinic. *J. Am. Ceram. Soc.* 74, 1487–1510. doi:10.1111/j.1151-2916.1991.tb07132.x
- Hench, L.L., Paschall, H.A., 1973. Direct chemical bond of bioactive glass-ceramic materials to bone and muscle. *J. Biomed. Mater. Res.* 7, 25–42. doi:10.1002/jbm.820070304
- Hu, S., Ning, C., Zhou, Y., Chen, L., Lin, K., Chang, J., 2011. Antibacterial activity of silicate bioceramics. *J. Wuhan Univ. Technol.-Mater Sci Ed* 26, 226–230. doi:10.1007/s11595-011-0202-8
- Jarcho, M., 1981. Calcium phosphate ceramics as hard tissue prosthetics. *Clin. Orthop.* 259–278.
- Karageorgiou, V., Kaplan, D., 2005. Porosity of 3D biomaterial scaffolds and osteogenesis. *Biomaterials* 26, 5474–5491. doi:10.1016/j.biomaterials.2005.02.002
- Kitsugi, T., Nakamura, T., Yamamura, T., Kokubu, T., Shibuya, T., Takagi, M., 1987. SEM-EPMA observation of three types of apatite-containing glass-ceramics implanted in bone: The variance of a Ca-P-rich layer. *J. Biomed. Mater. Res.* 21, 1255–1271. doi:10.1002/jbm.820211008
- Kokubo, T., Ito, S., Shigematsu, M., Sakka, S., Yamamuro, T., 1985. Mechanical properties of a new type of apatite-containing glass-ceramic for prosthetic application. *J. Mater. Sci.* 20, 2001–2004. doi:10.1007/BF01112282
- Kokubo, T., Takadama, H., 2006. How useful is SBF in predicting in vivo bone bioactivity? *Biomaterials* 27, 2907–2915. doi:10.1016/j.biomaterials.2006.01.017
- Likitvanichkul, S., Lacourse, W.C., 1998. Apatite–wollastonite glass-ceramics part I Crystallization kinetics by differential thermal analysis. *J. Mater. Sci.* 33, 5901–5904. doi:10.1023/A:1004491107420
- Lin, K., Zhai, W., Ni, S., Chang, J., Zeng, Y., Qian, W., 2005. Study of the mechanical property and in vitro biocompatibility of CaSiO<sub>3</sub> ceramics. *Ceram. Int.* 31, 323–326. doi:10.1016/j.ceramint.2004.05.023
- Long, L.H., Chen, L.D., Bai, S.Q., Chang, J., Lin, K.L., 2006. Preparation of dense β-CaSiO<sub>3</sub> ceramic with high mechanical strength and HAp formation ability in simulated body fluid. *J. Eur. Ceram. Soc.* 26, 1701–1706. doi:10.1016/j.jeurceramsoc.2005.03.247
- Maeno, S., Niki, Y., Matsumoto, H., Morioka, H., Yatabe, T., Funayama, A., Toyama, Y., Taguchi, T., Tanaka, J., 2005. The effect of calcium ion concentration on osteoblast viability, proliferation and differentiation in monolayer and 3D culture. *Biomaterials* 26, 4847–4855. doi:10.1016/j.biomaterials.2005.01.006
- Nase, S.T., Vargas, W.L., Abatan, A.A., McCarthy, J.J., 2001. Discrete characterization tools for cohesive granular material. *Powder Technol.* 116, 214–223. doi:10.1016/S0032-5910(00)00398-3
- Pérez, J.M., Teixeira, S.R., Rincón, J.M., Romero, M., 2012. Understanding the Crystallization Mechanism of a Wollastonite Base Glass Using Isoconversional, IKP Methods and Master Plots. *J. Am. Ceram. Soc.* 95, 3441–3447. doi:10.1111/j.1151-2916.2012.05415.x
- Picker, H., Arps, H., Köhler, S., Berger, G., 1993. Ceramic bone replacement materials. *Zahnärztl Implant.* 9, 111–116.
- Ploska, U., Berger, G., Sahre, M., 2004. Investigation of the Influence of Zirconium Content on the Formation of Apatite on Bioactive Glass-Ceramics. *Key Eng. Mater.* 254-256, 71–74. doi:10.4028/www.scientific.net/KEM.254-256.71
- Ramakrishnan, N., Arunachalam, V.S., 1993. Effective Elastic Moduli of Porous Ceramic Materials. *J. Am. Ceram. Soc.* 76, 2745–2752. doi:10.1111/j.1151-2916.1993.tb04011.x
- Ratner, B.D., 2004. *Biomaterials science: an introduction to materials in medicine.* Academic press.

- Reichelt, H., Köhler, S., Berger, G., Draffehn, J., Madry, C., Krenz, M., Wichner, H., 1986. [Peri-implant enzyme activities and mineralization in bone tissue after implantation of bioactive vitroceramics--a method for biomaterial testing of hard-tissue substitutes. 1. Establishment and representation of the method]. *Z. Exp. Chir. Transplant. Kunstliche Organe Organ Sect. Exp. Chir. Ges. Chir. DDR* 20, 67–74.
- Roberts, A.P., Garboczi, E.J., 2000. Elastic Properties of Model Porous Ceramics. *J. Am. Ceram. Soc.* 83, 3041–3048. doi:10.1111/j.1151-2916.2000.tb01680.x
- Schumacher, T.C., Volkmann, E., Yilmaz, R., Wolf, A., Treccani, L., Rezwani, K., 2014. Mechanical evaluation of calcium-zirconium-silicate (baghdadite) obtained by a direct solid-state synthesis route. *J. Mech. Behav. Biomed. Mater.* 34, 294–301. doi:10.1016/j.jmbbm.2014.02.021
- Shimazaki, K., Mooney, V., 1985. Comparative study of porous hydroxyapatite and tricalcium phosphate as bone substitute. *J. Orthop. Res.* 3, 301–310. doi:10.1002/jor.1100030306
- Valerio, P., Pereira, M.M., Goes, A.M., Leite, M.F., 2004. The effect of ionic products from bioactive glass dissolution on osteoblast proliferation and collagen production. *Biomaterials* 25, 2941–2948. doi:10.1016/j.biomaterials.2003.09.086
- Walsh, W.R., Morberg, P., Yu, Y., Yang, J.L., Haggard, W., Sheath, P.C., Svehla, M., Bruce, W.J.M., 2003. Response of a calcium sulfate bone graft substitute in a confined cancellous defect. *Clin. Orthop.* 228–236. doi:10.1097/01.blo.0000030062.92399.6a
- Wang, C., Xue, Y., Lin, K., Lu, J., Chang, J., Sun, J., 2012. The enhancement of bone regeneration by a combination of osteoconductivity and osteostimulation using  $\beta$ -CaSiO<sub>3</sub>/ $\beta$ -Ca<sub>3</sub>(PO<sub>4</sub>)<sub>2</sub> composite bioceramics. *Acta Biomater.* 8, 350–360. doi:10.1016/j.actbio.2011.08.019
- Woo, S.L., Akeson, W.H., Coutts, R.D., Rutherford, L., Doty, D., Jemmott, G.F., Amiel, D., 1976. A comparison of cortical bone atrophy secondary to fixation with plates with large differences in bending stiffness. *J. Bone Joint Surg. Am.* 58, 190–195.
- Wu, C., Chang, J., 2013. A review of bioactive silicate ceramics. *Biomed. Mater.* 8, 032001. doi:10.1088/1748-6041/8/3/032001
- Wu, C., Chang, J., Zhai, W., 2005. A novel hardystonite bioceramic: preparation and characteristics. *Ceram. Int.* 31, 27–31. doi:10.1016/j.ceramint.2004.02.008
- Wu, C., Ramaswamy, Y., Kwik, D., Zreiqat, H., 2007. The effect of strontium incorporation into CaSiO<sub>3</sub> ceramics on their physical and biological properties. *Biomaterials* 28, 3171–3181. doi:10.1016/j.biomaterials.2007.04.002
- Xiong, K., Shi, H., Liu, J., Shen, Z., Li, H., Ye, J., 2013. Control of the Dissolution of Ca and Si Ions from CaSiO<sub>3</sub> Bioceramic via Tailoring Its Surface Structure and Chemical Composition. *J. Am. Ceram. Soc.* 96, 691–696. doi:10.1111/jace.12168
- Xynos, I.D., Edgar, A.J., Buttery, L.D.K., Hench, L.L., Polak, J.M., 2001. Gene-expression profiling of human osteoblasts following treatment with the ionic products of Bioglass® 45S5 dissolution. *J. Biomed. Mater. Res.* 55, 151–157. doi:10.1002/1097-4636(200105)55:2<151::AID-JBM1001>3.0.CO;2-D
- Xynos, I.D., Hukkanen, M.V.J., Batten, J.J., Buttery, L.D., Hench, L.L., Polak, J.M., 2000. Bioglass® 45S5 Stimulates Osteoblast Turnover and Enhances Bone Formation In Vitro: Implications and Applications for Bone Tissue Engineering. *Calcif. Tissue Int.* 67, 321–329. doi:10.1007/s002230001134
- Zhai, W., Lu, H., Chen, L., Lin, X., Huang, Y., Dai, K., Naoki, K., Chen, G., Chang, J., 2012. Silicate bioceramics induce angiogenesis during bone regeneration. *Acta Biomater.* 8, 341–349. doi:10.1016/j.actbio.2011.09.008
- Zhang, M., Lin, K., Chang, J., 2012. Preparation and characterization of Sr-hardystonite (Sr<sub>2</sub>ZnSi<sub>2</sub>O<sub>7</sub>) for bone repair applications. *Mater. Sci. Eng. C* 32, 184–188. doi:10.1016/j.msec.2011.10.017
- Zhang, M., Zhai, W., Chang, J., 2010. Preparation and characterization of a novel willemite bioceramic. *J. Mater. Sci. Mater. Med.* 21, 1169–1173. doi:10.1007/s10856-010-3985-9

Zocca, A., Gomes, C.M., Mühler, T., Günster, J., 2014. Powder-Bed Stabilization for Powder-Based Additive Manufacturing. *Adv. Mech. Eng.* 2014.

Zocca, A., Gomes, C.M., Staude, A., Bernardo, E., Günster, J., Colombo, P., 2013. SiOC ceramics with ordered porosity by 3D-printing of a preceramic polymer. *J. Mater. Res.* 28, 2243–2252. doi:10.1557/jmr.2013.129

## CHAPTER 3

## CHAPTER 3

### Bioceramic scaffolds produced by extrusion-based 3D-printing of preceramic polymers and fillers

The aim of this work was the extrusion-based 3D-printing, also indicated as direct ink writing (DIW), of pastes containing a preceramic polymer and filler, in order to produce hardystonite scaffolds.

#### 3.1 Materials and methods

##### 3.1.1 3D-printer

The extrusion-based 3D-printer used in this work of thesis is a “Powerwasp Evo” (see *Figure 1*) model by “Wasp Project” (Italy).

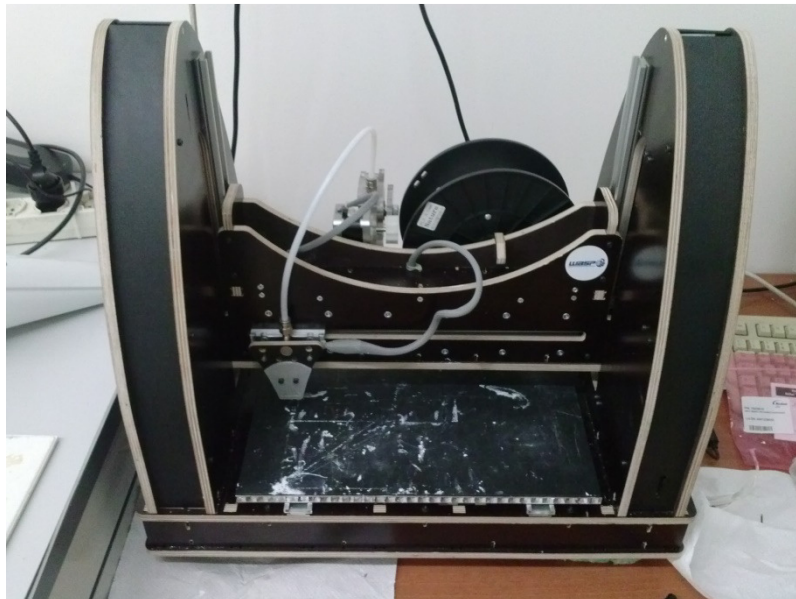


*Figure 1* Powerwasp Evo 3D-printer

This 3D-printer has been modified in collaboration with “Wasp” in order to implement a syringe paste extruder in place of the standard filament extruder for the fused deposition modelling.

The equipment used is depicted in *Figure 2*.



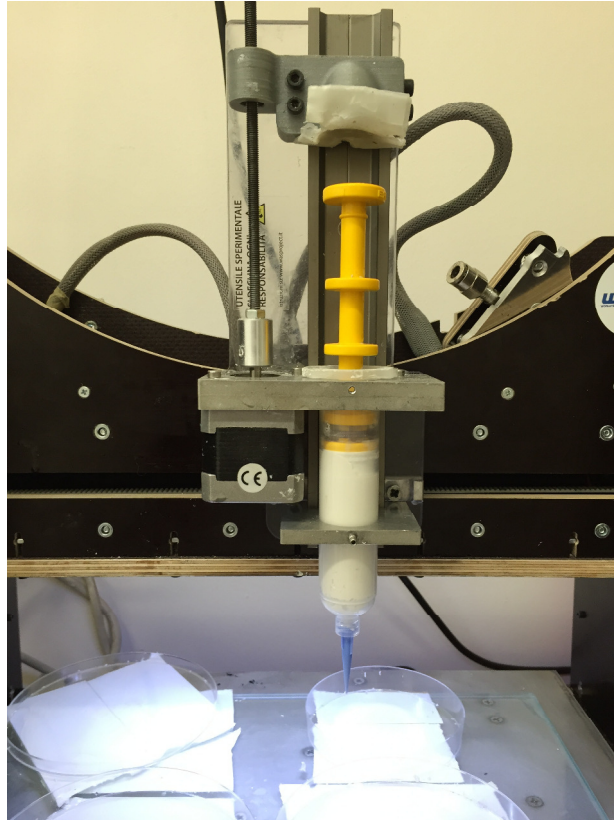


*Figure 2 Syringe and extruder supports.*

The ceramic paste is carefully loaded in the syringe barrel. The motor drives the screw on the left of *Figure 2*, and the head on the top pushes the plunger thus extruding the material through the nozzle.

### **3.1.2 Ink preparation**

ZnO (Sigma Aldrich, Germany) and CaCO<sub>3</sub> (Bitossi, Italy) were mixed as a ceramic powder, while SiO<sub>2</sub> was added to the system mainly through decomposition of the preceramic polymer (MK, see chapters 1 and 2).

The possibility of partially substituting the preceramic polymer with an additional source of SiO<sub>2</sub> has also been explored. Fumed silica (FS, Aerosil R106, Evonik, Germany) was used for the purpose of modifying the rheological properties of the paste; FS is known to be a thickening and thixotropic agent in low molecular weight solvents (Raghavan and Khan, 1995) (Paquien et al., 2005).

Obtaining a homogeneous mixture is essential for two reasons: (i) to achieve a complete reaction to form hardystonite (ii) to avoid agglomerates in the ink, which would clog the syringe nozzle during extrusion.

For this reason, the use of a laboratory mixer, employed in a first part of the work, was abandoned in favour of a mixing by intensive ball milling of the ink.

The ink was prepared as follows:

- 1) FS was dispersed in isopropanol until achievement of a thick gel;
- 2) the preceramic polymer was gently dissolved in the dispersion; the suspension was ball milled in a planetary mill for 1h at 200 rpm in an alumina jar with alumina balls (diameter  $\approx$  1cm);
- 3) The ceramic fillers were added and the ink was again ball milled for 5 hours at 400 rpm.

Two compositions were investigated, H0 and HF which are reported in *Table 1*. HF is similar to H0 as both are designed to give hardystonite upon heat treatment; however, HF contains some hardystonite filler already in the ink. Since bio-grade hardystonite powder was not available commercially, it was prepared by the preceramic polymer approach. This is a cheaper and easier alternative to obtain hardystonite powder compared to the sol-gel route which is usually employed in literature (Zhang et al., 2012).

<b>Composition (wt%)</b>	<b>Isopropyl alcohol</b>	<b>Fumed silica</b>	<b>MK</b>	<b>ZnO</b>	<b>CaCO<sub>3</sub></b>	<b>Hardystonite filler</b>	<b>Density (g/cm<sup>3</sup>)</b>
H0	13.5	2.5	26.4	16.7	41.0	0	2.61
HF	12.1	1.9	20.3	12.8	31.6	21.2	2.74

*Table 1 weight composition of inks H0 and HF*

After preliminary tests an appropriate amount of fumed silica was established as 10 wt% for both H0 and HF, expressed as the fraction of FS over the total amount of SiO<sub>2</sub> obtained after ceramization.

### **3.1.3 Rheological characterization**

Viscosity measurements were performed using a rotational viscometer (MCR302, Anton Paar, Austria) using a plate-plate geometry with a plate diameter of 50 mm suitable for highly viscous fluids and a gap of 1 mm. A solvent trap was used to prevent quick evaporation of the isopropanol.

Three types of test were performed: 1) flow curve increasing linearly the shear rate from  $0.1 \text{ s}^{-1}$  to  $100 \text{ s}^{-1}$ , 2) strain sweep in oscillatory mode test at a frequency of 1 Hz, increasing the strain from 0.001% to 100%, 3) relaxation test, applying at first a shear rate of  $50 \text{ s}^{-1}$  for 30s, followed by an application of a controlled shear stress of 25 Pa for 90 s in order to measure the recovery of viscosity.

### 3.1.4 Direct ink writing of hardystonite 3D scaffolds

A commercial fused deposition modelling printer for polymeric materials (Powerwasp Evo, Wasp, Italy) was modified in order to implement a syringe extruder. Conical nozzles of various sizes (Nordson Italia S.p.a., Italy) were mounted on the syringe. A nozzle with a diameter of 0.41 mm was used in the following experiments unless otherwise specified.

The ink was printed in a non-wetting oil bath in order to prevent clogging due to solvent evaporation, which is a common problem when extruding through fine nozzles.

Scaffolds with dimensions  $15 \times 5 \times 5 \text{ mm}^3$  were printed, following the geometry schematized in *Figure 3*. The spanning  $L$  between the centre of two contiguous filaments was 1 mm and the diameter  $d$  was 0.35 mm in average, measured by optical microscopy.

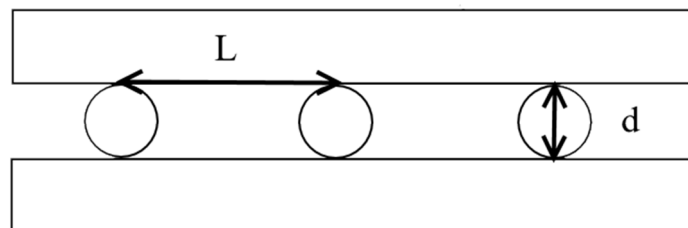


**Figure 3** Geometry of the extrusion-printed scaffolds

The produced scaffolds were heat treated following this schedule:

Room temperature ( $1^\circ\text{C}/\text{min}$ )  $\rightarrow$   $450^\circ\text{C}$  ( $0.5^\circ\text{C}/\text{min}$ )  $\rightarrow$   $500^\circ\text{C}$  (1h) ( $0.5^\circ\text{C}/\text{min}$ )  $\rightarrow$   $600^\circ\text{C}$  (3h) ( $0.5^\circ\text{C}/\text{min}$ )  $\rightarrow$   $900^\circ\text{C}$  ( $1^\circ\text{C}/\text{min}$ )  $\rightarrow$   $1200^\circ\text{C}$  (1h)  $\rightarrow$  ( $5^\circ\text{C}/\text{min}$ ) room temperature.

### 3.1.5 Phase composition characterization

The phase composition of powdered filaments heat treated at 1200°C was examined by X-ray diffractometry (XRD) (D8 Advance, Bruker, Germany). The composition of the ceramized materials was determined by X-ray fluorescence (S4 Pioneer, Bruker AXS GmbH, Germany).

### 3.1.6 Mechanical testing and physical characterization

The dimensions of the scaffolds were measured by means of a digital caliper, before and after the heat treatment, thus allowing the calculation of the ceramization shrinkage. The crushing strength of the ceramized scaffolds was measured at room temperature using an Instron 1121 UTM (Instron Danvers, USA) at cross-head speed of 0.5 mm/min. A compliant layer (Parafilm M, Pechiney Plastic Packaging, USA) was used between the plates and the sample surfaces. At least ten samples were measured for each composition and the results are reported as mean  $\pm$  standard deviation.

The morphology of the scaffolds was investigated by scanning electron microscopy (SEM, FEI Quanta 200 ESEM, The Netherlands). The porosity in the struts of the scaffold was evaluated using an image processing software (Image J, <http://imagej.net/>), which transforms the image in a black and white format according to a greyscale threshold value and counts the number of black and white pixels.

## 3.2 Results and discussion

### 3.2.1 Rheological characterization

The rheological properties of the paste are crucial for the replication of unsupported geometries, because the material has to bear its own weight with minimal deformation.

(Smay et al., 2002) and (Schlordtil and Greil, 2012) determined the conditions for stability of a spanning filament. Based on a static beam model, (Smay et al., 2002) determined that in order to have a minimal deflection ( $< 0.05$  times the diameter of the filament) the following equation must be respected:

$$G' \geq 1.4 \gamma \left(\frac{L}{D}\right)^4 D$$

*Eq. 1*

Where

$G'$  is the shear storage modulus of the paste

$\gamma$  is the specific weight of the paste

$L$  is the spanning distance (distance between two points supporting the filament)

$D$  is the diameter of the filament

Our aim was to produce scaffolds with a filament diameter of  $\approx 0.5$  mm and a spanning of 1 mm.

The paste used in our work had a density  $\rho = 1.69$  g/cm<sup>3</sup> for H0 and  $\rho = 1.82$  g/cm<sup>3</sup> for HF, which corresponds to a specific weight of  $1.66 \cdot 10^4$  N/m<sup>3</sup> and  $1.85 \cdot 10^4$  N/m<sup>3</sup>, respectively.

With these values, *Eq. 1* gives  $G' \geq 542$  Pa for H0 and 604 Pa for HF. (Schlordtil and Greil, 2012) calculated a value of  $G' \geq 270$  kPa for a similar geometry, but they erroneously overestimated the result because they used the density of the ink instead of its specific weight in the calculations. In the same reference, however, a model was used to describe dynamically the deformation of the beam, giving the following equation for the midspan deflection:

$$z(t) \sim \frac{1}{2} \sqrt{L(t)^2 - L_0^2}$$

**Eq. 2**

$z(t)$  = time dependent midspan deflection

$L(t)$  = time dependent length of the beam

$L_0$  = initial length of the beam

$$L(t) = L_0 \left( 1 + \int_0^t \frac{\rho \cdot g \cdot L_0}{6\eta(t)} dt \right)$$

**Eq. 3**

$\rho$  = density of the paste

$g$  = gravitation constant (9.81 m/s<sup>2</sup>)

$\eta(t)$  = time dependent viscosity

$\eta(t)$  has a major role in this equation since it is the only time dependent variable: in an optimized system, the material is extruded at high shear rate and at low viscosity; once it is deposited, its viscosity should rapidly increase (recover) to minimize the deflection  $z(t)$ .

Eq. 3 was slightly modified in order to take into account also the Archimedean force due to the fact that the filament is immersed in oil. For this reason, the density value  $\rho$  was substituted with  $\rho - \rho(\text{oil})$ , where  $\rho(\text{oil})$  is the density of the oil.

### 3.2.1.1 Dynamic oscillation test

This test was performed in oscillatory mode at a frequency of 1 Hz. The paste was sheared with a deformation ramp from 0.01 % to 100 %. Figure 4 shows a log-log plot of the storage modulus of the paste as a function of the shear stress.

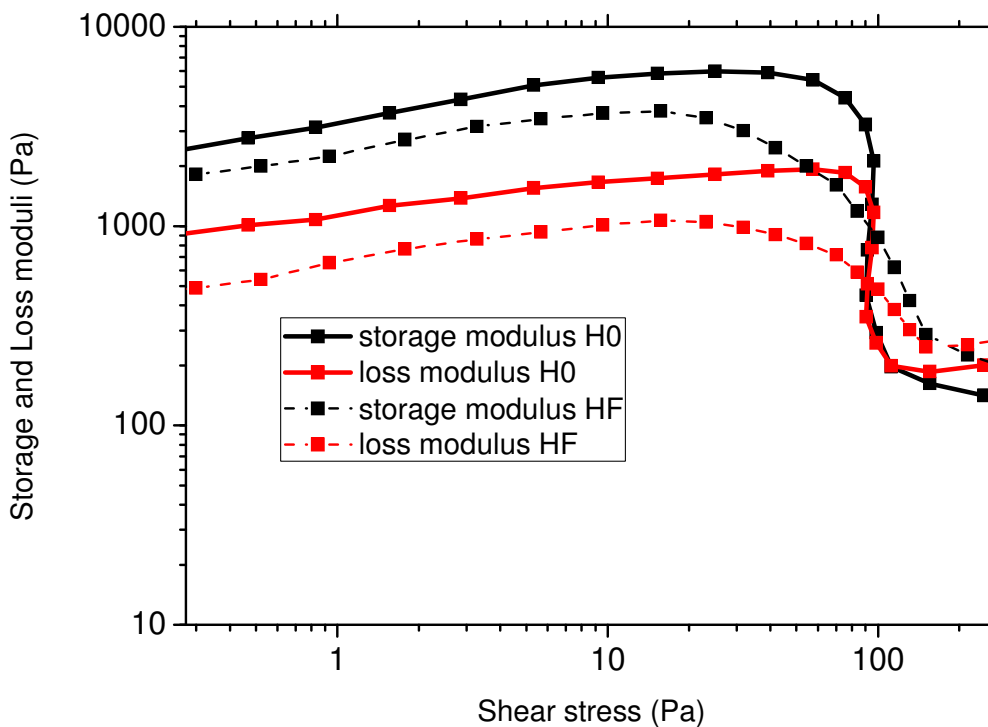


**Figure 4** logarithmic plot of the storage modulus of the paste as a function of the shear stress applied at 1 Hz.

The material had a gel-like behaviour with a distinct plateau at low shear stress, which corresponds to a yield stress  $\tau_y$ . At higher values of shear stress the storage modulus steeply decreased, which can be interpreted by a gradual destruction of the microstructural arrangement of the material.

In the plateau region  $G'$  had a value of  $G'(\text{eq}) \approx 6.0$  kPa and  $\tau_y$  calculated at the point  $G' = 0.9 G'(\text{eq})$  was  $\tau_y = 58$  Pa for H0. HF had slightly lower values  $G'(\text{eq}) \approx 3.8$  kPa and  $\tau_y = 25$  Pa, which indicated the behaviour of a weaker gel.

It can be noticed that in the literature stronger gels have been used.  $G'(\text{eq})$  was in the range 10-100 kPa for inks developed by (Smay et al., 2002), while (Schlordtil and Greil, 2012) developed inks with  $G'(\text{eq})$  up to 390 kPa. However, it is relevant that our result was still superior to the limit determined by *Eq. 1*.

### 3.2.1.2 Steady rate sweep

In this test, the shear rate was gradually increased from 0.1 to 100  $\text{s}^{-1}$  and the corresponding shear stress was measured. The material during extrusion is sheared with a shear rate which can be calculated by *Eq. 4*:

$$\gamma' = \frac{4Q}{\pi r^3}$$

***Eq. 4***

Q= volumetric flow rate

r = nozzle radius

which in our experiments gave a value of about 100  $\text{s}^{-1}$ .

*Figure 5* shows the experimental curves for inks H0 and HF. Both inks had a high apparent viscosity in the order of  $10^3$  Pa·s at low shear rate (0.1  $\text{s}^{-1}$ ) while this value decreased by two orders of magnitude when the shear rate increased to 100  $\text{s}^{-1}$ . This behaviour is typical of shear thinning fluids. For H0, the curves plotted in double logarithmic scale had an almost linear trend, which suggests that they follow a power-law model with yield stress, such as in (Herschel and Bulkley, 1926). The curves for HF were similar, even though these lines seem to be fragmented in two segments with different slopes, which complicates the interpretation.

This might be related to experimental errors, since it was noticed that the material tended to be expelled through the external side of the plates of the instrument. This effect probably also caused the irregularities and humps in the curve at high shear stresses.

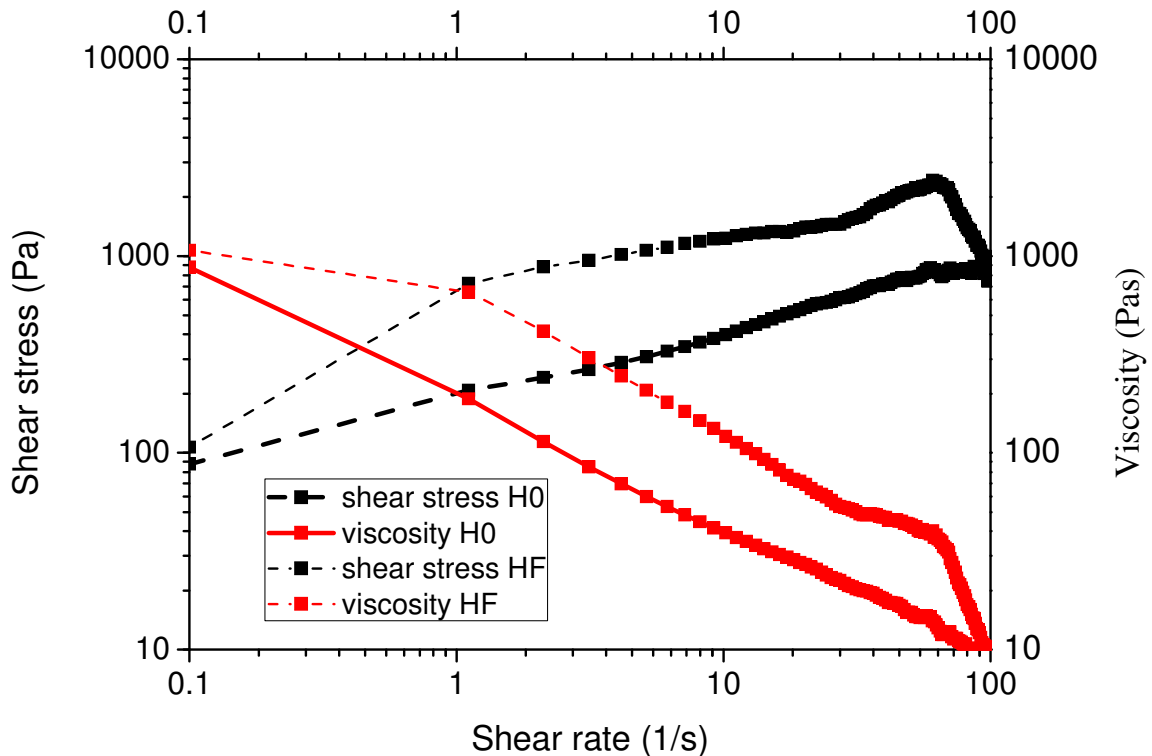


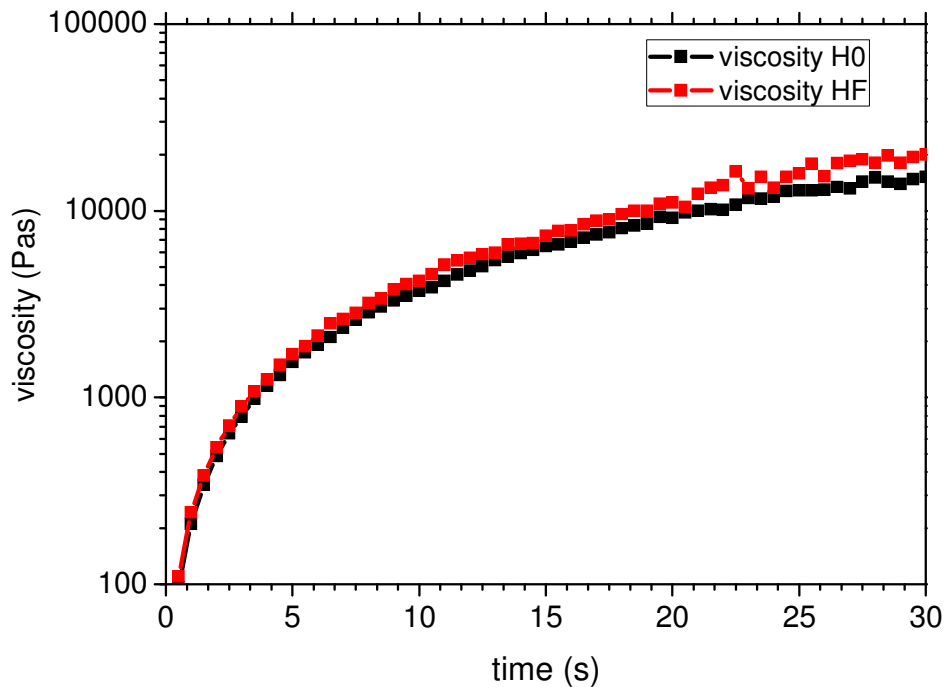
**Figure 5** Flow curve for inks H0 and HF, showing the shear stress and the corresponding calculated apparent viscosity in dependence of the shear rate.

### 3.2.1.3 Time dependent recovery

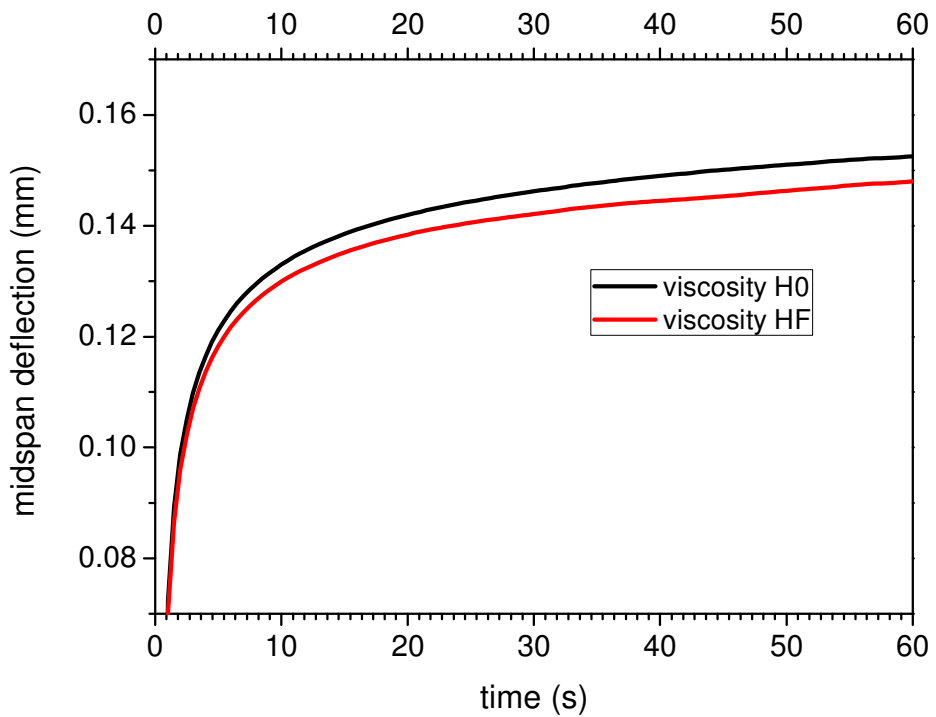
In this test, the material is sheared at a high shear rate in a first step and then sheared in a second step at low shear rate (corresponding to a shear stress  $< \tau_y$ ). In the second step, the increase of viscosity is recorded in dependence of time. The significance of this measurement can be interpreted as a destruction of the microscopic order of the material in the first step, followed by a recovery of the structure with time in the second step.

Figure 6 shows the variation in viscosity with time at a shear stress of 25 Pa, after a pre-shear of 30 s at  $50 \text{ s}^{-1}$ . The curves for H0 and HF are very similar: the viscosity is low at the beginning ( $< 100 \text{ Pas}$ ), but it increases by two orders of magnitude in the first  $\approx 20 \text{ s}$ , approaching a plateau value.





**Figure 6** Viscosity recovery test. The diagram shows a plot of the change in viscosity with time at a constant shear rate of  $0.1 \text{ s}^{-1}$ , after a pre-shear at  $25 \text{ s}^{-1}$ .



**Figure 7.** Plot of the midspan deflection in dependence of time calculated with Eq. 2 and data from Figure 6

By using the results of *Figure 6* in *Eq. 2* and *Eq. 3*, the deflection profile in the middle of the filament can be calculated, as in *Figure 7*. The shape of the curve resembles that of *Figure 6*. It can be interpreted that the filament deforms in the first seconds, but the viscosity quickly increases and the deformation also tends to reach a plateau value, because the viscosity becomes so high that further deformation is basically hindered. A similar result was also measured experimentally by (Lewis, 2006).

For a spanning distance of 1 mm and a filament diameter of 0.35 mm, the final calculated deflection was  $\approx 0.15$  mm.

This result confirms that the indicated geometry can be replicated, even though (Schlordtil and Greil, 2012) reported better results following this proposed model, with a deflection of  $\approx 0.04$  mm.

### 3.2.2 Production and characterization of porous scaffolds

Several porous lattices could be replicated by means of filament-based 3D-printing of the inks described in the previous paragraph.

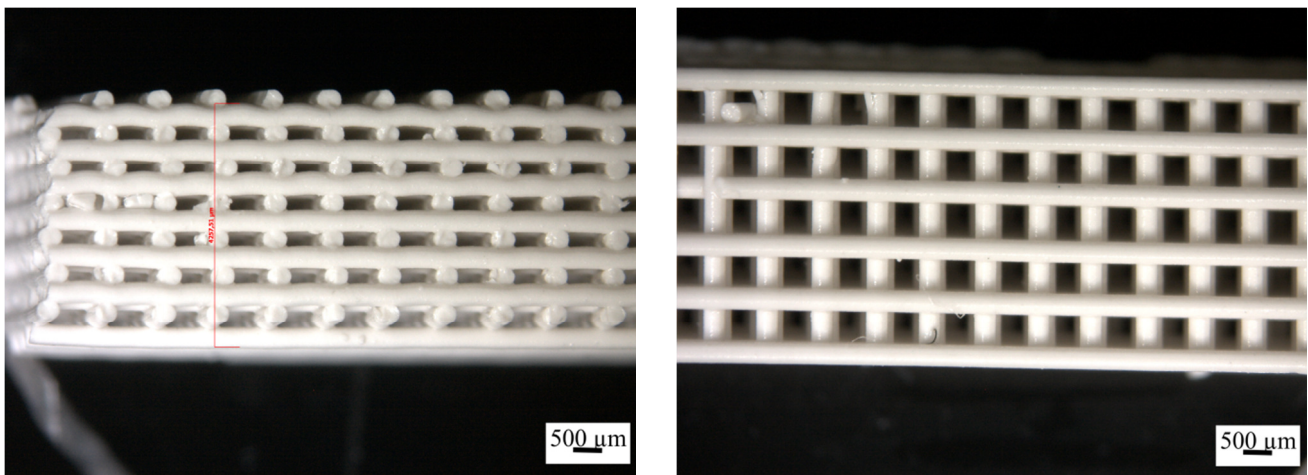


**Figure 8** Optical microscope images of a green scaffold produced with ink HF. Top view (left) and side view (right).

*Figure 8* shows an example of these 3D-printed structures in the green state. Top view (left) and side view (right).

The image is relative to ink HF, but scaffolds printed with H0 were similar in the green state. The filaments showed very limited sagging and deformation, which confirmed that the rheological properties of these inks were suitable for replicating this geometry.

The ceramization heat treatment however was problematic and often caused the appearance of large cracks in samples produced with H0, see *Figure 9*.

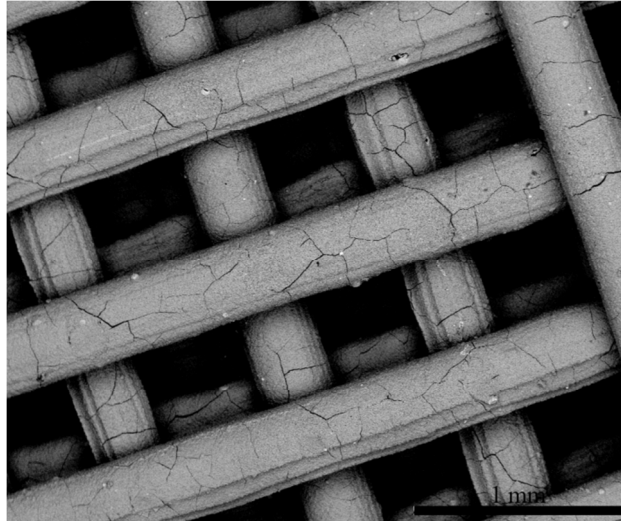


**Figure 9** Scanning electron microscope micrograph (backscattered electrons) of a scaffold produced with ink H0 and heat treated at 1200°C in air, showing several cracks in the filaments.

These cracks are likely formed due to the gas release and large shrinkage involved with the phase transformations which happen during the heat treatment. Gaseous species are released both during the polymer-to-ceramic transformation and by the decomposition of  $\text{CaCO}_3$  to  $\text{CaO}$  and  $\text{CO}_2$ . A hot-stage electron microscope analysis has been performed up to 1200°C in order to attempt understanding which was the most critical temperature range; unfortunately, no conclusive evidence could be collected due to the limited resolution of the instrument at high temperatures.

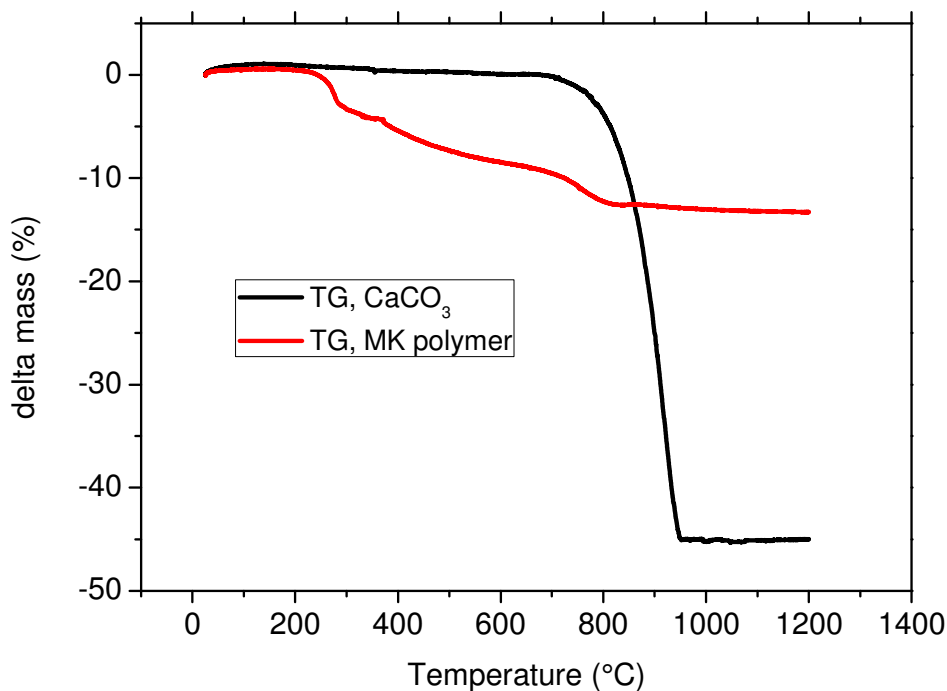


**Figure 10** Thermo-gravimetric curves of  $\text{CaCO}_3$  and MK polymer raw materials

Based on the thermo-gravimetric curves shown in *Figure 10*, the MK polymer had a mass loss starting from  $\approx 230^\circ\text{C}$  which is a result of the cross-linking reactions. At temperatures higher than  $\approx 350^\circ\text{C}$ , there is an almost continuous mass loss due to the ceramization decomposition reactions, which ends at  $\approx 830^\circ\text{C}$ . The  $\text{CaCO}_3$  powder, instead, started to decompose at  $\approx 700^\circ\text{C}$  forming  $\text{CaO}$  and  $\text{CO}_2$ , with most of the mass loss concentrated between  $800^\circ\text{C}$  and  $950^\circ\text{C}$ . Due to the fact that the  $\text{CaCO}_3$  total mass loss was very high ( $\approx 45\%$ ), it was hypothesized that its decomposition may have been the major cause of the severe cracking of the filaments. Unfortunately, an attempt to use a  $\text{CaO}$  filler instead of  $\text{CaCO}_3$  again led to defected samples, probably because of the difficult processing of  $\text{CaO}$  due to its high hygroscopicity, which makes its use impractical. It is possible that the use of other  $\text{CaO}$  precursors would lead to improved results.

A different approach was finally attempted, which consisted in the addition of a powder hardystonite filler to the ink, which acted as an inert filler as it does not participate in the ceramization reactions during the heat treatment, thus decreasing the total amount of gaseous species released. Accordingly, ink HF was formulated and tested, as described in *Table 1*.

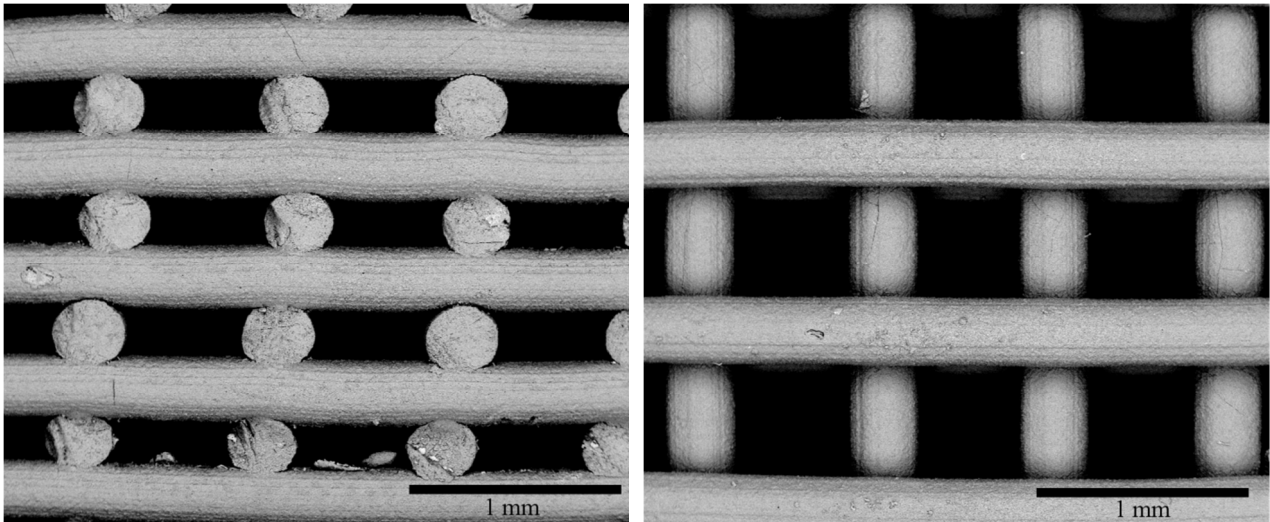


**Figure 11** Scanning electron microscope micrograph (backscattered electrons) of a scaffold produced with ink H0 and heat treated at 1200°C in air. Left: side view; right: top view.

As visible in *Figure 11*, the addition of the hardystonite inert filler greatly decreased the number of cracks in the filaments. The few cracks that are still visible may be related to the heat treatment, but may be also due to the preparation, i.e. cutting, of the samples for the analysis.

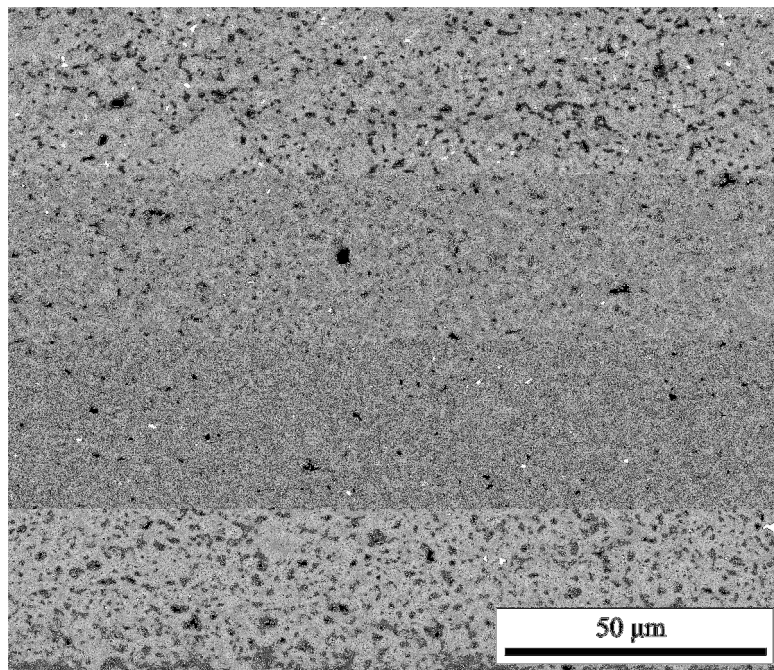


**Figure 12** Scanning electron microscope micrograph (backscattered electrons) of the surface of a scaffold produced with ink H0 and heat treated at 1200°C in air.

*Figure 10* shows an image of the surface of a filament, which reveals that the material was microporous. This porosity was most likely generated during CO<sub>2</sub> release from decomposition of CaCO<sub>3</sub>. It has been already noted in chapter 2 that porosity in the struts is detrimental for the mechanical properties, however it can be important for the biological properties of the scaffold, favoring cells attachment and proliferation. An amount of porosity in the strut of  $\approx 20\%$  was estimated by optical analysis.

The heat treatment of scaffolds HF was also investigated in nitrogen. The use of a non-oxidative atmosphere influences the decomposition of the preceramic polymer, which yields a SiOC residue upon ceramization (see chapter 1), instead of a SiO<sub>2</sub> residue which is obtained in air (see chapter 2).

It is clear from the SEM images in *Figure 13* that the scaffolds produced in nitrogen did not show any crack or defect created during the heat treatment.

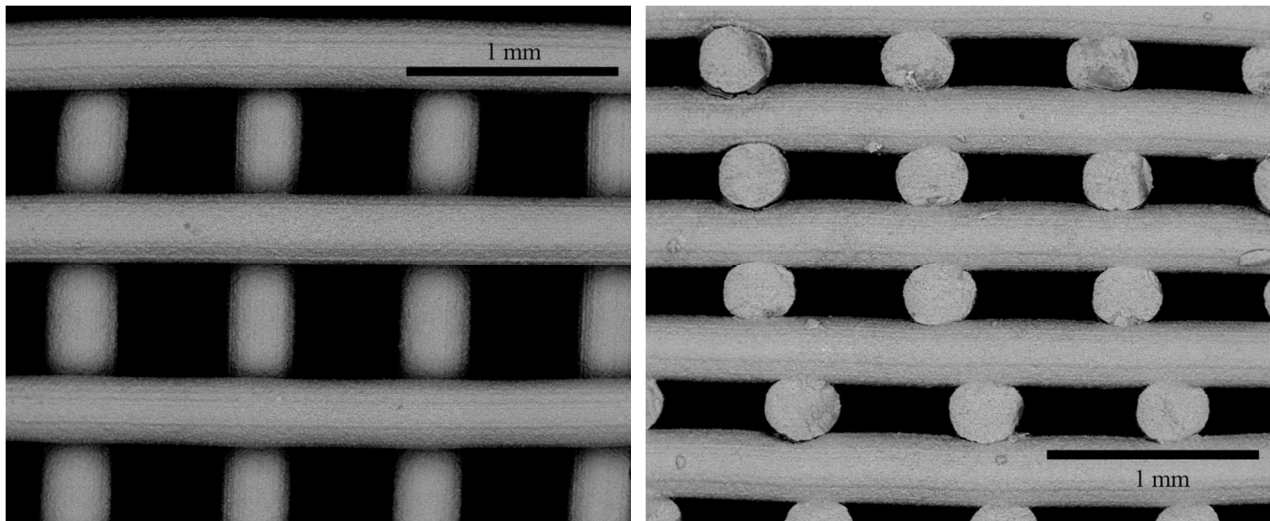


**Figure 13** Scanning electron microscope micrograph (backscattered electrons) of a scaffold produced with ink H0 and heat treated at 1200°C in air. Left: side view; right: top view.

As it will be described in paragraph 3.2.3, this formulation did not form hardystonite as main ceramic phase, nonetheless this result shows the potential of applying a heat treatment in inert atmosphere to other silicate ceramic systems.

As a final remark, it can be noted that other geometries can be replicated by this technology and material systems. *Figure 14* shows a ceramic 3D-printed vase of composition H0 and heat treated at 1000°C/ 1h. This part was produced to demonstrate that complex thin-walled structures with a high aspect ratio could be replicated. The nozzle used for this part had a diameter of 0.8 mm.



**Figure 14** Ceramic vase 3D-printed with composition H0 and heat treated at 1000°C for 1h.

### 3.2.3 Phase composition

The phase composition of scaffolds produced with ink HF has been investigated after heat treatment at 1200°C for 1 h in air or in nitrogen (*Figure 15 (a) and (b)*, respectively).

When heat treated in air, composition HF yielded almost pure hardystonite and secondary phases could not be detected. In particular, there were no traces of non-reacted ZnO or other raw materials.

As anticipated in the previous paragraph, HF treated in nitrogen did not form mainly hardystonite. The main phases found were two polymorphs of wollastonite ( $\text{CaSiO}_3$ ), parawollastonite and pseudowollastonite, along with only small traces of hardystonite. It is relevant that no other phases containing Zn atoms were present, which leads to the consideration that most part of the Zn was not present in the sample anymore after heat treatment.

A hypothesis could be that the ZnO underwent a carbothermal reaction with the carbonaceous residuals from the preceramic polymer (which are not decomposed in nitrogen as in air), being reduced to metallic Zn. The metallic Zn most probably evaporated at the higher treatment temperatures, which was confirmed by the finding of metallic Zn on the walls of the furnace. It seems reasonable that, being the composition deprived of Zn, wollastonite ( $\text{CaSiO}_3$ ) was formed instead of hardystonite ( $\text{Ca}_2\text{ZnSi}_2\text{O}_7$ ), because both phases have the same Ca:Si molar ratio.

The absence of zinc in the samples heat treated in nitrogen was also confirmed by XRF analysis, as reported in *Table 2*.

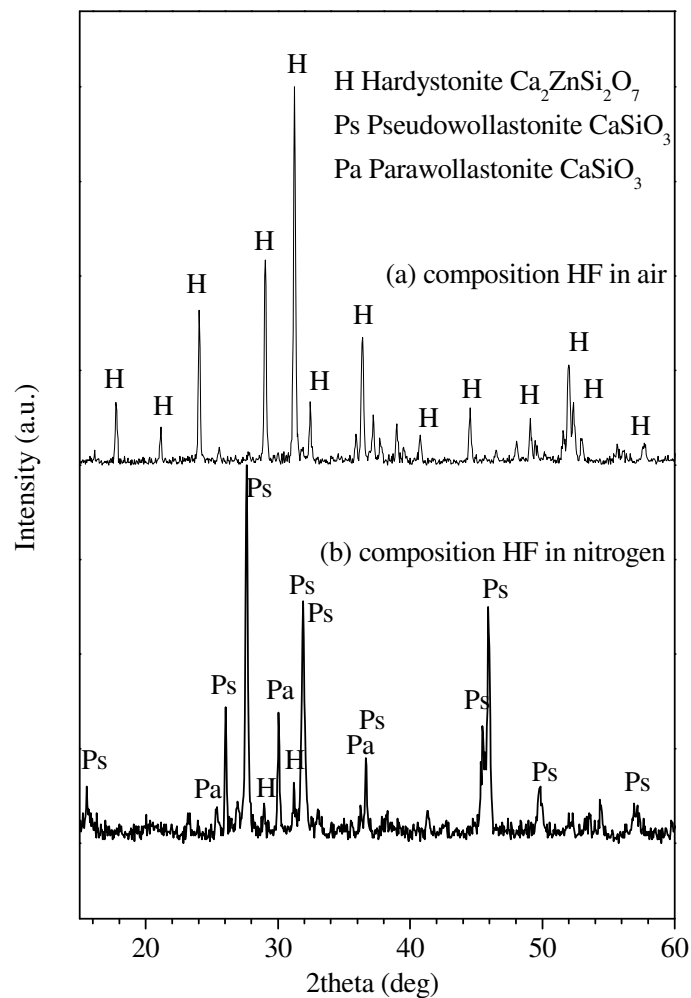


**Figure 15** Diffraction pattern of composition HF heat treated at 1200°C for 1 h: (a) in air (b) in nitrogen

Oxide / wt%	HF in air	HF in nitrogen
SiO <sub>2</sub>	39.1	55.8
CaO	34.6	42.0
ZnO	21.0	0.05
Al <sub>2</sub> O <sub>3</sub>	3.10	1.42
Na <sub>2</sub> O	1.77	
MgO	0.43	0.74
Fe <sub>2</sub> O <sub>3</sub>	0.05	0.04

**Table 2** Composition of samples HF heat treated in air and in nitrogen, measured by XRF



This result clearly indicates that after heat treatment in nitrogen there was an almost complete loss of Zn. The molar ratio  $\text{SiO}_2/\text{CaO}$ , which in the sample heat treated in air is very close to the unity (1.05) as in the hardystonite phase, also slightly increases, indicating an enrichment in  $\text{SiO}_2$  compared to CaO (ratio 1.24). A contamination of  $\text{Al}_2\text{O}_3$  probably derived from the ball milling process, while other impurities likely came from the raw materials.

### 3.2.4 Physical and mechanical properties of the scaffolds

Scaffolds produced with ink H0 and heat treated in air had a rather low compressive strength of  $0.6 \pm 0.2$  MPa at an average total porosity of  $77 \pm 2\%$ .

The properties of scaffolds produced with ink HF are collected in *Table 3* and show an almost three folds improvement in the compressive strength compared to H0 in the case of heat treatment in air and up to five folds in the case of heat treatment in nitrogen. This result is expected because of the almost complete elimination of cracks in HF samples compared to H0. Two batches with slightly different properties have been measured, therefore both are reported in the table.

	Shrinkage X (%)	Shrinkage Y (%)	Shrinkage Z (%)	Total porosity (%)	Compressive strength (MPa)
<b>HF in air 1200°C</b>					
Batch 1	$11.2 \pm 0.8$	$11.3 \pm 1.2$	$15.7 \pm 0.7$	$63 \pm 4$	$1.9 \pm 0.5$
Batch 2	$9.0 \pm 1.0$	$8.5 \pm 0.5$	$9.9 \pm 1.5$	$74 \pm 3$	$1.6 \pm 0.3$
<b>HF in nitrogen 1200°C</b>					
Batch 1	$9.3 \pm 1.6$	$10.1 \pm 1.4$	$7.5 \pm 1.3$	$72 \pm 1$	$3.2 \pm 0.8$
Batch 2	$8.1 \pm 0.5$	$9.1 \pm 1.0$	$10.0 \pm 1.0$	$80 \pm 3$	$2.5 \pm 0.6$

**Table 3** Shrinkage, total porosity and compressive strength of HF scaffolds heat treated in air and in nitrogen

### 3.3 Comparison of the mechanical properties of scaffolds produced by different technologies

Figure 16 compares the compressive strength in dependence of porosity for the scaffolds reported in Table 3 with several results of other scaffolds reported in literature, all produced by additive manufacturing technologies. The compressive strength of the cylindrical scaffolds produced by powder-based 3D-printing and presented in chapter 2 are also reported.

Plotting the y-axis with a logarithmic scale allows to observe that the strength data tend to follow a linear dependence with the porosity, corresponding to a well-known exponential law:  $\sigma(P) = \sigma_0 \exp(-bP)$ , where  $\sigma(P)$  is the compressive strength,  $\sigma_0$  a constant related to the strength of the zero-porosity material,  $b$  another constant and  $P$  the porosity. (Liu, 1997)

It is not easy to directly compare scaffolds with different geometries and made of different materials, but the examples reported in the plot include only biomaterials, in particular based mainly on calcium phosphates. Scaffolds produced by extrusion-based processes generally had a cubic geometry with orthogonal pores, while scaffolds produced by indirect AM techniques mostly had a cylindrical geometry with orthogonal or radial pores resembling the structure of bone implants. Both geometries are possible to be replicated by direct and indirect AM, but a cubic geometry is used in the case of extrusion-based printing because it simplifies the deposition path, while indirect technologies are almost geometry independent.

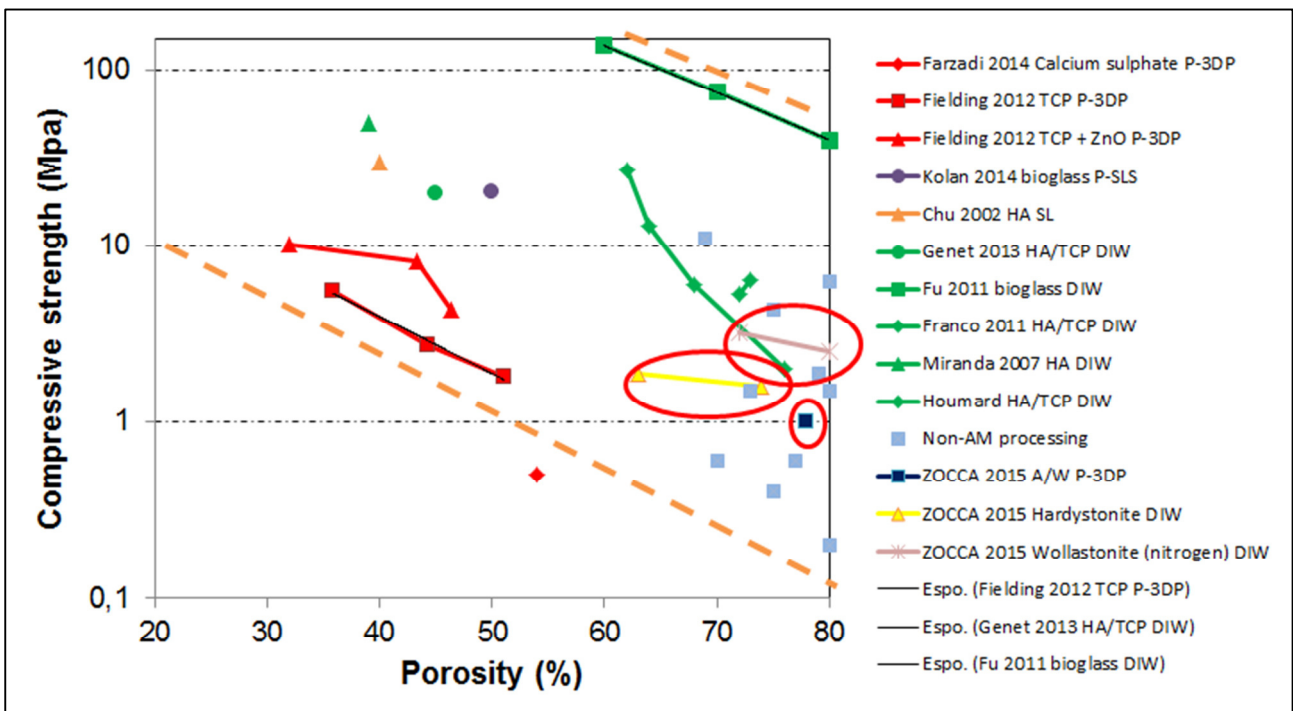


Figure 16 Plot of the compressive strength in dependence of porosity for porous scaffolds

It can be noticed that the scaffolds produced in this work compare rather favorably (given a same level of porosity) with scaffolds produced by other AM techniques and by traditional (non-AM) processes.

A more general observation is that scaffolds produced by DIW in most cases possess better mechanical properties compared to scaffolds produced by powder-based technologies. As pointed out in the introduction, DIW is able to generate denser, and thus stronger, struts compared to powder-based technologies.

The absolute values of compressive strength are distributed in a wide range of values, from 0.5 to over 100 MPa; however, there is a clear trend. Scaffolds produced by P-3DP have, in particular, a strength which is up to one order of magnitude lower than the strength of scaffolds made by DIW. It seems reasonable to correlate this observation with the micro-porosity in the scaffold struts: even though this value depends also on the specific material system used, there is a clear influence of the process, which can be found when examining the properties of parts shaped without designed porosity. Parts produced by P-3DP generally have a high level of residual micro-porosity, while parts produced by liquid-based processes (such as DIW and SL) can be almost dense after sintering.

### **3.4 Conclusions**

The extrusion-based 3D-printing of a preceramic ink was demonstrated, replicating complex hardystonite scaffolds comprising a designed ordered porosity. The rheological characterization showed that the ink used was suitable for the generation of spanning features up to 1 mm long without excessive sagging, when immersed in oil.

Scaffolds heat treated in nitrogen showed a higher mechanical strength compared to those heat treated in air. Even though this composition did not form the expected phases (hardystonite) in nitrogen, it might be applicable to different ceramic phases that will be investigated in the future, and which are potentially not affected by the problem of Zn evaporation.

## References

- Herschel, W.H., Bulkley, R., 1926. Measurement of consistency as applied to rubber-benzene solutions, in: *Am. Soc. Test Proc.* pp. 621–633.
- Lewis, J.A., 2006. Direct ink writing of 3D functional materials. *Adv. Funct. Mater.* 16, 2193–2204.
- Liu, D.-M., 1997. Influence of porosity and pore size on the compressive strength of porous hydroxyapatite ceramic. *Ceram. Int.* 23, 135–139. doi:10.1016/S0272-8842(96)00009-0
- Paquien, J.-N., Galy, J., Gérard, J.-F., Pouchelon, A., 2005. Rheological studies of fumed silica–polydimethylsiloxane suspensions. *Colloids Surf. Physicochem. Eng. Asp.* 260, 165–172. doi:10.1016/j.colsurfa.2005.03.003
- Raghavan, S.R., Khan, S.A., 1995. Shear-induced microstructural changes in flocculated suspensions of fumed silica. *J. Rheol.* 1978-Present 39, 1311–1325. doi:10.1122/1.550638
- Schlörtdil, T., Greil, P., 2012. Robocasting of Alumina Lattice Truss Structures. *J. Ceram. Sci. Technol.*
- Smay, J.E., Cesarano, J., Lewis, J.A., 2002. Colloidal inks for directed assembly of 3-D periodic structures. *Langmuir* 18, 5429–5437.
- Zhang, M., Lin, K., Chang, J., 2012. Preparation and characterization of Sr–hardystonite (Sr<sub>2</sub>ZnSi<sub>2</sub>O<sub>7</sub>) for bone repair applications. *Mater. Sci. Eng. C* 32, 184–188. doi:10.1016/j.msec.2011.10.017

## CURRICULUM VITAE

### **Personal data**

Name: Andrea Zocca

Date of birth: 25 March 1987

Place of birth: Mirano (VE), Italy

Gender: male

Nationality: Italian

### **Education**

- 09/2006 → 06/2009 Bachelor degree in materials engineering. University of Padova, Italy
- 09/2009 → 12/2011 Master's degree in materials engineering. University of Padova, Italy
- since 03/2012 PhD student, Clausthal university of technology (Germany) and University of Padova (Italy), in the frame of a joint doctorate.

### **Employment**

- 03/2009 → 07/2009 Internship. University of Padova, department of chemical processes of engineering.
- 04/2011 → 06/2011 Internship. University of Padova, department of mechanical engineering
- 07/2011 → 10/2011 Internship. Clausthal University of technology, Institut for non-metallic materials
- 03/2012 → 02/2014 Researcher at BAM (Federal Institute for Materials Research and Testing), Division of Ceramic Processing and Biomaterials. Berlin, Germany.
- 03/2014 → 03/2015 Researcher at the University of Padova, department of industrial engineering

Berlin, 14/04/2015

signature